

Granular material flow into cable shovel dippers

by

Raheleh Rasimarzabadi

A thesis submitted in partial fulfillment of the requirements for the degree of

Doctoral of philosophy
In
Mining Engineering

Department of Civil and Environmental Engineering
University of Alberta

© Raheleh Rasimarzabadi, 2016

Abstract

Electric cable (or rope) shovels are critical equipment in the surface mining industry. An improved understanding of the factors that affect the flow of broken material into the dipper during loading can help to evaluate the performance of the excavator, define the criteria for equipment selection, and develop ways to mitigate equipment damage caused by broken particles.

In this thesis, the flow pattern of angular cohesion-less granules loading into a cable shovel dipper was investigated both experimentally and numerically. The experimental study was performed through a series of laboratory tests by moving 1:32 and 1:20 (cube root scale) models of a 44m³ dipper through a test bin filled with angular crushed limestone. The influence of several parameters, including hoist speed, dipper pitch angle, and dipper size on the flow pattern, was investigated qualitatively and quantitatively.

In the numerical study, a 2D model was generated to simulate the filling of a cable shovel dipper, using PFC version 5.0 developed by Itasca. To verify the accuracy of the model, the results were compared to the experimentally measured results. Afterwards, a series of the model was developed to investigate the influence of particle shapes, particle sizes, and the role of the dipper tooth on the material behaviour.

Compared to experimental measurements, there was a good agreement between DEM (Discrete Element Modeling) and the lab experiments in identifying the filling procedure. The numerical model predicted all stages of filling, and the flowing layers of the particles. Due to the shortcomings and limitations, DEM was inaccurate in modeling the material properties, resulting in a lower resistance against digging via the dipper.

Based on the performed experimental and numerical investigations, angular cohesion-less material follows a specific flow pattern loading into a cable shovel dipper. This flow pattern is independent on the examined dig conditions and material properties, however, such parameters may influence the filling procedure, and therefore the productivity of the machine. For instance, in a specific period of time, employing a lower dipper angle and a faster dig time results in a higher number of completed dig cycles due to shorter dig times, and a higher amount of payload at each dig cycle due to a lower dipper angle, and both contribute an improved machine productivity. Employing a bigger size dipper although increase the amount of payload due to a wider lip length, it does not necessarily result in a high fill factor. Applying an appropriate depth of penetration according to the dipper size is one of the considerable factors. Dipper tooth is another parameter that results in a higher amount of payload due to a deeper penetration into the rock-pile. Regarding to material properties, increasing particle size and angularity has inverse effect on the machine productivity and reduces the dipper fill factor. One of the interesting findings of this study was identifying the procedure of creating the empty space in side the dipper during a dig cycle. Creating such a void space is a function of material properties, especially material internal friction coefficient, that results in a reduced fill factor and even over estimation of the payload.

Dedications

To my husband, Ehssan, who has been a constant source of support and encouragement during the challenges of graduate school and life. I am truly thankful for having you in my life. And, to my parents, who have always loved me unconditionally. Without you I never would have been able to achieve my goals.

Acknowledgment

I would like to express my sincere gratitude to my thesis advisor Dr. Tim Joseph for his invaluable advices and kind supports during the course of this study. I owe great respect to him for the opportunity he granted me to do research work under his tutorship. I would also like to thank Hammer-stone Company for providing the material required for this research, and Lucas Duerksen for designs and setting up the experimental model.

Last but not the least, I would like to express my heartfelt gratitude to all those who are directly or indirectly involved in the completion of this research work.

Table of content

Chapter 1	1
Introduction.....	1
1-1- Statement of the problem	1
1-2- Objectives of the study	2
1-3- Hypotheses of the study	2
1-4- Thesis outline	2
Chapter 2.....	4
Literature review	4
2-1- Particle shape definition.....	4
2-1-1- Description of shape.....	4
2-1-2- Description of roundness	5
2-1-3- Description of surface texture	9
2-2- Inter particle interactions	10
2-3- General modes of rock mass motions in rock slopes	18
2-3-1- Free fall	18
2-3-2- Bouncing	19
2-3-3- Rolling.....	20
2-3-4- Sliding.....	21
2-4- Dipper-ground interactions	21
2-4-1- Factors influence resistive force.....	22
2-4-2- Common hypothesis of material properties	24
2-4-3- Dipper-ground interaction models	24
2-5- Research on movement of granular particles into a ground engaging vessel	31
2-5-1- Analytical and experimental studies	31
2-5-2- Discrete element methods (DEM) studies.....	34
2-6- Influence of fragment properties on electric cable shovel performance	35
2-7- Key performance indicators for cable shovels	38
2-8- Size distribution assessment techniques.....	39

2-8-1- WipFrag Software	40
Chapter 3	42
Test preparation	42
3-1- Cable shovel operation.....	42
3-2- Experimental setup.....	44
3-3- Material properties and scaling the dipper profile	46
3-3-1- Determining the size distribution of material.....	47
3-3-2- Determining material internal friction angle and cohesion.....	49
3-3-3- Determining particle loose density.....	50
3-4- Conclusion	51
Chapter 4.....	52
Broken particle flow mechanism into a cable shovel dipper	52
4-1- Test procedure.....	52
4-2- Particle flow observations.....	54
4-3- Influence of pitch angle on the particle flow mechanism	58
4-4- Influence of hoist speed on the particle flow mechanism.....	59
4-5- Influence of dipper size on the particle flow mechanism	63
4-6- Influence of dig speed and pitch angle on performance of modeled cable shovel dipper	64
4-7- Particle flow mechanism.....	69
4-8- Conclusion	72
Chapter 5.....	73
Failure curvatures developed by digging.....	73
5-1- Test procedure.....	75
5-2- Results and discussion	76
5-3- Conclusion	80
Chapter 6.....	81
Scaling to full size dipper	81
6-1- Physical models	81
6-2- Dipper analogy.....	82
6-2-1- Geometry analogy of the dipper.....	82
6-2-2- Crowd analogy	83

6-2-3-	Performance analogy of the dipper	85
6-3-	Material analogy	87
6-3-1-	Size distribution analogy.....	87
6-3-2-	Particle size analogy.....	90
6-4-	Conclusion	90
Chapter 7.....		92
Discrete element method.....		92
7-1-	Limit equilibrium analysis	92
7-1-1-	Limitation of common limit equilibrium method	93
7-2-	Numerical modelling.....	95
7-3-	Discrete element method.....	95
7-3-1-	A brief description of PFC	96
7-3-2-	Force displacement law	96
7-3-3-	Law of motion.....	98
7-3-4-	Contact models.....	99
7-3-5-	Damping models	103
7-3-6-	Balls and Clumps	104
7-3-7-	Boundary Conditions	104
Chapter 8.....		105
Numerical simulation of filling a cable shovel dipper		105
8-1-	Determination of material properties	105
8-1-1-	Particle shape	106
8-1-2-	Particle size and size distribution.....	106
8-1-3-	Stiffness.....	109
8-1-4-	Friction coefficient.....	110
8-1-5-	Damping.....	111
8-2-	Reducing the processing time	112
8-2-1-	Decreasing cycle time	112
8-2-2-	Increasing time step	114
8-3-	DEM simulation of cable shovel dipper filling.....	114
8-3-1-	Investigating the generation of the void space inside the dipper	117

8-4-	Investigating the influence of material properties and dipper tooth on cable shovel dipper filling via DEM modeling.....	121
8-4-1-	Influence of particle size on flow mechanism.....	122
8-4-2-	Influence of particle shape on flow mechanism.....	126
8-4-3-	Influence of dipper teeth on flow mechanism.....	131
8-4-4-	Numerical modeling results	135
8-6-	Conclusion	136
	Chapter 9.....	138
	Conclusion	138
9-1 -	Main conclusions	138
9-1-1-	modeling cable shovel filling.....	138
9-1-2-	Influence of dig conditions on particle flow behaviour	141
9-1-3-	Influence of material properties on particle flow behaviour	142
9-1-4-	Influence of material properties on creating the void space inside the dipper	142
9-1-5-	Limitations	143
9-2 -	Research contributions.....	143
9-3 -	Suggestions for Future Works.....	146
	References.....	149
	Appendix A.....	161
	Appendix B.....	162

List of figures

Figure 2-1 A simplified representation of form, roundness and surface texture (adapted after Barrett, 1980)	4
Figure 2-2 Wadell's procedure for evaluating particle (adapted after Sukumaran et al., 2001)	6
Figure 2-3 Particle shape determination—sphericity and roundness chart. particle regularity $\rho=(\text{roundness} + \text{sphericity})/2$ is constant along the dotted lines (adapted after Krumbein and Sloss 1963)	7
Figure 2-4 Parameters for determining the degree of angularity (After Lees 1964)	8
Figure 2-5 Angularity estimation chart (adapted after Lees 1964)	8
Figure 2-6 Measurement method for characterizing a particle surface texture (adapted after Wright 1955)	9
Figure 2-7 Rotational characteristics in loose and dense packing (adapted after Santamarina and Cho, 2004)	12
Figure 2-8 Inter-particle rolling model (a) Low range assemblages; (b) wide range assemblages (adapted after Morgan, 2000)	13
Figure 2-9 Force chains generated in the particles sliding between two layers, critical angle in angular particles (b), narrow particle size distribution rounded particles (c), and wide particle size distribution rounded particles (d) (adapted after Mair et al., 2002)	14
Figure 2-10 Friction as a function of shear displacement for angular and spherical grains at $\sigma_n = 5$ MPa (adapted after Mair et al., 2002)	15
Figure 2-11 Schematic diagrams of spherical glass beads deforming as they are sheared between rough boundaries (adapted after Anthony and Marone, 2005)	15
Figure 2-12 Schematic diagrams of spherical and angular grains sheared between smooth and rough boundaries (adapted after Anthony and Marone, 2005)	17
Figure 2-13 Tilt tests with multiple blocks indicate higher strength than with large single blocks (adapted after Bandis et al. 1981&1982)	18
Figure 2-14 Rock block before and after the impact (adapted after Petje et al., 2006)	19
Figure 2-15 Sequences of rock positions (adapted after Bozzolo et al., 1986)	20
Figure 2-16 Two-Dimensional View of Excavation (adapted after Blouin et al., 2001)	21
Figure 2-17 Fundamental earth moving actions (adapted after Blouin et al., 2001)	22
Figure 2-18 Definition of cutting angle (adapted after Hemami et al., 1994)	23
Figure 2-19 Definition of depth of cutting, a) constant (bulldozer) b) variable (back-hoe) (adapted after Hemami et al., 1994)	24

Figure 2-20 2D Logarithmic spiral rupture approach for cutting soft ground (adapted after Osman, 1964)	25
Figure 2-21 Static equilibrium approximation of a failure surface (adapted after Blouin et al., 2001)	25
Figure 2-22 Loading Force Components during Digging Task (adapted after Blouin et al., 2001)	30
Figure 2-23 Unblasted soft material face (adapted after Joseph and Shi, 2012)	31
Figure 2-24 Blasted rock face (adapted after Joseph and Shi, 2012)	32
Figure 2-25 The Shear Zone Theory (adapted after Rowlands, 1991)	33
Figure 2-26 Top view of dumps for different widths (a)-(d) of a centrally situated tool (adapted after Maciejewski et al., 2004)	34
Figure 2-27 Dragline bucket filling results with rig angle=0 (adapted after Coetzee et al, 2009-A)	36
Figure 3-1 Cable shovel nomenclature (adapted after Stavropoulou et al., 2013)	43
Figure 3-2 2D Illustration of typical cable shovel dipper (adapted after Shi, 2007)	44
Figure 3-3 Schematic definition of rake angle, tooth angle and pitch angle (adapted after P& H, 2001)	44
Figure 3-4 Three-dimensional test rig	45
Figure 3-5 Experimental setup showing the position of the load cell	46
Figure 3-6 Data acquisition system	46
Figure 3-7 Size distribution of crushed limestone	48
Figure 3-8 Scale dipper	48
Figure 3-9 Direct shear test machine	49
Figure 3-10 Plot of shear stress versus horizontal displacement for $\sigma_n = 630.89$ KPa	50
Figure 3-11 Plot of maximum shear stress versus the vertical confining stress	51
Figure 4-1 Pitch angle definition	53
Figure 4-2) Snapshots of different steps of the particle flow into the dipper of scaled model	55
Figure 4-3 Creating and bulldozing material in front of the dipper	56
Figure 4-4 Traditional design of shovel dipper with void space at top area of the back wall (adapted after Shi, 2007)	57
Figure 4-5 Moving the location of the void space from the bottom side (a) to the top side (b) of the back wall by changing the orientation of the dipper	58
Figure 4-6 Angle between the dipper and rockpile with slope angle of 37° at the time of engaging at examined pitch angle	59

Figure 4-7 Low hoist speed, a) pitch angle 30°, b) pitch angle 20° and c) pitch angle 10° -the moment material reaches to the rear of the dipper	60
Figure 4-8 Moderate hoist speed, a) pitch angle 30°, b) pitch angle 20° and c) pitch angle 10° - the moment material reaches to the rear of the dipper	61
Figure 4-9 High hoist speed, a) pitch angle 30°, b) pitch angle 20° and c) pitch angle 10° -the moment material reaches to the rear of the dipper	62
Figure 4-10 An example plot of hoist force vs time resulted from the data acquisition system	65
Figure 4-11 Hoist force values with different hoist speeds at pitch angle of 30°	65
Figure 4-12 Cycle time range	66
Figure 4-13 Payload range for different conditions	66
Figure 4-14 Dig energy	67
Figure 4-15 Average rate of consuming energy	68
Figure 4-16 Specific dig energy	68
Figure 4-17 Diagram of different steps of the particle flow into the dipper of a cable shovel	70
Figure 5-1 The three distinct digging phases performed by a cable shovel (adapted after Stavropoulou et al., 2013)	74
Figure 5-2 Crack trajectory (dotted line) resembling a normal fault (adapted after Stavropoulou et al., 2013)	75
Figure 5-3 Soil cutting mechanism (adapted after Stavropoulou et al., 2013)	75
Figure 5-4 Different flow of material at the rockpile	77
Figure 5-5 Failure envelope inside the rockpile	79
Figure 5-6 Optimum dipper trajectory	80
Figure 6-1 Geometry of P&H 4100 dipper (Joy Global, 2012) vs. examined scaled model	83
Figure 6-2 Spiro shape trajectory versus circular shape trajectory	85
Figure 6-3 Dipper capacity versus suspended load and peak hoist force	86
Figure 6-4 Dipper capacity versus suspended load and peak hoist force of scaled dippers	87
Figure 6-5 Size distribution of crushed limestone	89
Figure 6-6 Fit to the RR model	90
Figure 7-1 slices and forces in a sliding mass (adapted after Krahn, 2003)	93
Figure 7-2 Typical DEM particle contact model (adapted after Coetzee et al., 2010)	98
Figure 7-3) Two particles in contact (adapted after Tiphavonnukul, 2002-A)	100
Figure 7-4) Sign convention for F_n and F_s (adapted after Tiphavonnukul, 2002-A)	102
Figure 8-1 Simplified particle shapes used in PFC modeling	107

Figure 8-2 Created angular particles used in PFC modeling	107
Figure 8-3 Size distribution of examined material vs size distribution of simulated material in PFC	108
Figure 8-4 Particle packing with different stiffness	109
Figure 8-5 Pile of limestone particles in angle of repose test	111
Figure 8-6 Pile of particles in simulated angle of repose test	111
Figure 8-7 Designed dippers for PFC modeling	113
Figure 8-8 Limiting the clumps to be created in a layer at the surface of the rockpile	113
Figure 8-9 Dipper filling procedure, DEM vs experimental set up	116
Figure 8-10 Simulated dig cycle with small size particles and uniform size distribution	118
Figure 8-11 Simulated dig cycle with medium size particles and uniform size distribution	119
Figure 8-12 Simulated dig cycle with large size particles and uniform size distribution	120
Figure 8-13 Created walls at PFC	122
Figure 8-14 Snapshots of a dig cycle with large particle sizes	123
Figure 8-15 Snapshots of a dig cycle with medium particle sizes	124
Figure 8-16 Snapshots of a dig cycle with small particle sizes	125
Figure 8-17 Snapshots of dig cycle with large particle sizes with more angular particles	128
Figure 8-18 Snapshots of dig cycle with medium particle sizes with more angular particles	129
Figure 8-19 Snapshots of dig cycle with small particle sizes with more angular particles	130
Figure 8-20 Snapshots of a dig cycle of low angular particles with a dipper with tooth	132
Figure 8-21 Snapshots of a dig cycle of high angular particles with a dipper with tooth	133
Figure 8-22 Snapshots of a dig cycle; a dipper with tooth vs without tooth	134
Figure 9-1 Diagram of the used approach in the research	139
Figure 9-2 Sample of designed particles in Rhino software, imported to PFC3D	147
Figure 9-3 Schematic 3D mode designed in Rhino, imported to PFC	147

List of tables

Table 2-1 Roundness Categories Roundness Categories based on Krumbein's work (adapted from Krumbein, 1941)	7
Table 3-1 Examined normal stresses and obtained shear strengths	50
Table 5-1 Length of failures ahead of the dipper based on the number of dipper length at 9 different dig conditions	78
Table 6-1 Shovel specifications and performance	86
Table 6-2 Predicted key performance for full scale dippers	87
Table 6-3 Required parameters to fit to RR	89
Table 7-1 different method of stability analysis indicating equilibrium conditions, forces and factor of safety considered (adapted after Sinha, 2008)	94
Table 8-1 Different particle sizes used in PFC simulation	10 8

List of symbols

2D	Two-dimensional
A	Total degree of angularity
a	Magnitude of measured angle
A_i	Degree of angularity
B	Width of foundation
C	Cohesion
C_0	Compactness and Cutting resistance index
C_a	Adhesion
D	distance between 2 particles
d	particle size
d	Depth of operation
DEM	Discrete element method
d_m	mean particle size
E	Void ratio
E	elasticity
e_{max}	Maximum void ratio
e_{min}	Minimum void ratio
e_z	Tool plate thickness
F	Shape factor
F(d)	distribution function
F1	Force required to overcome the weight of the loaded material in and above
F2	Resultant of forces of resistance for material moving towards the bucket
F3	Force due to the friction between the bucket walls and the soil material
F4	Resistance to cutting and/or penetration acting at the tip of the bucket and
F5	Inertia force of the material inside and above the bucket
F6	Force required to move the empty bucket
F^d	viscous component in hysteretic model
F^h	non-linear elastic component hysteretic model
F_n and F_t	summation of all forces in normal and tangential directions
g_c	contact activity index in Hertz model
k_l	Specific digging resistance
K_n and K_t	Stiffness in normal and tangential directions
Kz	Index for the type of cutting
l	Submerged length of the blade
M	mass of a particle
M	Resultant moment
m_x	mass of inertia of particle x
N	Number of corners of a particle
N	a measure of the spread of particle sizes
\dot{n}	Normal component of the relative velocity
N_γ, N_c, N_{ca} ,	Dimensionless Reece factors
N_γ', N_c', N_q'	N-coefficients for Terzaghi's model
P	Flatness ratio

P1	Cutting resistance of the flat trenching blade with a sharp edge
P2	Additional resistance due to the wear of the edge
P3	Resistance offered by the two sides of bucket
P4	Resistance due to friction of the sides
Q	Surcharge pressure acting vertically on soil surface - Elongation ratio
R	Radius of curvature of a corner
R	radius of a partice
$r_{\max\text{-in}}$ or R	Radius of the maximum inscribed circle
$r_{\min\text{-cir}}$	Radius of the smallest circumscribed sphere
S	Surface area of a sphere of the same volume as the particle - Cutting edge
S	Actual surface area of the particle
\dot{s}	tangential component of the relative velocity
U_n	Overlap in the contact normal direction
V	Speed
W	Blade width
X	Distance to the tip of the corner from the center of the maximum inscribed
\dot{x}	velocity vectors of a particle
Z	Number of other grains contacting each particle
Z	Coefficient for teeth configuration in the Zelenin model
A_c	Cutting angle
B	Rake or cutting angle
β_c	Tip angle
Γ	Soil bulk density
Δ	External friction angle
H	Failure envelope line
M	Friction coefficient
P	Shear plane angle
σ_n	Normal pressure acting perpendicularly on the shearing surface
T	Shear stress
τ_{mm} and τ_{mt}	Shear strengths in terms of the internal medium failure and the medium-tool
Φ	Internal friction angle
φ_c	Critical angle
Θ	angular velocity vectors of a particle
\bar{e}	unit vector from the center of one particle to the center of another particle
I_x	moment of inertia of particle x
\bar{t}	unit vector obtained by a clockwise rotation of \bar{e} through 90°
ΔF_n and ΔF_t	Incremental force in normal and tangential directions
Δ_n and Δ_t	Magnitudes of particle overlap in normal and tangential directions
ΔU_s	Displacement increment in the contact tangential direction
$\sum F_{xi}$	summation of all forces acting on the particle x

Chapter 1

Introduction

1-1- Statement of the problem

Ground-engaging tools have a significant influence in mining industry. The role and structure of such machines vary from one to another. The main groups of these machines are as follows (Coetzee, 2004): Blades penetrate into materials with a depth of cut not greater than their width, and move the material forward. “Bulldozer front blades”, “road graders”, “hauling scrapers”, and “snowplows” are some examples of machines armed with blades (Coetzee, 2004). Rippers are used to remove harder material with a width shorter than the applied depth of penetration. Bulldozers and graders are machines usually equipped with rippers (Coetzee, 2004). Buckets are made of blades and side walls to remove and load materials. Nowadays, ground-engaging tools are made of new metallurgical material and work with advanced energy supplies, but over the last 100 years, their overall structures have not been varied a lot (Coetzee, 2004).

Regarding to the loading blasted hard rock, the material shows flowing into a dipper instead of real cutting action (Joseph and Shi, 2012). In this case, excavating depends on material properties such as particle size, shape, and size distribution, and the dipper rake angle that encourages the material into the dipper (Joseph and Shi, 2012).

Based on previous works, the interrelation of the granular composition of blasted rock and shovel productivity has been studied incompletely. However, most studies did investigate the influence of particle size and size distribution of blasted material, while just a few looked at the effect of the shape of fragments. Particle flow, which occurs extensively in mining approaches, has received the least attention by previous researchers. For instance, little literature has been reported that relates directly to flow mechanisms of granular material into an excavator bucket. Although the filling behaviour of a dragline bucket has been studied experimentally or through discrete element modeling simulations, no cable shovel bucket filling investigation was identified in the literature.

This study is motivated by a desire to understand the cable shovel loading procedure better, leading to improved efficiency and productivity of this huge mining equipment.

1-2- Objectives of the study

The primary objective of this thesis was to investigate the flow mechanism of cohesion-less granular material entering the dipper of a cable shovel. This research aim was broken down into whether a flow pattern can be identified during a loading action, and if so, how various dig conditions and material properties may influence it. To reach this goal, two approaches were employed: scaled experimental laboratory tests and numerical modeling.

A set of experimental tests were performed to identify a general flow pattern and to investigate the influence of dig conditions by varying the dipper size, dipper pitch angle, and hoist speed. Also, generating failure envelopes in the rockpile during the dig cycle was studied experimentally. In numerical studies, a PFC code was developed to determine whether the modern DEM code can be used to accurately model the flow of granular material into a cable shovel dipper. To verify the numerical model, the experimental test results were used. Afterward, by modifying the designed PFC model, the influence of particle shape and size, and also the dipper's tooth were analysed.

1-3- Hypotheses of the study

- Granular cohesion-less materials follow a pattern, loading into a cable shovel dipper that is partially dependent on the material properties and dig conditions. A scaled physical model performs in a similar way to actual sized equipment, permitting findings to be extrapolated to a full size machine.
- DEM as a modeling tool is capable of simulating the granular material flow into a cable shovel dipper.

1-4- Thesis outline

Chapter 2 presents some background of the relevant topics involved in the present study. First, the definition and the modes of motion of particles are described. Secondly, dipper-ground interaction models and the relevant works are presented. This discussion is then followed by a brief background of the interrelation of granular blasted rock and shovel productivity along with the main key performance indicators for cable shovels. At the end, a brief overlook analyses the different size distribution assessment methods and the particular one used in the current study.

Chapter 3 introduces the design and set up of the scaled model for experimental analysis and describes the several preliminary tests required before performing the experiment.

Chapter 4 presents the mechanism of granular material flow investigations through a series of laboratory tests based on the designed scaled model explained in Chapter 3. Chapter 4 describes experimental observations along with qualitative and quantitative analysis of the influence of several parameters, including hoist speed, dipper pitch angle, and dipper size on the flow pattern. At the end, a general flow mechanism relevant to the cable shovel dipper filling is presented.

Chapter 5 focuses on the planar failures in a rockpile generated during a dig cycle of a cable shovel dipper, as a part of the experimental scaled tests.

Chapter 6 presents different approaches used to validate the proposal that the scaled experimental laboratory test results can be extrapolated to the full sized scale. The experimental results are compared to the available field and lab data. The geometry of the dipper profile, the relation between dipper and particle size, as well as the size distribution of particles are verified to be comparable to the full size scale.

Chapter 7 presents a brief overview of common limit equilibrium analysis methods used for slope stability analysis and describes why these methods are not suitable for the current study. In this discussion, the history and fundamentals of the numerical modeling technique used in this study is introduced. This technique consists of the theoretical framework of the particle flow code PFC along with a brief description of contact models, damping models, basic elements, and boundary conditions.

Chapter 8 describes the designed numerical models using PFC and presents the results and discussions of the numerical simulations. The experimental results are used to evaluate and validate the code. Furthermore, the numerical analysis of the influence of material properties and the dipper tooth on the particles' behaviour during loading cycle is presented.

Chapter 9 summarizes the experiment, methodology, and results, along with the limitations, the contributions, and the suggestions for the future work.

Chapter 2

Literature review

2-1- Particle shape definition

Shape includes all aspects of external morphology, which is the overall shape (form), roundness (smoothness/angularity) and surface texture (roughness). These parameters may change with no influence on the other ones, so they do not depend on each other, Figure 2-1 (Barrett, 1980). Form describes a particle size in different directions, roundness describes the corners of a particle, and surface texture describes the surface roughness or smoothness of a particle (Barrett, 1980).

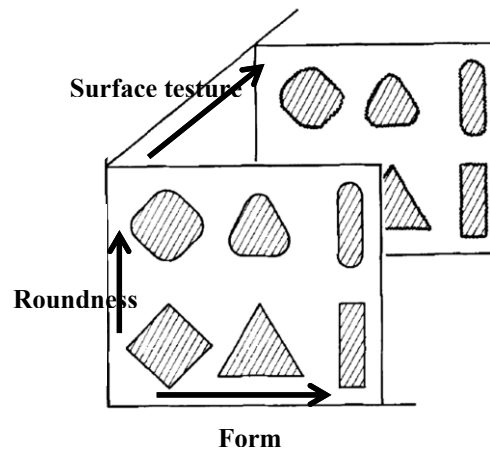


Figure 2-1 A simplified representation of form, roundness and surface texture (adapted after Barrett, 1980)

2-1-1- Description of shape

Since 1930, the shape (form) of particles is defined through different methods (Janoo, 1998). These methods assess the shortest, intermediate and longest lengths of particles, and use them to calculate the flatness and elongation ratios, or the shape factor (Janoo, 1998). Wadell (1932) described the flatness ratio (p) as the ratio derived by dividing the short length to the intermediate length, and the elongation ratio (q) as the ratio derived by dividing the intermediate length to the longest length. Shape factor (F) and sphericity are other parameters to study the shape of a particle (Janoo, 1998). The shape factor (F) is obtained by dividing the flatness ratio (p) by the elongation ratio (q) (Janoo, 1998), equation [2-1].

$$F = \frac{p}{q} \quad [2-1]$$

Based on Janoo (1998), if the shape factor is 1, then the particle has a rounded or cubic shape. If it is less than 1, then the particle is lengthened, slim, or needle like. Otherwise, the particle has a flat shape (Janoo, 1998). Sphericity was first defined by Wadell (1932) as the ratio of the surface area of a sphere which has the same volume as the particle in question, to the surface area of the particle, expressed by equation [2-2] (Wadell, 1932).

$$s/S = \text{Degree of true sphericity} \quad [2-2]$$

where s is the surface area of a sphere with the same volume as the particle, and S is the real particle surface area. The maximum value of this formula is 1 which is obtained of a particle with the same shape as a sphere. All shapes other than the sphere result in a value smaller than 1 (Wadell, 1932). In another description, Krumbein and Sloss (1963) described sphericity as the diameter of the largest possible inscribed sphere relative to the diameter of the smallest circumscribed sphere (Santamarina, 2004).

There are many other parameters for describing the shape of a particle; however, most of them use the longest, shortest and intermediate lengths of the particle (Barrett, 1980). Only a few of these techniques (Wadell, 1932) require the measurement of particle volume or surface area. While three-dimensional measurements are, in general, more representative of particle shape, they are often difficult to measure, especially with small particles (Barrett, 1980).

2-1-2- Description of roundness

The most complete way to measure roundness is to consider three perpendicular planes; however, it is possible just to take into account two planes or even just one plane. Thus, unlike sphericity, when working with small particles, roundness can be obtained only from one plane (Wadell, 1932). According to Wadell (1932), the maximum value that the curvature of a corner (r) may obtain is the radius of the maximum inscribed circle (R). Therefore, the roundness of such a corner is calculated through the ratio of r/R . The maximum value of this ratio is 1, and all other values would be less than 1. By taking the average of the roundness of all corners in a plane, the total roundness of the particle (Figure 2-2) will be obtained as (Jenson 2001; Barrett 1980; Janoo 1998 and Santamarina 2004):

$$\frac{\sum r}{N} = \text{Degree of roundness of a particle in one plane}, \quad [2-3]$$

where $\sum \frac{r}{R}$ is the sum of all corners' roundness value in a plane, and N is the corners number (Jenson 2001; Barrett 1980; Janoo 1998 and Santamarina 2004). Based on the give equation, the maximum roundness would be 1 for a particle with a spherical shape (Wadell, 1932).

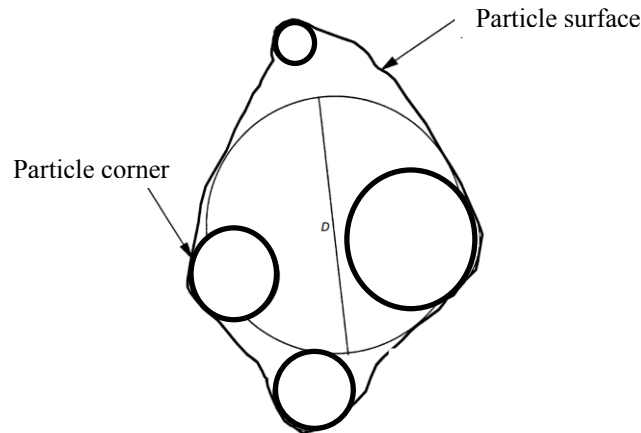
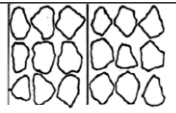
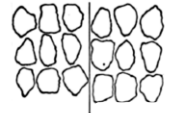
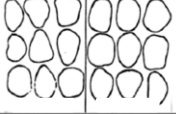
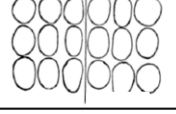


Figure 2-2 Wadell's procedure for evaluating particle (adapted after Sukumaran et al., 2001)

In practice, to evaluate the roundness of a particle, visual charts have been proposed due to the time consuming nature of the mentioned method (Janoo, 1998). The Krumbein chart (Table 2-1) shows five groups of roundness, including angular, subangular, subrounded, rounded, and well rounded. Each group has a range and an average value for roundness (Bareither et al., 2008). According to this chart, roundness has a range between 0.1 and 0.9. Values greater than 0.6, imply high roundness. Values between 0.4 and 0.6 imply medium roundness, and values lower than 0.4 represent low roundness (Janoo, 1998).

Another chart, modified from Krumbein and Sloss (1963), effectively characterizes sphericity and roundness together by visual comparison, as shown in Figure 2-3 (Santamarina, 2004 & Cho et al, 2006). Janoo (1998) reported that Lees (1964) concluded the Krumbein chart had some weaknesses. For instance, two different shape particles might get the same value for roundness, particularly when working with crushed particles. To solve this problem, Lees (1964) suggested another method by considering both the roundness of a corner, and its distance from the inscribed circle center, Figure 2-4 (Janoo, 1998).

Table 2-1 Roundness Categories based on Krumbein's work (adapted after Krumbein, 1941)

Roundness	Krumbein image	Rang	Average
Angular		0.10 - 0.26	0.18
Subangular		0.26 - 0.42	0.34
Subrounded		0.42 - 0.58	0.50
Rounded		0.58 - 0.74	0.66
Well-Rounded		0.74 - 0.90	0.82

Increasing roundness
↓

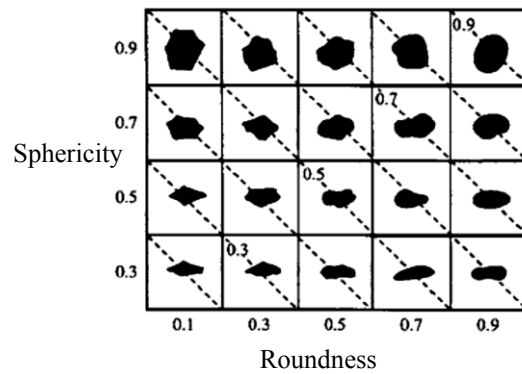


Figure 2-3 Particle shape determination—sphericity and roundness chart. particle regularity $\rho=(\text{roundness} + \text{sphericity})/2$ is constant along the dotted lines (adapted after Krumbein and Sloss 1963)

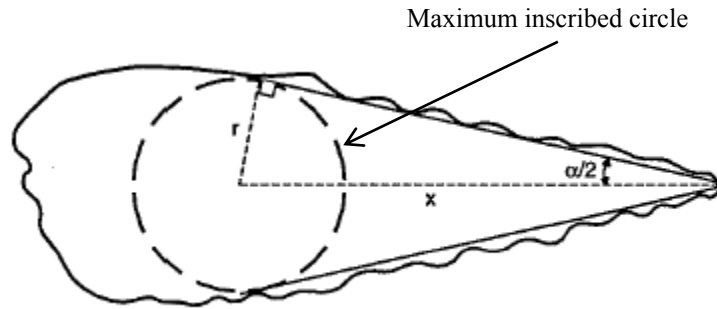


Figure 2-4 Parameters for determining the degree of angularity (adapted after Lees 1964)

Based on Lees work (1964), the degree of angularity may be calculated using the following equation (Janoo, 1998):

$$A_i = (180^\circ - \alpha) \frac{x}{r_{\max-in}} \quad [2-4]$$

where A_i is the angularity degree, α is the measured angle, x is the distance to the tip of the corner from the center of the maximum inscribed circle, and $r_{\max-in}$ is the radius of the maximum inscribed circle (Janoo, 1998). To calculate the total degree of angularity (A), one may add the angularity of all corners in three planes at right angles to each other. However, a visual chart was proposed by Lees (1964) to more easily estimate the angularity of a particle, Figure 2-5 (Janoo, 1998).

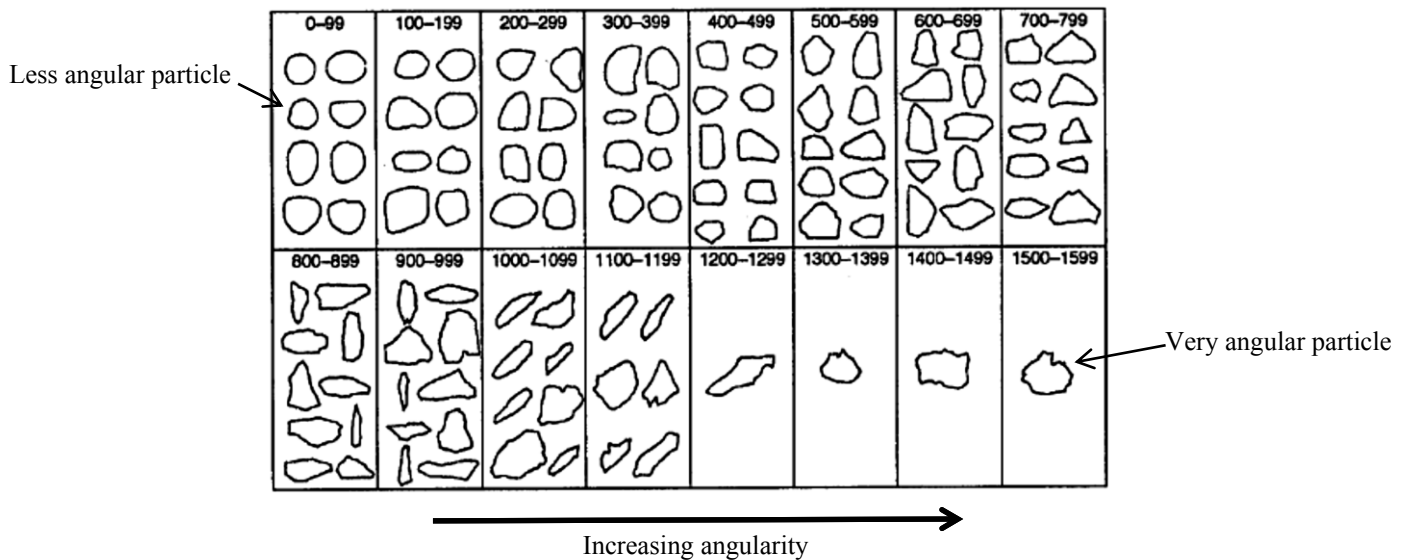


Figure 2-5 Angularity estimation chart (adapted after Lees 1964)

Although a number of charts have been developed to determine the sphericity and roundness of particles more easily and faster (Cho et al., 2006), the results of these methods may have a difference of only 0.1 and not greater than 0.2 (Santamarina et al, 2004).

2-1-3- Description of surface texture

Surface roughness characterise the surface of a particle (Jensen et al., 2001). Janoo (1998) and, Terzaghi and Peck (1967) described texture as smoothness or roughness of the particle surface, and used terms such as “smooth”, “sharp”, “gritty” to explain the surface of a particle. As reported by Janoo (1998), Barksdale and Itani (1994) developed a visual method to estimate the roughness of a particle surface ranging from 0 for very smooth particles to 1100 for very coarse particles. Bikerman (1964) developed another method, by covering a flat surface of a particle with asphalt and then removing it. In this method, still in use, the amount of the remaining asphalt indicates the particle texture and its degree of absorption (Janoo, 1998). In another method, proposed by Wright (1955), the surface of the particles was covered with synthetic resin, and then after drying, thin sections were prepared from the coated particles and studied under a projection microscope. The total length of the roughness was measured and matched with some chords to find their differences. The obtained difference was used as an indicator of the particle roughness (Figure 2-6). Although the accuracy of this method was acceptable, examining a number of particles to find the average roughness was required (Janoo, 1998).

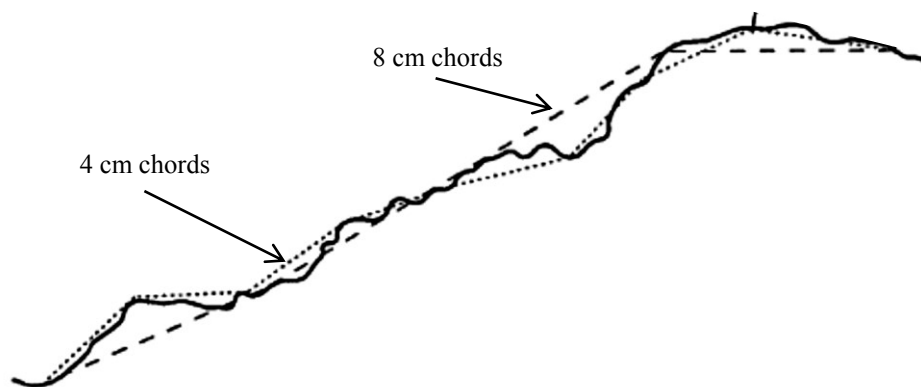


Figure 2-6 Measurement method for characterizing a particle surface texture (adapted after Wright 1955)

As described, it is very time consuming to measure roughness directly. Digital image analysis performs such measurements much easier by using Fourier, fractal, and other hybrid analysis (Santamarina et al, 2004). In these methods, a picture is taken from a particle via a high-resolution video, and then analysed with computer software to measure the particle roughness (Janoo, 1998).

2-2- Inter particle interactions

At the inter particle level, shear strength and particle movements may be affected by several parameters, such as packing and particle shape (Jensen et al., 2001). Packing is defined with void ratio, and is influenced by both shape and size distribution of particles, while shape is described through sphericity, angularity, and roughness of the particles (Jensen et al., 2001). Among these three parameters, angularity is the most useful parameter to define the shape of a particle. Of less importance among engineers is the roughness of an aggregate, since sphericity does not change very much for most granules (Jensen et al., 2001). At the inter particle level, the influence of particle properties such as shape, mean size, and size distribution has been long studied. Janoo (1998) reviewed the effect of particle shape on the behaviour of crushed material. He reported that when particles experience pressure, rounded particles slide one over another with less difficulties, while angular particles show a higher frictional resistance, and therefore, a lower displacement due to a greater internal friction coefficient (ϕ) (Janoo, 1998).

Jensen et al. (2001) used the discrete element method (DEM) to investigate the effect of particle shape on the shear behaviour of rough particles. They concluded that the packing capability and the internal friction angle (ϕ) of an assembly of sand are influenced intensely with angularity and roughness of particles. As the sand particles become more angular and exhibit a higher surface texture, the void ratio and likely the value of ϕ increase (Jensen et al., 2001).

Bareither et al. (2008) provided a multivariate regression model to estimate the internal friction angle of compacted sands in their study. Their model showed that the friction angle was affected by particle roundness, particle size, and packing characteristics. As roughness decreases or particle size increases, the internal friction angle increases (Bareither et al., 2008). As particles become more angular, they tend to interlock more and provide more resistance to the shear. Indeed, as mentioned earlier, the internal friction angle is higher for angular particles compared to round particles. McLemore et al. (2009) indicated that as the surface roughness increased, the value of

the angle of internal friction increased. But they suggested that these observations might be as a result of a low pressure that particles experienced during the test. They suggested that under a low pressure, the frictional resistance is controlled by the particle roughness, but at a higher pressure, the frictional resistance is influenced by the particle fracturing rather than the particle roughness (McLemore et al., 2009). This behaviour is common with the findings of Mair et al. (2002), and Guo and Su (2007).

Another modeling code, based on the discrete element modeling (DEM) developed by Mirghasemi et al. (2002), indicated that during compaction, angular particles generate a higher coordination number, which is the number of granules touching the particle in question. This higher coordination number will result in more stable contacts and less void space between particles which indicates that at the same magnitude of confining pressure, angular particles are more compressible (Mirghasemi et al., 2002).

Santamarina et al. (2004 and 2006) suggested that as angularity reduces, due to less interlocking and packing, maximum and minimum void ratios, as well as the difference between extreme void ratios ($e_{\max}-e_{\min}$) decrease. They also noted that at a low coordination number (loose packing; Figure 2-7), if particles have no restriction to rotate freely, they will show a great displacement under a low energy. In contrast, at a high coordination number (dense packing; Figure 2-7), the particles experience more difficulties to rotate, and thus show more tendency to reduce the coordination number to shear through sliding or dilation (Santamarina et al., 2004 and 2006). Santamarina et al. (2004) concluded that resistance to particle rotation is increased by angularity, sliding is delayed by roughness, and dilatancy and anisotropy are increased by both, angularity and roughness. This range of conditions is common with the findings of Mirghasemi et al. (2002).

In terms of size distribution, Morgan (1999-A&B, and 2000) performed a number of numerical simulations to study the effect of size distribution and the internal friction coefficient on mechanical behaviours. He found that the influence of the particle size distribution arises when deformation is a function of sliding and rolling. Based on his research, the contact directions and the normal/shear forces control whether sliding or rolling will occur (Morgan, 1999-A).

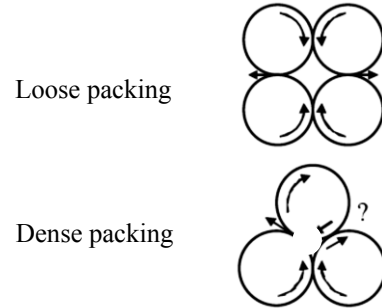


Figure 2-7 Rotational characteristics in loose and dense packing (adapted after Santamarina and Cho, 2004)

Results of Morgan’s DEM simulations on rounded particles of the same size demonstrated that in a low internal friction, more sliding is developed at the particle contacts than rotation, while in a high internal friction, displacements will happen due to rolling, resulting in a higher dilation, since sliding is restricted (Morgan, 1999-A). However, in systems with various particle sizes, the numerical models (Morgan, 1999-B) showed short phases of distributed shear, and counter-rotation (opposite to the sense of shear) of some grains. In a low range size distribution system with a high number of large granules in contact, although the number of granules rotating in a synthetic direction is high, the granules with antithetic rotation can still be found all over the system (Morgan, 1999-B). For low range size distribution systems, the percentages of rolling particles were high in both synthetic and antithetic directions. This high percentage is because the number of particles rolling in the synthetic direction is approximately equal to the number of particles rolling in the antithetic direction, resulting in a high magnitude of frictional forces at the contacts (Morgan, 1999-B). High frictional forces at the contacts of large particles influence a vast area, and provide an approximately extensive diffuse slip area, Figure 2-8 (Morgan, 1999-B).

Systems with a high percentage of small particles present a huge number of rolling particles, developing chains with particles rotating in the synthetic or antithetic directions (Morgan, 2000). In systems with a combination of both small and large particles, the small particles, usually with the antithetic rotation, separate the large particles, mostly with the synthetic rotation, by creating some vertical chains, Figure 2-8-b (Morgan, 1999-B). Thus, in the systems with moderate to wide size distributions, the contact of large particles will be minimized, and the frictional force will be generated mostly due to the small particle contacts adjacent to the initial shear area (Morgan, 1999-

B). In such systems, the small particles act like a lubricant, resulting in a reduced frictional force between the particles (Morgan, 2000).

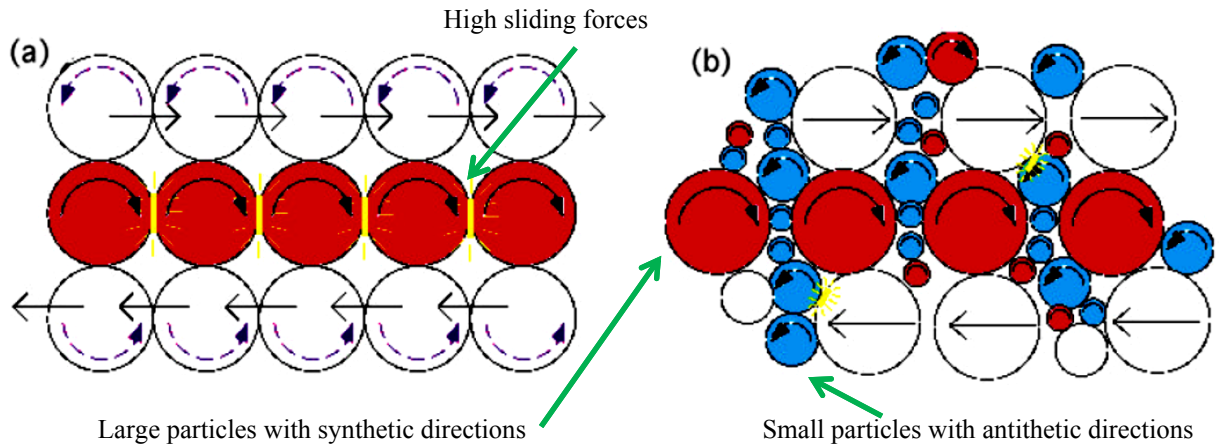


Figure 2-8 Inter-particle rolling model (a) Low range assemblages; (b) wide range assemblages (adapted after Morgan, 2000)

When angular grains are present, rolling may be inhibited, so the particles move one over another through sliding (Morgan, 2000). The simulation results by Morgan (2000) showed that adding a small number of angular particles has little effect on the shear behaviour of material. However, Nataliya et al. (2010) found that adding a small number of rolling particles in an assembly with mostly angular particles significantly influenced the material shear behaviour.

In another study, Mair et al. (2002) suggested that the stability of an assembly of material under the shear forces depends on the stress chains generating between the particles (Figure 2-9). These chains may consist of a few particles, each carrying a moderate to high shear load, or a diffuse zone of the particles, each carrying a low to moderate load (Figure 2-9-a), and are stable only at a critical angle (ϕ_c) (Figure 2-9; b, c and d). This angle is larger for the diffuse chains and smaller for the localized chains. When the orientation of a chain passes this angle, the chain fails. Then, immediately, another chain will be generated to support the shear load (Mair et al., 2002). Failure of a chain results in a drop in the dynamic stress and an unstable stick-slip sliding (Mair et al., 2002).

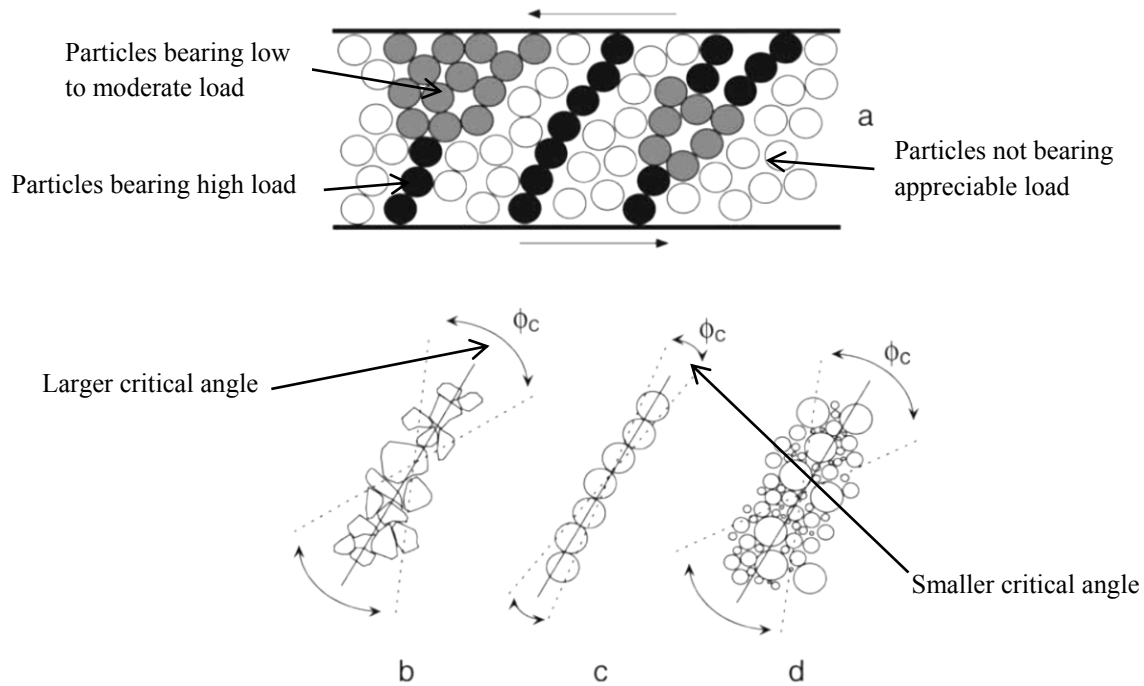


Figure 2-9 (a) Force chains generated in the particles sliding between two layers, critical angle in angular particles (b), narrow particle size distribution rounded particles (c), and wide particle size distribution rounded particles (d) (adapted after Mair et al., 2002)

Mair et al. (2002) hypothesized that assemblies with a greater coordination number, such as angular materials or materials with a wide size distribution, create extensive diffuse zones, and therefore have a wider critical angle. In contrast, in systems with a small coordination number, such as rounded particles, a localized chain with a tighter critical angle is more probable to be created (Mair et al., 2002). Figure 2-10 illustrates friction as a function of shear displacement for angular and spherical particles at a normal stress of 5 MPa. The breakage of particles is negligible at this stress for both the angular and spherical materials. The spherical particles show a lower value of friction coefficient and the stick-slip behaviour, whereas the angular particles slide stably with a higher friction (Mair et al., 2002).

This idea is consistent with those of Anthony et al. (2005), who showed how spherical particles shear between rough surfaces by dividing the particles into three groups (Figure 2-11): particles along boundary sides (light grey), particles that create the force chains and carry the loads (dark grey), and particles with no load (white). By shearing two surfaces, the force chains are generated and carry the load; by continuing the shearing, the force chains deviate from their stable orientation, and in some cases fail, resulting in slip localization. As soon as a set of the force chains

collapse, a new group of chains is generated to carry the load (Anthony et al., 2005). According to Anthony et al. (2005), the generated force chains have the angle of 45° to the shear surfaces.

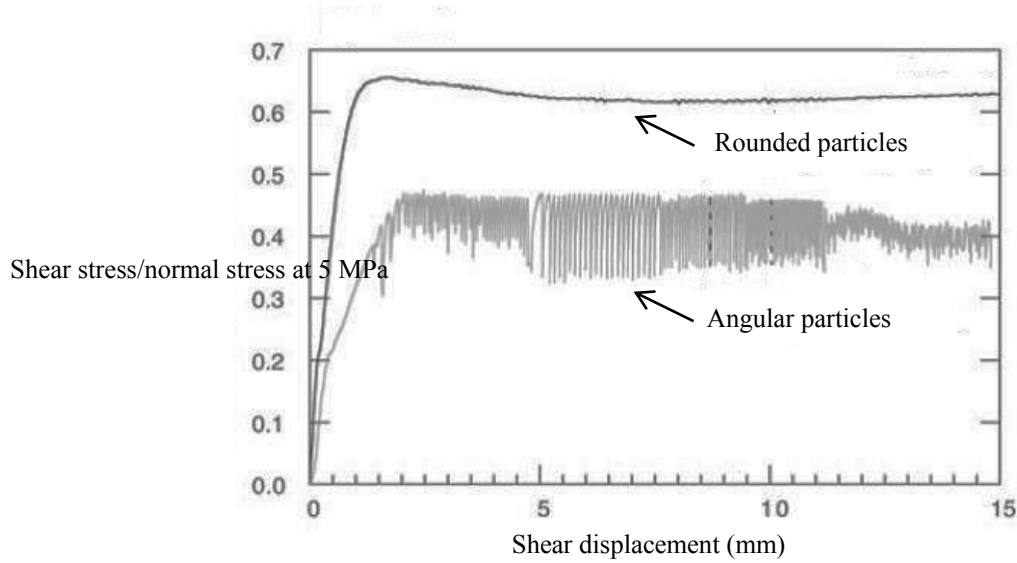


Figure 2-10 Friction as a function of shear displacement for angular and spherical grains at $\sigma_n = 5$ MPa (adapted after Mair et al., 2002)

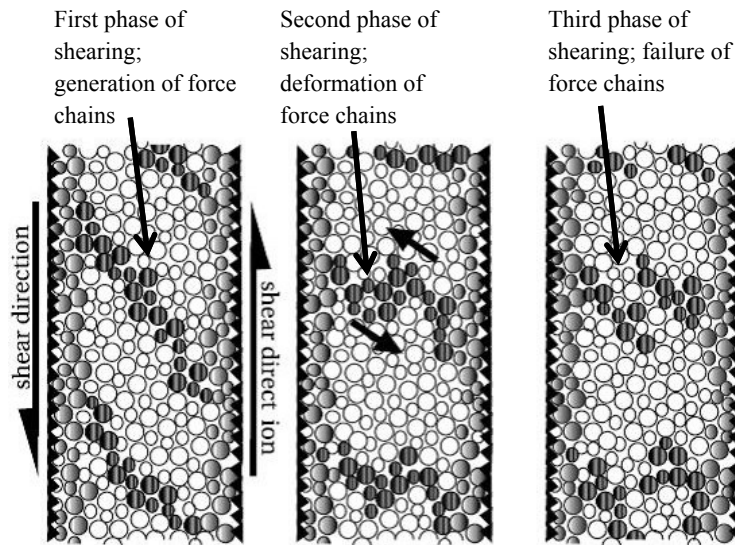


Figure 2-11 Schematic diagrams of spherical glass beads deforming as they are sheared between rough boundaries (adapted after Anthony and Marone, 2005)

Anthony et al. (2005) found that parameters such as particle shape and size directly influence the frictional behaviour of the material. They showed that an increased angularity or roughness of the particles resulted in an increased frictional strength and an extended diffuse zone in the area between the two shearing surfaces (Anthony et al., 2005). The following explains their findings based on Anthony et al. (2005):

Figure 2-12-a and Figure 2-12-b show a set of spherical and angular particles shearing between two smooth surfaces, respectively. In Figure 2-12-a the shear is limited close to the shearing surfaces, while in Figure 2-12-b shearing occurs through sliding and rotation of the particles along the shearing surfaces. Comparing the behaviour of the particles in the mentioned cases indicated that the frictional strength is higher in the angular particles, because they cannot move past one another easily, like the spherical particles, and thus become interlocked due to the roughness of the surrounded particles. Therefore, the mode of motion of the spherical particles is mostly rolling and sliding with little resistance, while the angular particles displace through dilation (Anthony et al., 2005).

Figure 2-12-c and Figure 2-12-d show the spherical and angular particles shearing between two rough surfaces, respectively. Figure 2-12-c shows that there is a thin layer of particles rolling and rotating along the shearing surfaces, and the stress is carried through the localized chains. In Figure 2-12-d the thickness of layers along the shearing surfaces are increased and the force chains become wider and more frequent due to the interlocking of the angular particles. These changes will result in the more stable force chains, and therefore a reduction of the sudden chain failures (Anthony et al., 2005).

In addition of the shape and size distribution effects, the influence of particle size has been studied in different engineering areas, specifically concrete, rocks, or soils (Hu et al., 2011). The findings indicated that an increased particle size results in a reduced friction angle, and therefore, the material shear strength (Hu et al., 2011). However, the experimental findings by Fakhimi et al. (2008) suggested that increasing the number of oversized particles will increase the internal friction angle.

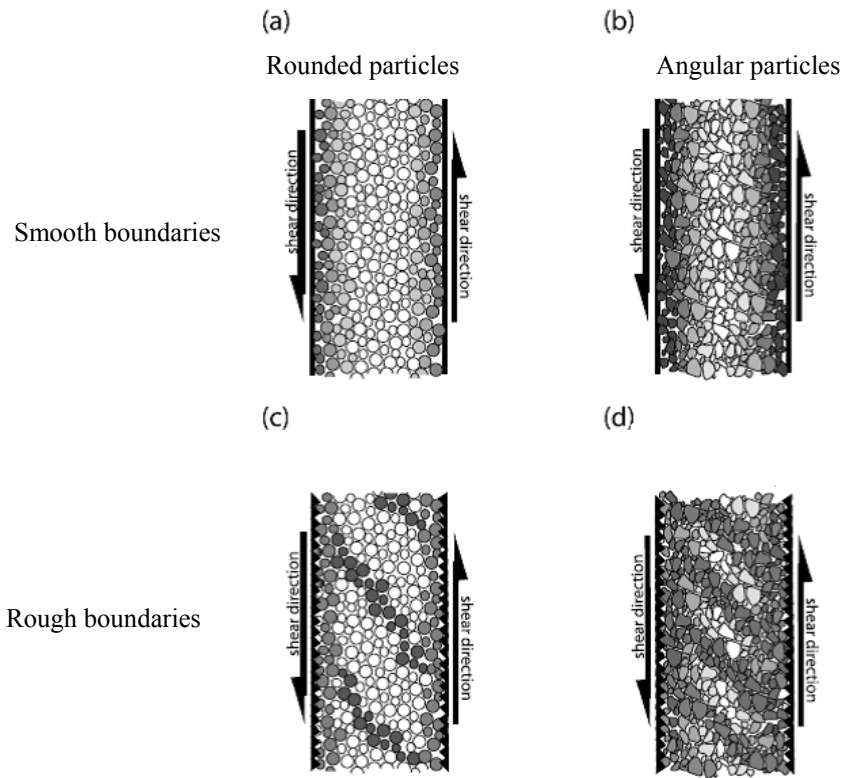


Figure 2-12 Schematic diagrams of spherical and angular grains sheared between smooth and rough boundaries (adapted after Anthony and Marone, 2005)

In application to slope stability consideration, Bandis and Barton (1981 & 1982) noted that despite equal joint roughness, the shear strength of a small block mass may be higher than that of a large block mass due to the mass stiffness of blocks. Small blocks have a higher degree of freedom, and so have more chance to rotate and make more contacts with each other, while large blocks have more difficulties in rotating, and so have less contact areas and thus less strength in comparison to the small blocks, Figure 2-13 (Bandis et al., 1981 & 1982).

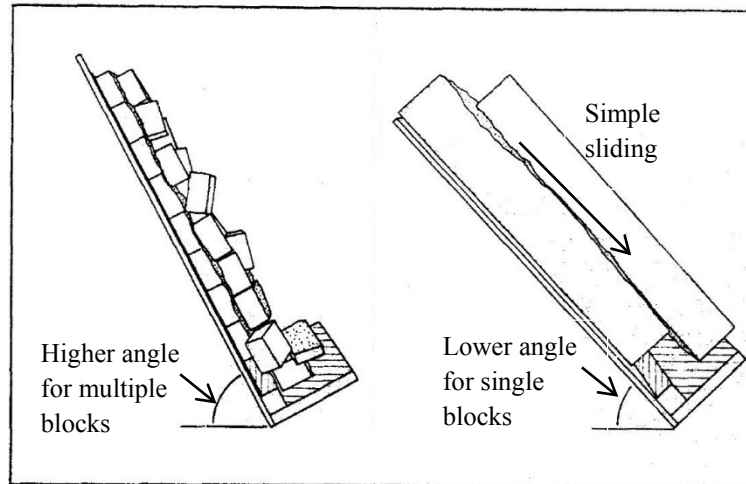


Figure 2-13 Tilt tests with multiple blocks indicate higher strength than with large single blocks

(adapted after Bandis et al. 1981&1982)

2-3- General modes of rock mass motions in rock slopes

There are different methods of rock mass (stones, rocks, and blocks) movement in slopes where each mode of motion may be described by dynamic equations (Petje et al., 2006). Based on the ground slope, a particle may move with different modes, when it is separated from the original rock mass (Dorren, 2003). The most significant modes of motion of granular material are sliding, rolling, bouncing, and freefall, which are discussed in the following sections (Dorren, 2003).

2-3-1- Free fall

Free fall is a movement in the air with no contact with the ground, and happens when the slope angle is greater than 76° (boundary value is 70°) (Petje et al., 2006). A free fall contains two motions: moving the center of the particle, and rotation of the particle around its centre (Dorren, 2003). At the time the particle hits to the ground, the free fall mode of motion will be changed into the other modes (Spang et al., 1987). Particles are mostly not rounded; therefore, after hitting the ground, they may follow different trajectories, Figure 2-14 (Dorren, 2003). Then, the particle will continue its movement with the new mode of motion until it stops, experiences another hit, or experiences a change in the ground slope (Spang et al., 1987).

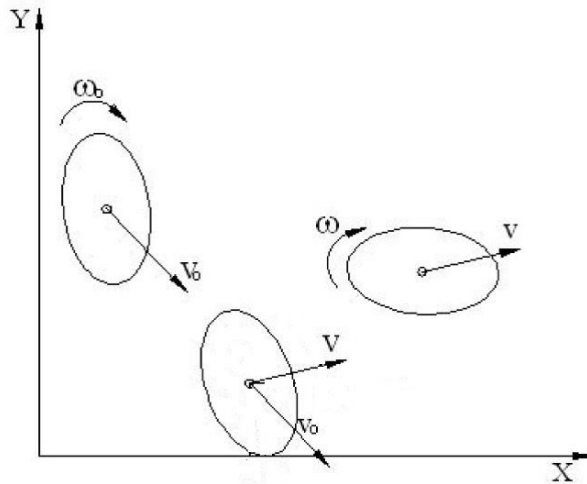


Figure 2-14 Rock block before and after the impact (adapted after Petje et al., 2006)

2-3-2- Bouncing

Hitting a particle in the free fall mode of motion to the ground due to the changing the ground slope is called bouncing. After the first bounce, the particle will lose a huge portion of its energy (Dorren, 2003). Based on the experimental analyses, the new mode of motion after bouncing is a function of the particle shape, geometry of the ground, and the amount of energy loss after the collision (Petje et al., 2006). Figure 2-15 illustrates the locations of a particle during bouncing with arrows specifying the contact points between the particle and the ground (Bozzolo et al., 1986). Figure 2-15-a and Figure 2-15-b show contacts on a hard surface. At this condition, the tangential component of the velocity at the contact point is close to zero (Bozzolo et al., 1986). Figure 2-15-c illustrates contacts on a soft surface that causes a small amount of sliding at the contact point (Bozzolo et al., 1986).

Field observations of rock-fall mechanisms showed that when a particle moves on a slope, it may cause displacements in the other particles (Bozzolo et al., 1986). Movements of the other particles happen if the slope angle is at least equal to the dynamic friction coefficient of the particles ($\tan^{-1}(\mu)$) (Petje et al., 2006). Moreover, if the surface is covered with particles of the same size of the moving particle, the mode of motion after collision will be a number of bouncing (Bozzolo et al., 1986)

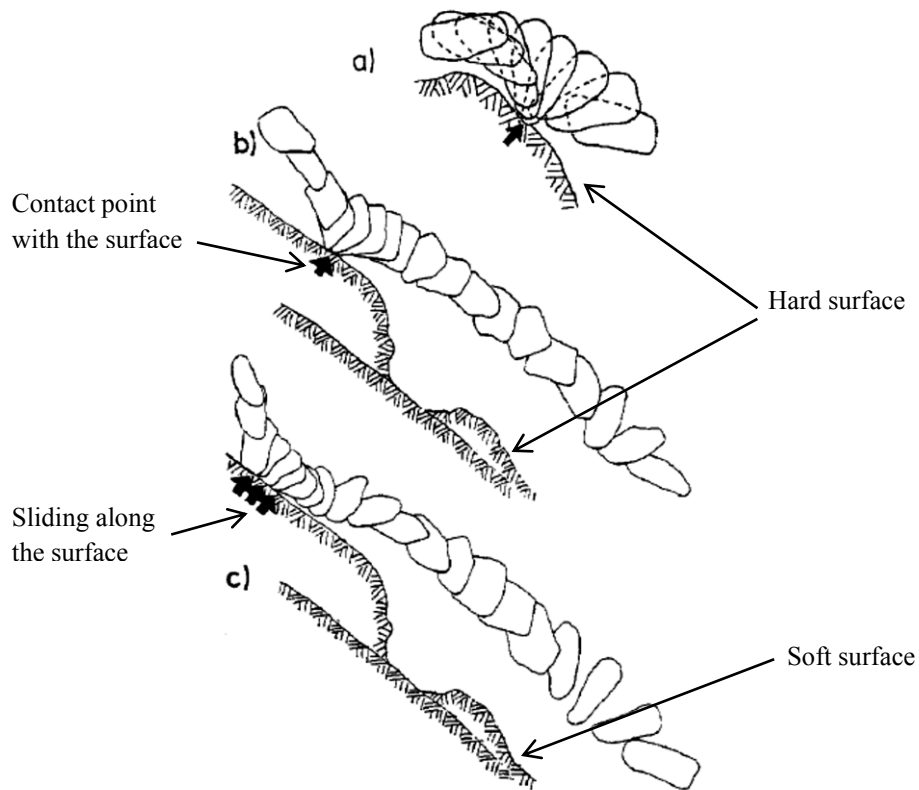


Figure 2-15 Sequences of rock positions (adapted after Bozzolo et al., 1986)

2-3-3- Rolling

In flatter slopes with angles less than 45° , the mode of motion changes into rolling. In rolling, a particle rotates, and will be always in contact with the surface from its largest radius (Petje et al., 2006). “Rolling occurs when the vertical projection of the centre of gravity is outside the polygon defined by the contact surface” (Petje et al., 2006). Rolling is similar to toppling by considering the influence of the ground geometry (Petje et al., 2006).

Rolling occurs when slope angle β is greater than $180/n$ (n is the sum of the vertices of polygonal prism at the top or bottom side), and the friction coefficient is larger than $\tan(\beta)$ (Petje et al., 2006). If the friction coefficient is less than $\tan(\beta)$, sliding occurs instead of rolling (Petje et al., 2006). In reality, it is unlikely to have a pure rolling, because most particles do not have a spherical shape, and most surfaces are not smooth. In such conditions, the mode of motion will be very complicated, probably a mixture of bouncing and rolling (Petje et al., 2006).

2-3-4- Sliding

Sliding is another mode of motion over the slope surface. In sliding, particles lose the energy due to the dynamic friction which is in relation with the surface slope; reducing the surface slope results in a higher amount of energy loss (Spang et al., 1987). It is important to highlight the role of static friction. Static friction is a parameter that determines, in the case of sliding, if sliding is the first mode of motion, and in the case of rolling, if there will be rolling or a mixture of rolling and sliding (Spang et al., 1987). In rolling, energy is lost due to the rolling resistance, and not because of the friction (Spang et al., 1987). Meanwhile, in sliding, if the surface slope is not changed, the particle will come to rest due to the friction (Dorren, 2003). Sliding initiates when the friction coefficient is less than $\tan(\beta)$; in this mode, the particle is continuously in contact with the ground (Petje et al., 2006).

2-4- Dipper-ground interactions

In cutting or digging a material, the machine needs to apply a force greater than the resistive force of material (Hemami et al., 1994). It is necessary to understand this resistive force in order to provide a better equipment design and machinery automation (Hemami et al., 1994). Therefore, it is essential to define a relationship between the resistive force, the material properties, the tool geometry, and the motion of the equipment, as illustrated in Figure 2-16 (Blouin et al., 2001).

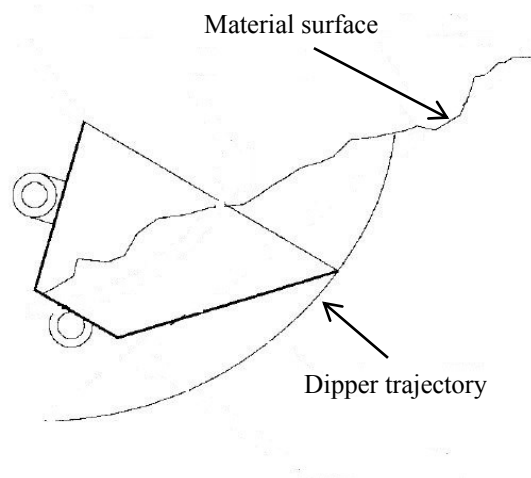


Figure 2-16 Two-Dimensional View of Excavation (adapted after Blouin et al., 2001)

2-4-1- Factors influence resistive force

Resistive force that a cutting tool experiences during a dig action is a function of the material properties, the shape and size of the tool, and the motion of the cutting tool (Hemami et al., 1994). The following discussion describes how these parameters influence the resistive force.

2-4-1-1- Earthmoving actions

The interaction between an excavation tool and a medium is not the same in the actions of penetration, cutting, and excavation (Lipsett et al., 2011). Penetration is defined as the action of inserting a rigid tool with a constant direction into a medium (Lipsett et al., 2011), as shown in Figure 2-17-a. A penetration tool usually has a blade shape with a controllable depth of operation (Lipsett et al., 2011). Cutting is linear, rotational or a combination of both motions applied by a rigid blade shape tool, Figure 2-17-b. The orientation, depth of penetration, and the speed of the tool is constant in a cutting action (Lipsett et al., 2011). Based on the width of the blades, there might be side effects, thus blades are categorized into three groups of the narrow, wide, and very wide blades, where a wide blade refers to a blade with the width double the depth, and a very wide blade refers to a blade with the width more than six times the depth (Lipsett et al., 2011). In this discussion, excavation is referred to the extraction of a medium with a bucket or a dipper of a shovel, namely a loading task in the mining industry. The motion executed by such a tool consists of a complex mixture of penetration, cutting, and scooping, Figure 2-17-c (Lipsett et al., 2011).

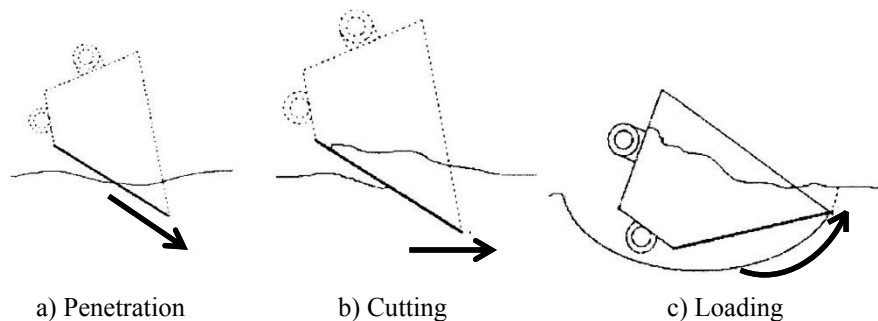


Figure 2-17 Fundamental earth moving actions (adapted after Blouin et al., 2001)

2-4-1-2- Material properties

The medium is another parameter that influences a cutting or digging action and includes clay, granules, soil, or a combination of them (Blouin et al., 2001). Clay is made of very fine particles with cohesion and plasticity. Granules are cohesion-less adhesion-less hard broken particles with various sizes. Soil is a combination of loose sediments and water (Blouin et al., 2001).

According to Blouin et al (2001), a medium may be described through a number of characteristics. Density describes how a tool and the medium act together. Regarding friction, there are two types: internal friction related to the material components, and one of the inherent characteristics of the material; external friction related to the friction between a tool and the material, and the way they interact together. Internal friction is approximately equal to the angle of repose of the granular un-compacted material. Cohesion is defined as the resistance a material shows to separate its particles. Adhesion is a function of the water content and the internal friction, and defines the interaction of a tool and the medium (Blouin et al., 2001).

2-4-1-3- Tool Properties

Based on the previous studies, the properties of the cutting tool including the size and shape of the tool, whether the tool has equipped with teeth or not, and the angle at which the tool cuts or digs the medium (Figure 2-18) influence the performance of the cutting tool (Hemami et al., 1994).

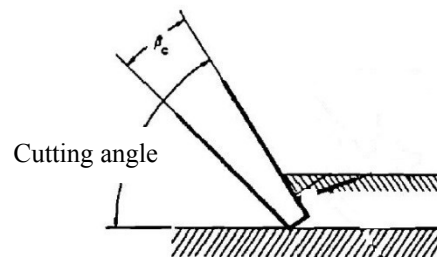


Figure 2-18 Definition of cutting angle (adapted after Hemami et al., 1994)

2-4-1-4- Mode of application

There are different modes of application based on the type of equipment, such as cutting cohesive material or pushing a non-cohesive medium through a grader or a bulldozer (Figure 2-19-a), applying a curvature penetration through a back-hoe (Figure 2-19-b), or cutting and scooping

through a loader (Hemami et al., 1994). The forces and the methods of analysing each type are different. Moreover, different approaches such as theoretical, experimental, or combination of both may lead to different results (Hemami et al., 1994).

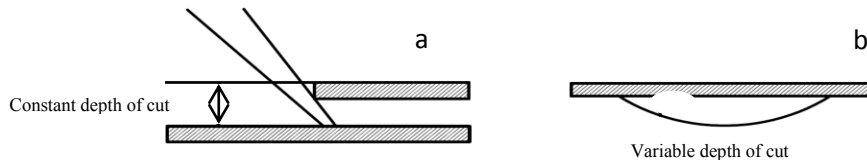


Figure 2-19 Definition of depth of cutting, a) constant (bulldozer) b) variable (back-hoe) (adapted after Hemami et al., 1994)

2-4-2- Common hypothesis of material properties

In order to analyse applications such as digging, penetrating, and cutting, it is necessary to make the following assumptions (Blouin et al., 2001):

- Material is homogeneous, having the same properties all over the medium, such as rocks and sands.
- Material is continuous, having for instance no void space in the medium.
- Material is isotropic, behaving similarly in all directions of an application.

2-4-3- Dipper-ground interaction models

2-4-3-1- Penetration models

The resistive forces that a tool experiences during a cut or a penetration are similar. Moreover, in reality, to assess the cutting forces, a penetration tool may be employed (Blouin et al., 2001). Thus, to have a better understanding of the penetration models, it is recommended to study the cutting models.

2-4-3-2- Cutting models

When equipment cuts or penetrates a medium, it causes a failure that is best described through shear stress or shear strength theories (Shi, 2007). Some parameters such as shear strength of the

material and the direction of ruptures in the medium influence the required force to create this failure (Blouin et al., 2001).

Two common shapes for this failure are assumed to be a curved or logarithmic shape, Figure 2-20 or a flat shape, Figure 2-21. Although graphical or empirical approaches are required to describe a curved failure, common physical parameters may be used to characterize a flat failure, parameters such as speed (v), cutting angle (β), penetration depth (d), shear plane angle (ρ), blade width (w), surcharge (q), and blade length (l), as illustrated in Figure 2-21, (Blouin et al., 2001).

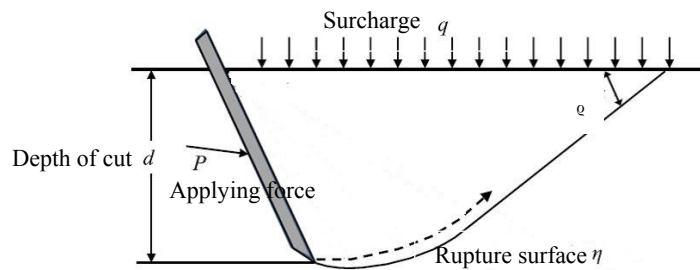


Figure 2-20 2D Logarithmic spiral rupture approach for cutting soft ground (adapted after Osman, 1964)

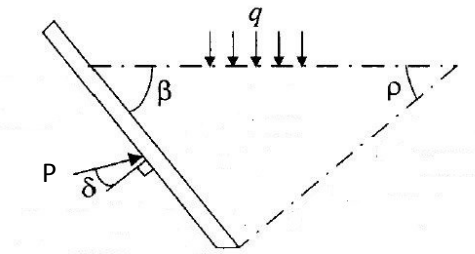


Figure 2-21 Static equilibrium approximation of a failure surface (adapted after Blouin et al., 2001)

Coulomb (1779) noted that there are two parameters to describe the material shear strength: friction that is relative to the pressures acting at right angles to the shear surface, and cohesion (Lipsett et al., 2011). Coulomb's equation for medium-medium and tool-medium interactions may be written as equations [2-5] and [2-6], respectively (Blouin et al., 2001).

$$\tau_{mm} = C + \sigma_n \tan (\varphi) \quad [2-5]$$

$$\tau_{mt} = C_a + \sigma_n \tan (\delta) \quad [2-6]$$

where τ_{mm} and τ_{mt} are shear strengths regarding the medium-medium and medium-tool interactions, respectively, σ_n is normal pressure, ϕ and δ are internal and external friction angles, respectively, C is cohesion, and C_a is adhesion (Blouin et al., 2001).

While the Coulomb method assumed that the material failure was a flat shape, a model to calculate the stresses at the various failure surfaces in a stable and homogeneous system was proposed by Mohr (Blouin et al., 2001). However, Coulomb's and Mohr's theories are not appropriate for all cases, for example, when the excavation tool moves with various speeds, or where the medium is made of individual particles (Blouin et al., 2001). As reported by Raza et al (2013), Terzaghi (1943) used the passive earth pressure theory, and proposed a theory as the fundamental of the universal earthmoving equation (UEE), for the bearing capacities of materials at shallow bases as shown in equation [2-7]:

$$Q_u = 0.5\gamma B N'_\gamma + C N'_c + q N'_q \quad [2-7]$$

where γ is the soil density; B is the width of foundation; N'_γ , N'_c , N'_q are the N-Coefficients for Terzaghi's model (values depend upon the internal friction angle (ϕ)), and q is the surcharge pressure perpendicular to the soil surface (Raza et al., 2013).

According to Shi (2007), Osman (1964) used the passive pressure theories of Coulomb (for granular material) and Ohde (logarithmic spiral model) to investigate the cutting action via a wide blade. In Osman's theory, a blade cut a soil by applying force P at the depth of d , while experiencing the resistive force of q . The blade causes a failure curvature of line η with angle of ρ to the horizon, and follows a logarithmic spiral trajectory, as illustrated in Figure 2-20 (Shi, 2007). Osman's theory can be written with dimensionless parameters as equation [2-8] (Heitiaratchi et al., 1966):

$$\frac{P}{\gamma d^2} = f\left(\frac{c}{\gamma d}, \frac{c_a}{\gamma d}, \frac{q}{\gamma d}, \phi, \delta, w\right) \quad [2-8]$$

where ϕ , γ and C are the soil properties, δ and C_a are the soil/interface properties, w and d are the interface geometry, and q is the surcharge pressure perpendicular to the soil surface (Heitiaratchi et al., 1966).

Reece (1965) found that the cutting mechanism is comparable to Terzaghi's theory (Shi, 2007), and suggested to rewrite Osman's equation as expressed in equation [2-9] (Heitiaratchi et al., 1966):

$$P = (\gamma g d^2 N_\gamma + C_d N_c + C_a N_{ca} + q d N_q) w \quad [2-9]$$

where material response is described through gravitational, cohesive, adhesive, and surcharge factors, respectively. The N coefficients are constant values related to the failure envelope shape and thus, are the functions of the internal and external frictions, and the shape of the cutting tool (Heitiaratchi et al., 1966). Reece's equation did not consider the inertia forces; therefore, it may only be used in conditions where the speed of the cutting tool is very low (Heitiaratchi et al., 1966). To estimate the N coefficients, a set of charts was provided by Hettiaratchi and Reece (1974); however, this method works unsatisfactory for repetitive modeling's (Shi, 2007). Based on Blouin et al. (2001), the best equation to model the cutting application is the one initially proposed by Reece (1965), and then reviewed by McKyes (1985), that includes individual terms to show the influence of weight, cohesion, adhesion, surcharge, and inertia (N_γ , N_c , N_{ca} , N_q , and N_a , respectively) as equation [2-10] (Blouin et al., 2001):

$$P = (\gamma g d^2 N_\gamma + C_d N_c + C_a N_{ca} + q d N_q + \gamma v^2 d N_a) w \quad [2-10]$$

This equation may be written in detail as equation [2-11]:

$$P = \frac{w d}{\cos(\beta + \delta) + \sin(\beta + \delta) \cot(\rho + \varphi)} \left[\frac{\gamma g d (\cot \beta + \cot \rho)}{2} + q (\cot \beta + \cot \rho) + c (1 + \cot \rho \cos(\rho + \varphi)) + C_a (1 - \cot \beta \cot(\rho + \varphi)) + \frac{\gamma v^2 (\tan \rho + \cot(\rho + \varphi))}{1 + \tan \rho \cot \beta} \right] \quad [2-11]$$

This equation may be used in different fields such as “blade cuts, wire cuts, pile driving, and chisel-plough-wing cuts” through employing appropriate terms of the equation (Blouin et al., 2001). For a cable shovel dipper working with blasted rock, it only requires the exclusion of cohesion, surcharge and inertia factors. Moreover, as the tool surface is normally very smooth in contrast to the material, so that the adhesion is not significant and the related component in cutting force resistance is often neglected. Therefore, the earthmoving equation can be rewritten as equation [2-12]:

$$P = (\gamma g d^2 N_\gamma) w = \frac{wd}{\cos(\beta+\delta)+\sin(\beta+\delta) \cot(\rho+\varphi)} \left[\frac{\gamma g d (\cot \beta + \cot \rho)}{2} \right] \quad [2-12]$$

2-4-3-3- Loading Models (extraction of a medium with a dipper)

When a cutting tool changes from a blade into a dipper, the number of forces acting on the tool will be increased due to the side and bottom walls of the bucket (Blouin et al., 2001). The experimental and analytical methods have been used to model these resistive forces that include the cutting forces at the bucket teeth, and the excavation forces to move the material inside and in front of the dipper (Raza et al., 2013).

Some of the earlier studies were carried out by Dombrovskii and Pankratov (1961), who developed an equation to estimate the lateral digging force by summing the resistive force to cut the material, the friction force between the material and the tool, and the resistive force to move the material inside and in front of the bucket (Raza et al., 2013). Afterwards, Alekseeva et al (1985) modified their equation as equation [2-13] (Raza et al., 2013):

$$P = dwk_1 \quad [2-13]$$

where k_1 is the specific dig resistance, refers to the all resistive forces, and is obtained experimentally for each material (Raza et al., 2013).

Balovnev (1983) modeled the cutting resistance on a dipper by combining the Universal Earthmoving Equation and the passive earth pressure theory, and expressed an equation containing the fundamental forces applying to the different bucket walls (side walls, back wall, etc.) (Raza et al., 2013). These force components include P_1 that is the resistive force of the cutting edge, P_2 that is a resistive force to wear on the edge, P_3 that is the resistive force on the side walls, and P_4 that is the friction force on the side walls (Blouin et al., 2001). Zelenin et al. (1985) investigated the effect of each parameter on the cutting force on a dipper without a tooth, and proposed an empirical expression as equation [2-14] (Blouin et al., 2001):

$$P = 10C_o d^{1.35} (1 + 2.6w)(1 + 0.0075\beta)(1 + 0.03s)e_z k_z \quad [2-14]$$

where C_o is compactness, s is the cutting edge, e_z is the tool plate thickness, and k_z is the cutting type. Zelenin et al. (1985) believed that if a dipper is equipped with teeth, those teeth would

decrease the influence of the dipper side walls, thus the cutting force equation may be written as equation [2-15] (Raza et al., 2013):

$$P = 10C_o d^{1.35} (1 + 2.6w)(1 + 0.0075\beta)z \quad [2-15]$$

where z indicates the influence of blade (Raza et al., 2013). Although these equations seem very complicated, to date nobody has examined them for a verification or disapproval (Blouin et al., 2001). Wu (1995) developed a model to evaluate the resistive forces on a dragline bucket using Rowland's model (1991) (Raza et al., 2013). His model included the frictional forces on the teeth, lip, and dipper walls, and also, the weight of material inside the dipper which all applying on the dipper tip in a static condition (Raza et al., 2013). Different approaches were employed to calculate each of the mentioned components; for instance, the material loaded into the dipper was used to assess the bottom wall frictions; the passive earth pressure theory was used to estimate the side wall frictions; Hettiaratchi and Reece's work (1994) was employed to calculate the teeth and lip frictions; and the maximum capacity of the dipper was used to calculate the payload weight (Raza et al., 2013). Hemami (1994) investigated the forces applied on a dipper while digging a rockpile, and categorised them into six components. These forces, denoted by F_1 to F_6 in Figure 2-22, are expressed in equation [2-16] (Hemami, 1994):

$$F = F_1 + F_2 + F_3 + F_4 + F_5 + F_6 \quad [2-16]$$

F_1 : to overcome the material weight inside and in front of the dipper with various amount and acting points during a dig cycle (Hemami, 1994).

F_2 : to overcome the resistive force of the material in front of the dipper due to the compaction when the dipper tries to make room to move forward into the rockpile. The magnitude of this force will be zero in case of the lake of the compaction role of the dipper (Hemami, 1994).

F_3 : to overcome the frictions between the material and the dipper walls. The direction of this force is common with direction of the dipper velocity, and its magnitude is always greater than zero (Hemami, 1994).

F_4 : to overcome the material resistance to be cut and loaded into the dipper that acts along the cutting edges (Hemami, 1994).

F₅: to overcome the inertia force of the material inside and in front of the dipper, with zero magnitude in case of an unchanged dipper speed during a dig cycle (Hemami, 1994 and Raza et al., 2013).

F₆: to overcome the weight of the empty dipper (Hemami, 1994)

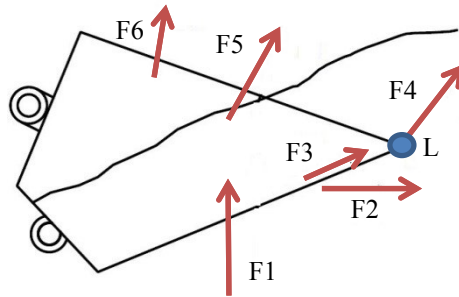


Figure 2-22 Loading Force Components during Digging Task (adapted after Blouin et al., 2001)

The direction of the forces illustrated in Figure 2-22 specifies a particular time, which means the direction and magnitude of the forces, except F₁, change during a dig cycle (Blouin et al., 2001). The direction of F₁ is always vertical, because it indicates the weight of the material inside the dipper. The direction of all other forces depends on the orientation of the dipper (Blouin et al., 2001). When analysing the forces of a dipper moving at a rockpile, an alternative way might be helpful (Blouin et al., 2001). In such a case, a good solution is to divide F₁ into two components, one perpendicular to the rockpile slope, and another one parallel to the slope. The first component may act similar to F₁ as illustrated in Figure 2-22. The second component may be added or deducted from the moving force of the dipper generated by the equipment, depending on the direction of the digging action (upward or downward) (Blouin et al., 2001). Hemami (1994) suggested the acting point of the total force F is the lip of the dipper (point L in Figure 2-22). In general, four parameters influence the mentioned force components, including material properties, dipper size and shape, dipper motion, and environmental conditions such as temperature and gravity. The dipper motion indicates the movement orientation of the dipper, and is referred to as the dipper trajectory (Hemami, 1994).

2-5- Research on movement of granular particles into a ground engaging vessel

Very few authors have published complete work linking blasted fragments, relative movement and shape of ground engaging tools. These studies may be categorized into two groups; the analytical and experimental studies, and the discrete element modeling studies.

2-5-1- Analytical and experimental studies

In digging a rockpile using a ground engaging tool like a shovel dipper, Joseph and Shi (2012) noted that excavating depends on material properties such as particle size, shape, and size distribution, and the dipper rake angle that encourages the material into the dipper. When digging a rockpile through a shovel dipper, material softness or hardness plays an important role in the dipper performance (Joseph and Shi, 2012). In the case of a soft material that does not need a blasting, and usually consists of fine and same sized particles, the dipper trajectory is a long path parallel to the rockpile slope, and would be similar in different dig cycles. In such a case, fewer particles fall down towards the rockpile toe, as shown in Figure 2-23 (Joseph and Shi, 2012). In the case of a hard material that normally consists of blasted particles with wide size distributions, the material has more tendencies to fall down and accumulate at the rockpile toe. In such a case, the dipper trajectory has a length approximately equal to two to three times of the dipper depth, and the dipper role is to just clean the loose material at the rockpile toe, as shown in Figure 2-24 (Joseph and Shi, 2012).

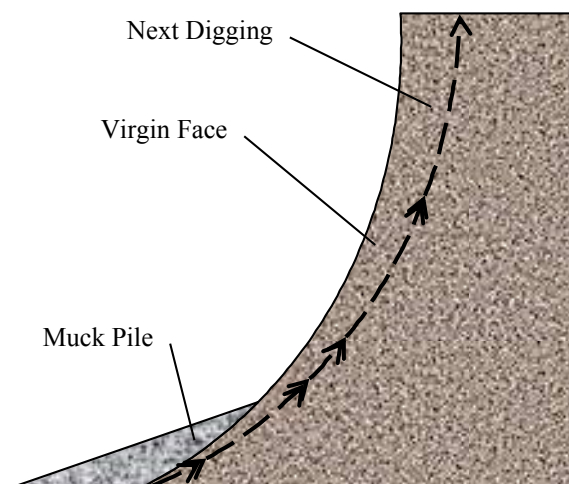


Figure 2-23 Unblasted soft material face (adapted after Joseph and Shi, 2012)

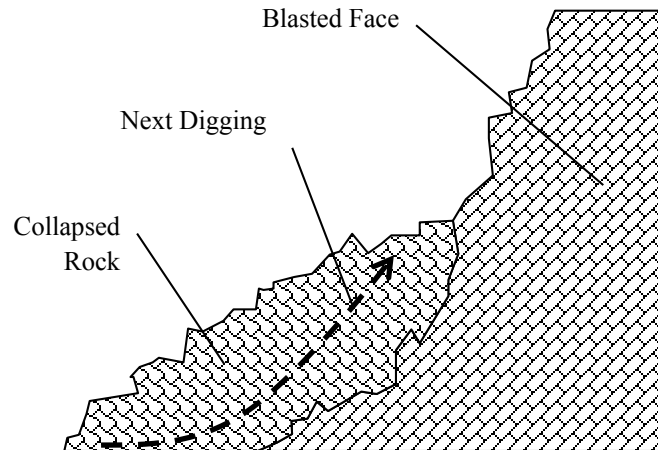


Figure 2-24 Blasted rock face (adapted after Joseph and Shi, 2012)

Rowlands (1991) described a theory that reflects the flow characteristics of material loading into a dragline dipper and named his model “Shear Zone Theory”. Figure 2-25 schematically illustrates Rowland’s theory. Based on this theory, by initiating a dig cycle and applying a drag force, the dipper approaches the virgin material and leads it to flow into the dipper, resulting in the generation of a zone named the “active dig zone” at the dipper lip and teeth (Rowlands, 1991). When the material flows into the dipper, it comes to rest by generating a layer named “initial laminar layer”. By continuing the dig cycle and increasing the size of the “laminar layer”, another zone named “active flow zone” is generated between the “active dig zone” and “initial laminar layer”. The particles in this zone have approximately vertical displacements (Rowlands, 1991). At the first dig phases, the virgin material flows into the dipper through “active dig zone”, while at latter dig phases, the virgin material transfers from the “active dig zone” to the “active flow zone”. By continuing the dig cycle, some material from “active flow zone” comes over “initial laminar layer”, and creates “dead load zone”. Also, a portion of this new zone is a result of failure of a part of the material from “initial laminar layer” (Rowlands, 1991). An increase in the drag angle results in increasing the speed of flowing material towards the rear of the dipper. Also, the increased drag angle may cause the combination of two zones of “active dig zone” and “active flow zone” (Rowlands, 1991). In addition, two shear planes are generated between these zones. The first one named “cutting shear line” is from the dipper tip to the free surface; the second one, named “dead load shear line”, is located between “initial laminar layer” and “dead load zone” (Rowlands, 1991).

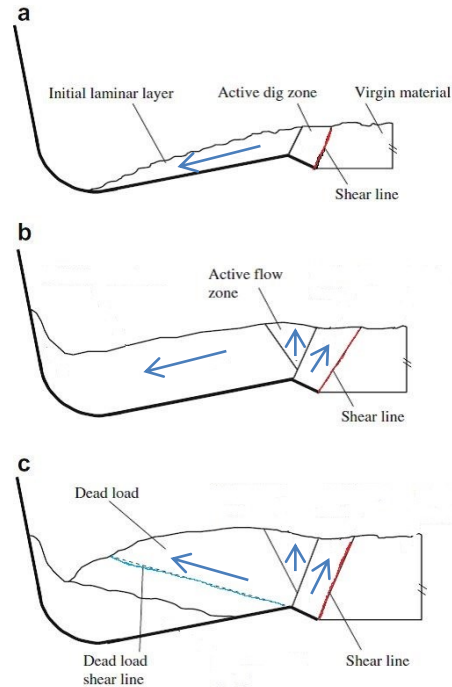


Figure 2-25 The Shear Zone Theory (adapted after Rowlands, 1991)

Rowlands (1991, 1992) also, experimentally investigated the filling behaviour of a scaled dragline dipper to study the effect of dipper shape, rigging conjunctions, and tooth spacing. He found that by modifying the width/depth ratio of a dipper it is possible to reduce the fill distance and improve the dig efficiency; however, reducing the fill distance has an inverse effect on the maximum drag force (Rowlands, 1991 & 1992). Also, he reported that specific dig energy (dig energy per unit volume of bucket payload) is a useful indicator for evaluating both the dipper efficiency and the material diggability (Rowlands, 1991 & 1992). According to Sing et al (2006-B), diggability refers to how much material resist against loading action, and is a function of the excavator type and size, and material properties such as hardness, density, size and size distribution. There are different methods to estimate the diggability of a material which is usually expressed as a dimension-less parameter (Sing et al, 2006-B).

The process of filling an excavator bucket without teeth was investigated experimentally by Maciejewski and Jarzebowski (2002). The aim of their research was optimization of the dig action through the geometry of the dipper and the dipper trajectories. They concluded that a tool with a long bottom wall that results in a lower rear wall pushing process is the most efficient shape of the

digging tool (Maciejewski et al., 2002). As reported by Maciejewski et al. (2004), when a ground engaging tool moves through a material, it causes a plane strain condition; however, in the case of excavating tools, a plane strain condition occurs only in limited areas, and therefore assuming such a condition for the entire area would be inappropriate. Maciejewski et al (2004) experimentally examined the accuracy of such an assumption (plane strain condition) for a soil mass in a test bin. He found that when the tool width is small, and so the tool is not in contact with the test bin side walls, the plan strain condition happens at the middle part of the tool (Figure 2-26). In the case of employing a number of teeth, if teeth spacing is high, the plane strain deformation will happen in front of each tooth, similar to the previous condition (Maciejewski et al., 2004). With the reduction of teeth spacing, the teeth will play as a single blade, and therefore the plane strain condition is again applicable for such a condition. However, this behaviour can only be assumed for a cohesive material and is not suitable for broken rocks (Maciejewski et al., 2004).

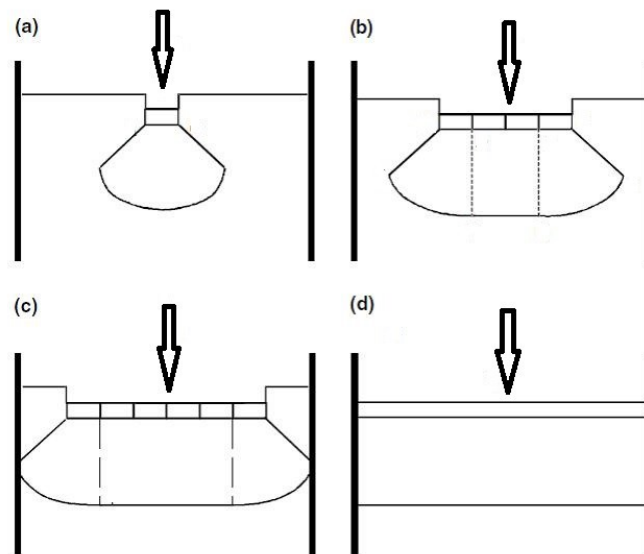


Figure 2-26 Top view of dumps for different widths (a)-(d) of a centrally situated tool (adapted after Maciejewski et al., 2004)

2-5-2- Discrete element methods (DEM) studies

The discrete element method (DEM) is an effective method to model the ground-excavator (tool) interactions, and can be used to solve some difficulties involved by the analytical methods (Coetzee et al., 2010). This method has been used to predict the behaviour of granular materials for the last decades, and has been provided the good results for many industrial and mining

problems, such as “dragline excavators”, “ball mills”, “silo filling”, and other industrial applications (Cleary, 2000).

Coetzee et al. (2007, 2009A&B, and 2010) modeled the flow of granular material into a dragline bucket, using DEM, and proposed a way to estimate the input parameters required for modeling cohesion-less materials. It was suggested that the size and density of granules could be assessed through direct measurement and modeled easily. Clumps could be used to model the shape of particles, and confined compression tests and angle of repose tests could be used to estimate the other parameters (Coetzee, 2010). Coetzee concluded that the general trend was modeled accurately, but DEM could not predict the drag forces correctly, Figure 2-27 (Coetzee et al., 2007, 2009A&B, and 2010).

Cleary (1998 A&B) modelled a dragline dipper filling, using DEM-2D to compare the performance of the different dippers, and to evaluate the effect of rigging and material properties. He also studied the effect of particle shape on fill times and volumes in 2D (Cleary, 2000), and noted two shape parameters that influence the behaviour of the loading particles into the dipper. They were aspect ratio and sharpness (Cleary, 2000). The filling of a dragline bucket was also modeled with spheres (Cleary, 2004) and with different super-quadrics shapes, both in DEM-3D (Cleary, 2009). Comparing the results indicated that the non-spherical particles showed more resistance to the flow, and resulted in a reduced payload and an increased fill time (Cleary, 2009). However, one weakness of these studies was that no experimental verification was provided to support the numerical results (Cleary, 2010). In another study, Owen et al. (2004) simulated a dragline bucket filling process which the particles were modeled with DEM-3D and the dipper was modeled with finite element method. Drag forces and drag distances were compared with a prototype scale test.

2-6- Influence of fragment properties on electric cable shovel performance

Electric cable (or rope) shovels are critical equipment in the surface mining industry. Parameters influencing the productivity and efficiency of mining shovels include material properties; such as particle size, shape, size distribution, and stiffness; affecting the excavation dig performance (Singh et al, 1992). The influence of material properties on the productivity and efficiency of mining shovels has been to date studied incompletely (Osanloo, 2005). Moreover, most studies

investigated the influence of particle size and size distribution for blasted materials, but only a few looked at the effect of fragment shape.

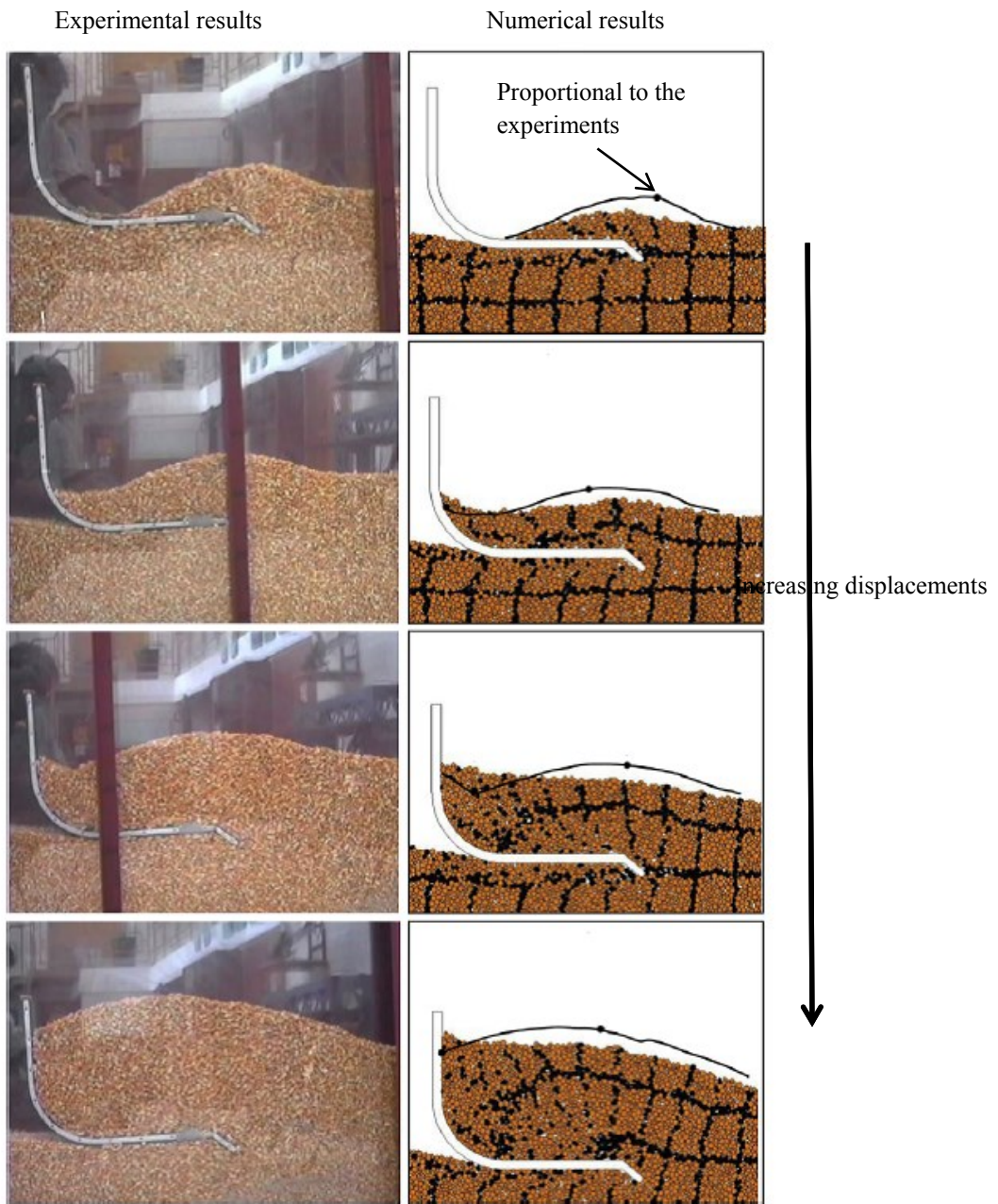


Figure 2-27 Dragline bucket filling results with rig angle=0 (adapted after Coetzee et al, 2009-A)

Williamson et al. (1983) performed one of the first shovel monitoring studies on the electric shovels to provide an index to estimate the material diggability at the Mt. Newman Iron Ore Mine in Australia. The index was based on the effect of size distribution, swell factor, and rockpile profile. Hendricks (1990), and Hendricks, Peck, and Scoble, (1990) introduced an effective

technique through the instrumentation and monitoring of the blast-hole drills and the electric mining shovels, at a surface coal mine in western Canada. Their proposed index could be used to characterize the medium, and to optimize the blasting results (Hendricks, 1990). Karpuz et al. (1992) studied the influence of cut depth, and blasting on the performance of the cable shovels during a set of experiments in a surface coal mine. Four different rock types with and without blasting, and three different cut depths were examined. The results indicated that an increase in the cut depth and the material strength provided an increase in the power consumption and the specific dig energy (Karpuz et al., 1992). A case study was performed by Taksuk (2000) to study the influence of several parameters, including particle size, fill factor, swell factor, specific dig energy, dig time, and loading period on the performance of machine. As a result of his tests, as the size of particles after blasting increased, the bucket fill factor decreased and the dig cycle increased. In addition to particle size, the formation properties and the operator skill were also found to affect the dig cycle (Taksuk, 2000).

Doktan (2001) studied the influence of blasting on shovel productivity and performance through an in-house developed simulator. He found that a better fragmentation results in increasing the number of the loading pass, decreasing the dig cycle, and increasing productivity, due to providing smaller sized particles (Doktan, 2001). In another study, Osanloo and Hekmat (2005) obtained a relationship between the shovel productivity and the rock properties, based on the modified Rosin-Rammler-Bennett fragmentation size expression, and an image analysis technique named GoldSize. Their investigation results indicated that as mean particle size and/or the percentage of oversized particles increase, the productivity of the machine decreases (Osanloo and Hekmat, 2005).

Some other studies have focused on the other types of excavators. For instance, Singh et al (1992) investigated the effect of size of blasted material on wheel loader productivity. They found that the bucket fill factor decreases with increasing the mean particle size, D_{80} , and the index of uniformity of particles. Also, they observed that the peak and mean penetration forces increase with an increase in the percent of oversized particles. In another study, Singh et al (2006-A) obtained similar results by examining the effect of size distribution of blasted material on the productivity of a wheel loader.

Based on these studies, it can be concluded that as particle size increases, void ratio increases, bucket fill factor decreases, and dig cycle increases (Singh et al., 1992; Taksuk, 2000; and Osanloo, 2005). Oversized particles tend to interlock more and show a higher resistance to the dipper penetration, resulting in increased dig time, decreased fill factor, and decreased productivity (Singh et al., 1992). In contrast, smaller particles lubricate the space between larger ones, resulting in an easier penetration, and so, a higher fill factor and a better productivity, but a longer dig time (Singh et al., 2006-A).

2-7- Key performance indicators for cable shovels

Many key indicators have been examined during previous studies, including dig cycle time, total cycle time, hoist energy and power, crowd energy and power, number of cycles per unit time, bucket fill factor, energy consumption for digging, and specific dig energy. The dig cycle alone is probably not a good indicator for ground diggability, because it varies significantly if the dipper works with non-uniform materials or follows non-uniform trajectories (Patnayak et al., 2005).

Williamson et al (1983) reported that crowd motor voltage and current react to digging conditions and used them as the shovel performance indicators. This reliance on these reactions is in contrast to the findings of Patnayak et al (2005) who reported that the crowd motor does not properly reflect the ground diggability, and varies not only in non-uniform materials but also in uniform materials (Patnayak et al., 2005).

Hendricks et al (1989) and Hendricks (1990) studied the relationship between shovel performance and rockpile characteristics, and found that the hoist motor responded well to the different digging conditions. They reported that, among the other indicators, the hoist armature current signal was the best indicator of ground diggability (Hendricks et al., 1989&1990). A field research program undertaken at a surface coal mine by Karpuz, et al. (1992) suggested that the best indicator of ground diggability is the specific dig energy that relates power consumption to payload and dig cycle (Karpuz, et al., 1992). Patnayak and Tannant (2005) used current and voltage data from hoist, crowd and swing motors of a number of the cable shovels for a performance monitoring study at an oil sand mine. They believed that average hoist power (hoist power/number of dig cycles) could be a representative indicator for the ground diggability, because it is independent on the dig

trajectory (Patnayak and Tannant, 2005). This indicator agrees with findings of Hendricks et al. (1989) and Hendricks (1990) in that hoist motor data responds well to different dig conditions.

It should be noted that taking an average of data results in losing detailed information and may not lead to accurate conclusions. Different parts of mine can have different digging conditions due to material properties, face properties, experience of an operator and etc. Therefore, taking the average of a parameter of a loading machine which works in different conditions is questionable. Instead, using a distribution of data would give a weighted average, while honoring the data detail, and avoid overestimating/underestimating in an assessment.

2-8- Size distribution assessment techniques

To have a better blasting result, it is required to have a fast and accurate way to evaluate the blasting, and to investigate its influence on the productivity process (Singh and Scoble, 1990). Blasting efficiency involves assessing the particle size after blasting. Different methods are available for this purpose that can be divided into two groups of direct and indirect methods (Siddiqui et al., 2009). The direct method that includes the sieve analysis is very accurate, but not fast and cheap. Therefore, indirect methods have been provided that can be categorized into three groups of the observational, empirical, and photo based methods (Siddiqui et al., 2009).

In the observational method, an experienced person inspects the rockpile right after the blasting, and evaluates the size of particles, the shape of the created rockpile, particle movements, etc. However, this method has some weaknesses; for instance, the observer cannot see the inside parts of the rockpile, and also his experience may influence the accuracy of the observation (Thote and Singh, 2003). There are a number of empirical methods for size distribution measurements; however, they all have some limitations, listed as follows (Thote and Singh, 2003):

- 1- The high number of unknown inputs may lead to a failure to consider all of them in size distribution analysis
- 2- The format of the analysis results may not be very practical.
- 3- Some constant parameters such as hole location, firing time, and explosive performance may influence the results.

Photographic techniques such as counting particles within superimposed grids have limitations, and the results do not cover the whole blasting (Palangio, 1995). Digital image analysing

techniques are new methods for the size distribution assessments, and use special hardware and software to estimate the particle properties such as size, shape, orientation, area, and perimeter (Bozic, 1998). The main advantage of such widely used methods is that they do not interrupt the production procedure, and therefore could be the best choice in mining operations (Siddiqui et al., 2009). Some other advantages are listed below (Maerz et al, 1996):

- 1- Image analysing techniques are fast with minimum time required to take and process a picture.
- 2- It is economically feasible to take as many samples as needed to minimize the sampling errors.
- 3- While sieving method is practical just for small scales, image analysing techniques can be used for any size of materials.

Like other techniques, this method has some limitations. For example, this method works better for non-colorful particles, narrow size distributions, or dusty fragments. In the case of a wide size distribution, the results would be less accurate for fine particles (Maerz, 1998). In addition, since in this method the long and intermediate particle dimensions are measured, the results may be overestimated in comparison to the sieving method that uses the intermediate and short particle dimensions (Maerz, 1998). Nowadays many software packages are available, using digital image analysing techniques, with different relative accuracies ranging from 2 % to 20 %, such as “SPLIT, WipFrag, GoldSize, FragScan, TUCIPS, CIAS, PowerSieve, IPACS, KTH, and WIEP” (Siddiqui et al., 2009). Here, the WipFrag software is reviewed as a useful tool for the size distribution analysis.

2-8-1- WipFrag Software

In the mid 1980's a research was performed by Du Pont company to find a more improved technique for particle size measurements, that resulted in proposing a new image analysing system, named “Waterloo Image Enhancement Program” (WIEP) developed by University of Waterloo (Palangio, 1995). Based on this system, WipFrag software was designed for the first time to evaluate quality of underground blasting, and become one of the common techniques in the digital image analysing systems for blasted materials (Frankline et al, 1995).

WipFrag can work with different types of images from different sources ranging from analog to digital cameras (Maerz et al, 1996). In this technique, at first, the edge of particles is detected automatically, manually, or a combination of both. Then, using geometric probability concepts, the size distribution of particles in 3D will be generated (Maerz et al, 1996). WipFrag has a number of capabilities to improve the results of the estimation of fine and large particles, such as “missing fines corrections”, and “merging” and “zoom-merging” techniques. Here, merging refers to the results combination of the different images with the same scale, and zoom-merging refers to the results combination of the different images with different scales (Maerz et al, 1996). It is worth mentioning that the first step in this technique involves obtaining a representative image of the broken rock. In this respect, there are a number of considerations (Frankline et al., 1995):

- At least five photographs at random locations of the material assembly should be taken to have a representative set of images of both fine and large particles, and then combine the results (Frankline et al., 1995).
- The field of view should be filled with particles, where the largest block should occupy less than 10% to 20% of the width of the image (Frankline et al., 1995).
- A set of images from a large rockpile requires the scale object to appear in only one of the images. But if the surface of the rockpile is not parallel to the surface of the camera, then at least two scale objects are required, one to place at the bottom of the rockpile, and one to place at the top of the rockpile (Maerz et al., 1996).
- Indirect or diffuse lights are recommended to avoid shadows and hot spots. In this way, particles are uniformly brightened, and have a soft shadow on their edges. In outdoor photography, it is better to avoid photography in sunny days (Frankline et al., 1995).

Chapter 3

Test preparation

The behaviour of fragmented material is influenced by the inherent characteristics of the material, characteristics such as particle shape, size, size distribution, angularity and surface roughness. These characteristics affect the productivity and efficiency of a loading machine like a mining shovel.

One of the objectives of this thesis was to model broken material flow into the dipper of a cable shovel experimentally, based on scaled experimental laboratory tests. The present chapter will discuss designing and setting up the scaled model for experimental analysis and several preliminary tests that were required before performing the experiment.

3-1- Cable shovel operation

According to Stavropoulou et al (2013), the main parts of a cable (rope) shovel are the lower works (consisting of the carbody of side rails), the upper structure (on which the mechanical and electrical drives are mounted), and the attachment which comprises the boom, the dipper, the crowd, and the handle (Figure 3-1). The main movements of a cable shovel may be classified into the following (Stavropoulou et al., 2013):

1. Crowd: lengthening and shortening the length of the crowd arm
2. Hoist: pulling the hoist rope to drag the dipper, handle, and crowd arm upward, and loosening the hoist rope to take the attachments downward by gravitational assistance.
3. Swing: turning the whole machine to right and left sides
4. Propel: traveling the whole machine from one place to another

Hoist and crowd related to the dig cycle, and swinging and propelling related solely to the movement of the machine. The hoist and crowd motors generate the hoist and crowd motions. The hoist motion is achieved via a rope drum lifting the dipper, while the crowd motion is accomplished by a rack and pinion arrangement between the crowd arm and the boom, respectively. During the crowd motion, the handle is extended out and the dipper moves towards

the active face. Effectively lengthening the handle and raising the hoist rope generate a dig cycle trajectory describing the dig kinematic (Stavropoulou et al., 2013).

Figure 3-2 shows the components of a typical shovel dipper (Shi, 2007):

1. “Teeth and lip system”
2. “Front wall, including wear protection rib and heel”
3. “Side wall”
4. “Back wall”
5. “Bottom door”
6. “Attachment and connection”

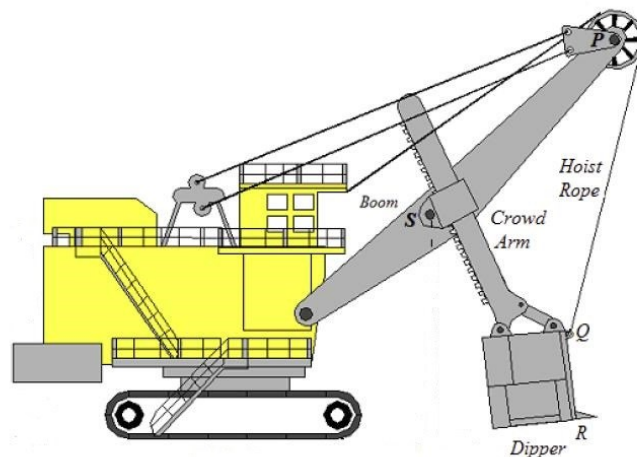


Figure 3-1Cable shovel nomenclature (adapted after Stavropoulou et al., 2013)

The dipper tooth and rake angles are two of the main factors in determining the filling factor as an expression of the efficiency of a dipper, plus the required power to complete a dig cycle. An imaginary line connecting the dipper lip to the rack pinion contact-with the dipper handle, describes the rake angle as an angle made with a horizontal line, Figure 3-3 (P& H, 2001). Rake angle is controlled by the length of pitch braces. The tooth angle is further adjusted based on the rake angle setup. In general, it is desirable to have the largest possible tooth angle to maximize the cutting action; together with proportionally minimal wear, resulting from a moderate heel band clearance. A steeper rake angle is more effective in easier digging conditions with less wear.

However, where the wear is severe, under heavier digging conditions, a smaller rake angle would be potentially more desirable (P& H, 2001).

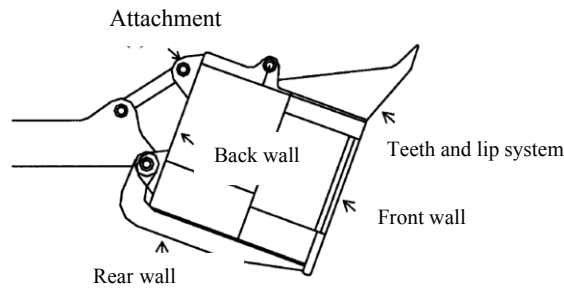


Figure 3-2 2D Illustration of typical cable shovel dipper (adapted after Shi, 2007)

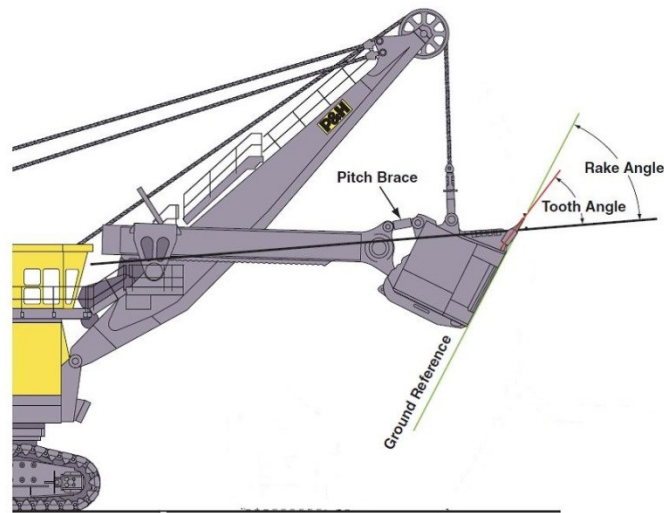


Figure 3-3 Schematic definition of rake angle, tooth angle and pitch angle (adapted after P& H, 2001)

3-2- Experimental setup

Based on the mentioned digging motions of the cable shovel, three-dimensional experiments were performed by moving a cable shovel dipper model in a test bin filled with crushed rock particles (Figure 3-4). The test bin had dimensions of $1\text{m} \times 1\text{m} \times 1\text{m}$ with one of the side walls made of transparent material to allow for visual observation and video recording (Figure 3-4, wall A). The test bin was filled with crushed limestone which was dumped from a very low height to create a scaled rockpile with a slope approximately equal to the angle of repose of the material. The final observed angle of repose was in the typical range of 37° to 40° for durable angular mine waste

rock reported by Hustrulid, et al. (2000). This angle of repose depends on the following (Hustrulid, et al., 2000):

- Shape properties such as size, shape and roughness (increasing with increasing size, angularity and roughness)
- Specific gravity of material (decreasing with decreasing specific gravity)
- Height of fall (increasing with decreasing height of fall)
- Water percentage (increasing with adding more water, decreasing after reaching to saturation)
- Curvature of the slope in plane (concave or convex slopes)
- Base conditions
- Natural or artificial slope (may decrease up to 6° in artificial slopes created in laboratory testings)



Figure 3-4 Three-dimensional test rig

A dipper handle with scaled dipper with transparent walls was fixed to the top frame of the bin (Figure 3-4). The dipper/handle assembly was hoisted at constant velocity by an electric motor equipped with a variable speed reducer. The motor model was a WPMDC 12-18-90V-56CB with a maximum speed of 1800 RPM which produced a maximum voltage of 90 volts. The model of the speed reducer was HDRF175-50/1-L56C which had a reducer ratio of 50.

The dipper hoist trajectory and the flow of material into the dipper were affected by the pitch at the lip, which caused the dipper to penetrate and dig into the material. As the dipper was hoisted through the material the resultant flow patterns were observed using a high resolution camera

which could be mounted above wall B of the bin (Figure 3-4) or on a tripod outside the bin. The hoist force was recorded using a load cell attached to the hoist rope, and an e-Daq data acquisition system (Figure 3-5 and Figure 3-6).



Figure 3-5 Experimental setup showing the position of the load cell

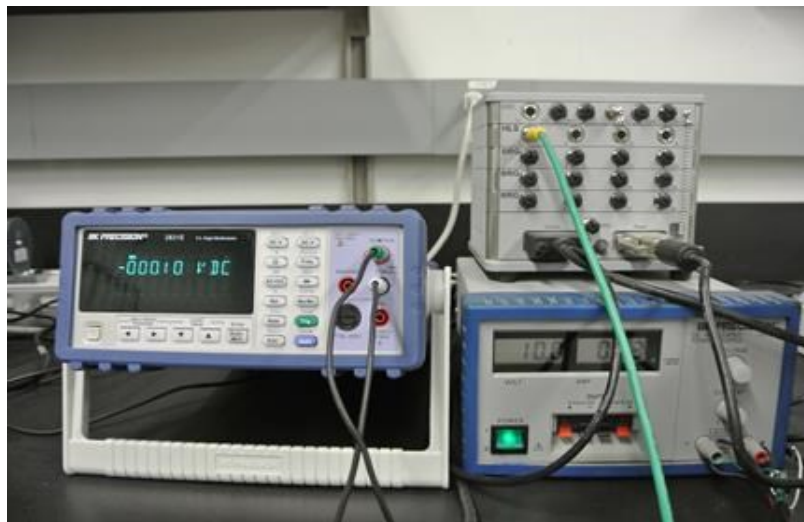


Figure 3-6 Data acquisition system

3-3- Material properties and scaling the dipper profile

The material used in this study was hard, angular, rough crushed limestone with inter-particle frictional and wear characteristics representative of common blasted rocks. Movement of these

particles could also be visually determined with relative ease which was critical for the current study.

3-3-1- Determining the size distribution of material

The chosen limestone had a mean particle size of 1 cm and a maximum particle size of about 3.75cm. Since very fine particles result in a dusty environment, and therefore an unclear scene, it was decided to remove particles less than 5 mm by sieving with a size 4 mesh (4.75 mm). To shorten the total processing time for size distribution assessment, the digital image processing system WipFrag was used to determine the size distribution of the remaining particles after sieving the material.

After sieving, the material was transferred into the bin in medium size buckets. Before filling, a few pictures were taken via putting each bucket under a tripod. The camera mounted on the tripod was set in a way that was perpendicular to the surface of the material. Zooming was used to improve photo resolution. However, to remove the effect of variable zooming, WipFrag's zoom-merge capability was used to combine images at different scales of magnification. Figure 3-7 shows the final result in estimating the size distribution of the crushed limestone.

The final particle size distribution was important in designing a dipper profile as it is generally assumed by shovel dipper designers that the material largest particle size should not be greater than one-third of the width of the dipper lip (Joseph, 2013, personal communication). Based on this, a simplified small scale dipper profile based on a 44 m³ shovel dipper (1:32 cube root scale) was designed with the lip length of 11 cm ($3.75 \times 3 = 11.25$). The bucket was not equipped with teeth to keep the experiments as simple as possible (Figure 3-8). An alternative solution was used to minimize the influence of lack of teeth in the performance of the dipper (section 6-2-1). Considering the scale factor of 32, the min and max size for upscale particles would be 0.32m and 1.2m, respectively which are in the range of blasted materials in open pit mines.

A second dipper was constructed to investigate the influence of dipper size on the particle flow pattern. This second dipper model was designed with a lip size of 17 cm. The results of the first dipper model were used to identify the particle flow mechanism and to study the probable influence of hoist speed and dig angle on the flow pattern, and also on the performance of the machine. The results of the secondary model were used to investigate the influence of dipper size on the flow

pattern and to ensure that the observed flow pattern was independent to the dipper capacity and/or dipper fill factor. The model also allows for the replacement of the employed dippers with different geometry designs.

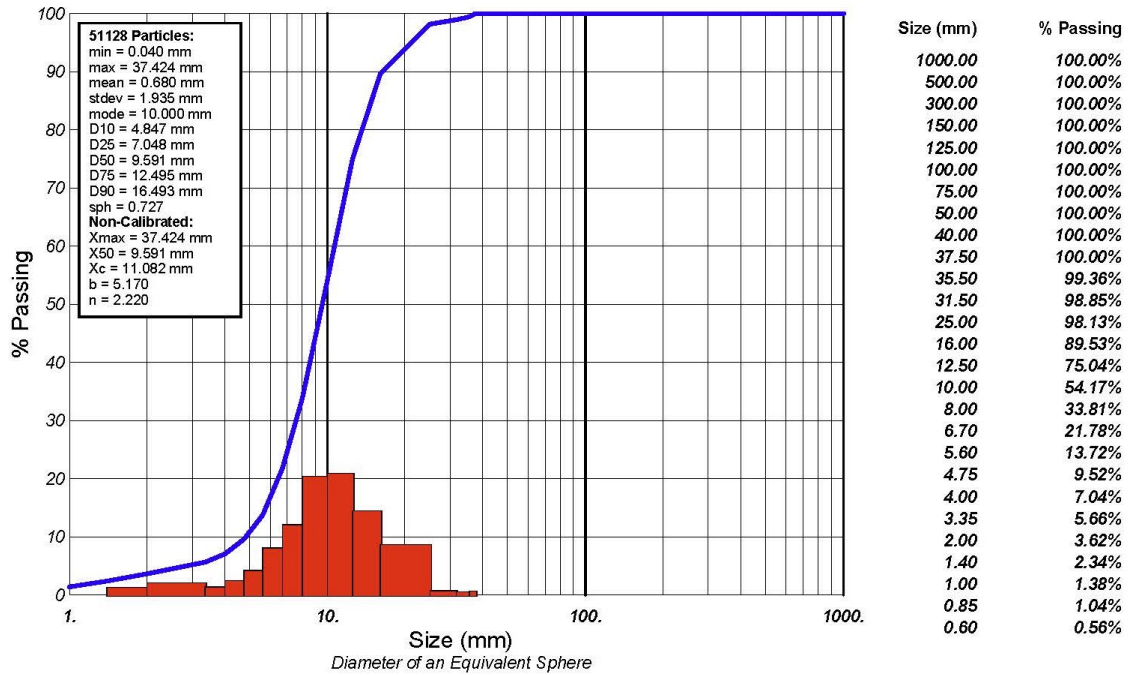


Figure 3-7 Size distribution of crushed limestone

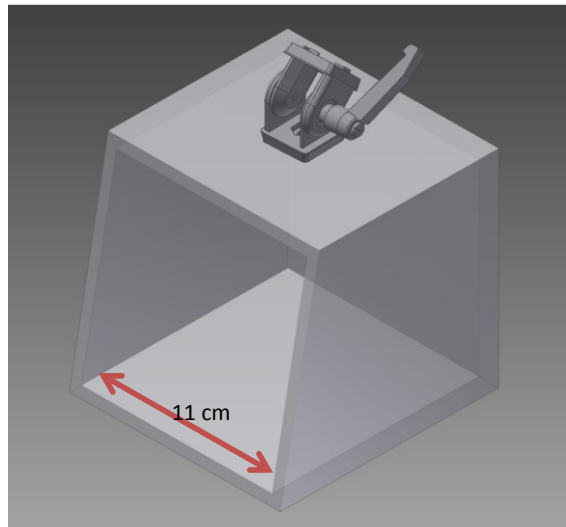


Figure 3-8 Scaled dipper

3-3-2- Determining material internal friction angle and cohesion

Shear strength is needed for determining the stability of a slope. In this research, internal friction angle is one of the requirements as an input for numerical modeling. Therefore, the direct shear test was used to estimate the shear strength of the material used in the experimental test (Figure 3-9).

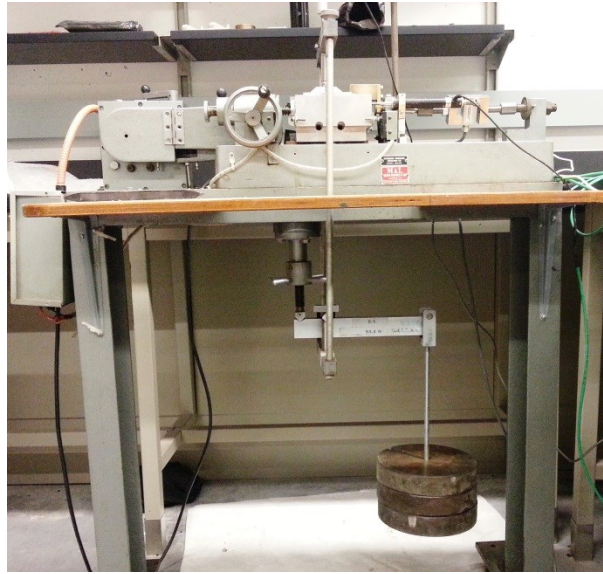


Figure 3-9 Direct shear test machine

The direct shear test was run several times for different normal stresses. The box had dimensions of 58mm × 58mm with a large enough height for testing the particles. For each normal stress, the shear stresses and the horizontal displacements were recorded, and plotted to find the maximum experienced shear stress during each test (Figure 3-10). Then, a plot was provided showing the examined normal stresses versus the estimated maximum shear stresses (Table 3-1 and Figure 3-11), and the best straight line was fitted to the data. From this line, the tangent of the internal friction angle and the cohesion of the material could be determined as equation [3-1].

$$\tau = \sigma_n \tan(\varphi) + c \quad [3- 1]$$

Since the material used in this study was dry broken particles, the value of cohesion was expected to be zero. So, the shear strength may be written as equation [3-2]:

$$\tau = \sigma_n \tan(\varphi) \quad [3- 2]$$

The results showed the examined material had an internal friction angle of 39.77 degrees with zero cohesion.

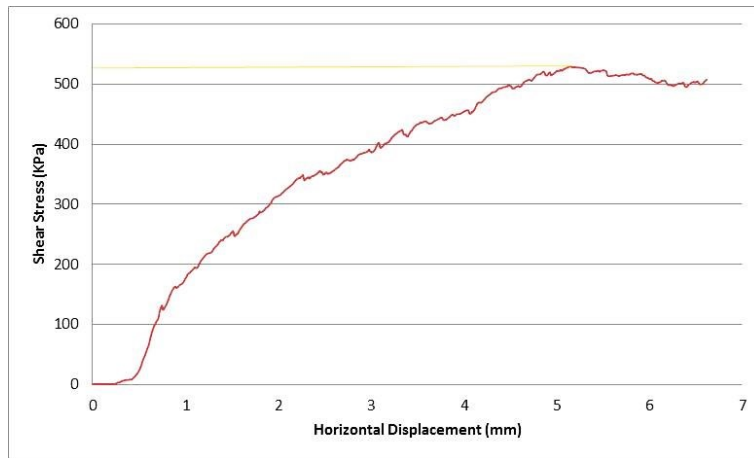


Figure 3-10 Plot of shear stress versus horizontal displacement for $\sigma_n = 630.89$ KPa

Table 3-1 Examined normal stresses and obtained shear strengths

Real Weight (lb)	Actual Normal Weight (lb)	Actual Normal Weight (Kg)	Actual Normal Pressure (KPa)	Measured Shear Pressure (KPa)
10	76.95	34.90	101.79	134.07
20	126.95	57.58	167.92	150.78
40	226.95	102.94	300.20	254.89
50	276.95	125.62	366.34	281.41
80	426.95	193.66	564.75	519.05
90	476.95	216.34	630.89	529.54

3-3-3- Determining particle loose density

The loose density of the material, using a volume/weight method, was estimated at 1415 kg/m³, obviously less than a solid rock density for limestone at about 2500-3000 kg/m³. This parameter was used for data analysing regarding to machine performance.

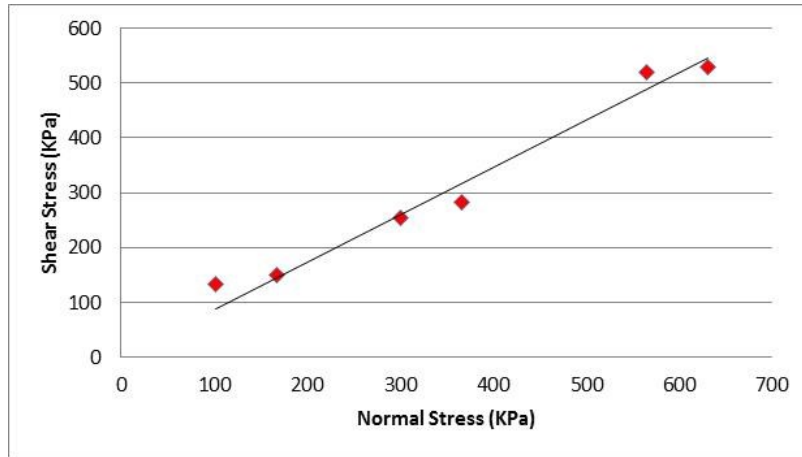


Figure 3-11 Plot of maximum shear stress versus the vertical confining stress

3-4- Conclusion

A test bin was prepared filled with angular crushed limestone with average size of 1 cm. Two cable shovel models of a 44m³ dipper were designed by considering the accepted law by shovel dipper designers that the material largest particle size should not be greater than one-third of the width of the dipper's lip (scales of 1:32 and 1:20).

To determine the size distribution of the material, the digital image processing system, WipFrag, was used. Direct shear test was used to find the shear strength of the material. Also, the loose density of the material was evaluated using a volume/weight method. These parameters were required for experimental set up, data analysing based on the experimental measurements and/or further numerical modeling.

Chapter 4

Broken particle flow mechanism into a cable shovel dipper

Since an improved understanding of dipper-ground interaction may lead to improve efficiency and productivity of heavy-duty excavators, this chapter will focus on development of a concept incorporating flow mechanisms for broken rock into cable shovel dippers.

The mechanism of granular material flow was investigated through a series of laboratory tests by moving 1:32 and 1:20 (cube root scale) models of a 44m³ dipper through a test bin filled with angular crushed limestone. The procedure of setting up the test was discussed in the previous chapter. The influence of several parameters including hoist speed, dipper pitch angle, and dipper size on the flow pattern were investigated qualitatively and quantitatively. Based on the results, a flow mechanism was presented.

4-1- Test procedure

The literature (P& H, 2001) recommended that an initial rake angle should be between 57° and 59° for hard digging conditions and between 59° and 61° for medium digging conditions. Based on material density, and characteristics such as uniformity of blasting, rake angle may be adjusted to provide an improved performance (P& H, 2001). Considering this recommendation, this study examined particle flow at rake angles of 60°, 70° and 80°. To simplify rake angle adjustment during testing the pitch angle was defined as the angle between the top wall of the dipper and the axis normal to the dipper handle, as shown in Figure 4-1. It should be noted that the top and bottom wall of the scale dippers are parallel and that a zero pitch angle condition implies a 90° rake angle. To achieve the desired rake angles testing was conducted with the dipper at pitch angles of 30°, 20°, and 10° respectively.

Previous studies have discerned optimal crowd and hoist speeds to be 0.25m/s and 0.7m/s respectively (Awuah-Offei & Frimpong; 2007 & 2011). For the purposes of this study the effect of crowd speed was neglected by fixing the dipper handle to a constant length. A review of field data from a 44m³ cable shovel operating in blasted hard rock showed that a hoist speed of 0.7m/s was very common. Given this agreement between the existing literature and field data a hoist speed

of 0.75m/s was chosen as the experimental mid-range hoist speed with 0.5m/s and 1m/s as the lower and upper ranges. During testing, these hoist speeds were scaled down to 0.016, 0.023, and 0.031m/s and were referred as low, moderate and high hoist speeds, respectively.

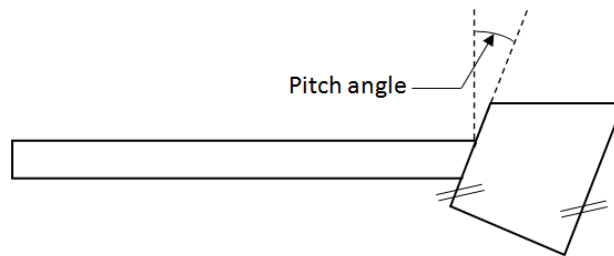


Figure 4-1 Pitch angle definition

To model the particle flow mechanism into the dipper, the dig cycles of the scaled model were recorded. To achieve a better understanding, two sets of measurements were performed for each test setup. In the first set, the camera was mounted on top of wall B of the bin to record the top view of the loading cycle. The findings of this set were used to investigate the particle flow mechanism into the dipper. In the second set, which will be explained in details in the next chapter, the camera was mounted on a tripod outside of the transparent wall to record the failure curvature of the rockpile at each instant.

Tests were run for the 3 different hoist speeds and 3 different dipper pitch angles with the main dipper model (smaller dipper) for a total of 9 (3×3) different digging conditions. Each test was comprised of 5 runs with results analyzed as distributions which were considered representative of the specific digging condition. The second model (bigger dipper) was tested at only one dig condition (lowest hoist speed and 30° pitch angle) with all other parameters held constant. The qualitative digging action was documented for each run.

The following procedure was employed for each run of the test:

1. Mount the camera on the top of the side wall of the bin.
2. Set the desired pitch angle and the desired motor speed.
3. Reshape the slope of the rockpile to have a constant slope and shape.
4. Check the length of handle, to be constant to all tests.
5. Turn on the hoist motor, turn on the data acquisition system to collect data, and turn on the camera to record the dig cycle.

6. When the dipper disengages from the rock pile, stop the motor, turn off the camera and data acquisition system.
7. Dump the dipper payload into a container and weigh the payload.
8. Repeat the cycle 5 times.
9. Adjust the dipper pitch angle and motor speed for another condition.
10. Repeat the test.

4-2- Particle flow observations

After performing the scaled tests, qualitative observations via camera records were used to define a model of broken particle flow into a dipper. Based on these observations a five step particle flow pattern was proposed to describe the flow of particles into the dipper as it moves from initial engagement to exit of the digging face. A description of each digging stage follows. Figure 4-2 illustrates a sample snapshot of different stages of particle flow observations (red arrows represent flow of particles into the dipper and blue arrows represent flow of material around the dipper).

Stage 1: In the first stage of the flow mechanism the dipper engages the rockpile. As the front lip of the dipper engages the material, particles above the lip are dislocated and a very thin layer of particles flows horizontally into the dipper. This initial flow of particles has rotational and sliding modes of motion, which push back towards the rear of the dipper ahead of the flowing material. This layer of particles which have rotational and sliding motion has been termed the “flow zone” (Figure 4-2, 1).

Stage 2: As the dipper penetrates further into the rockpile, more material is lifted by the dipper and a thicker “flow zone” of particles entering into the dipper is developed. These particles slide one over another and/or rotate into the dipper. At this stage, a flow of particles extends to the two sides of the dipper, adjacent to the toe of the rockpile. The penetration action of the dipper causes displacement of these particles, which in the initial stage of digging (near the toe) have rotational motion (Figure 4-2, 2).

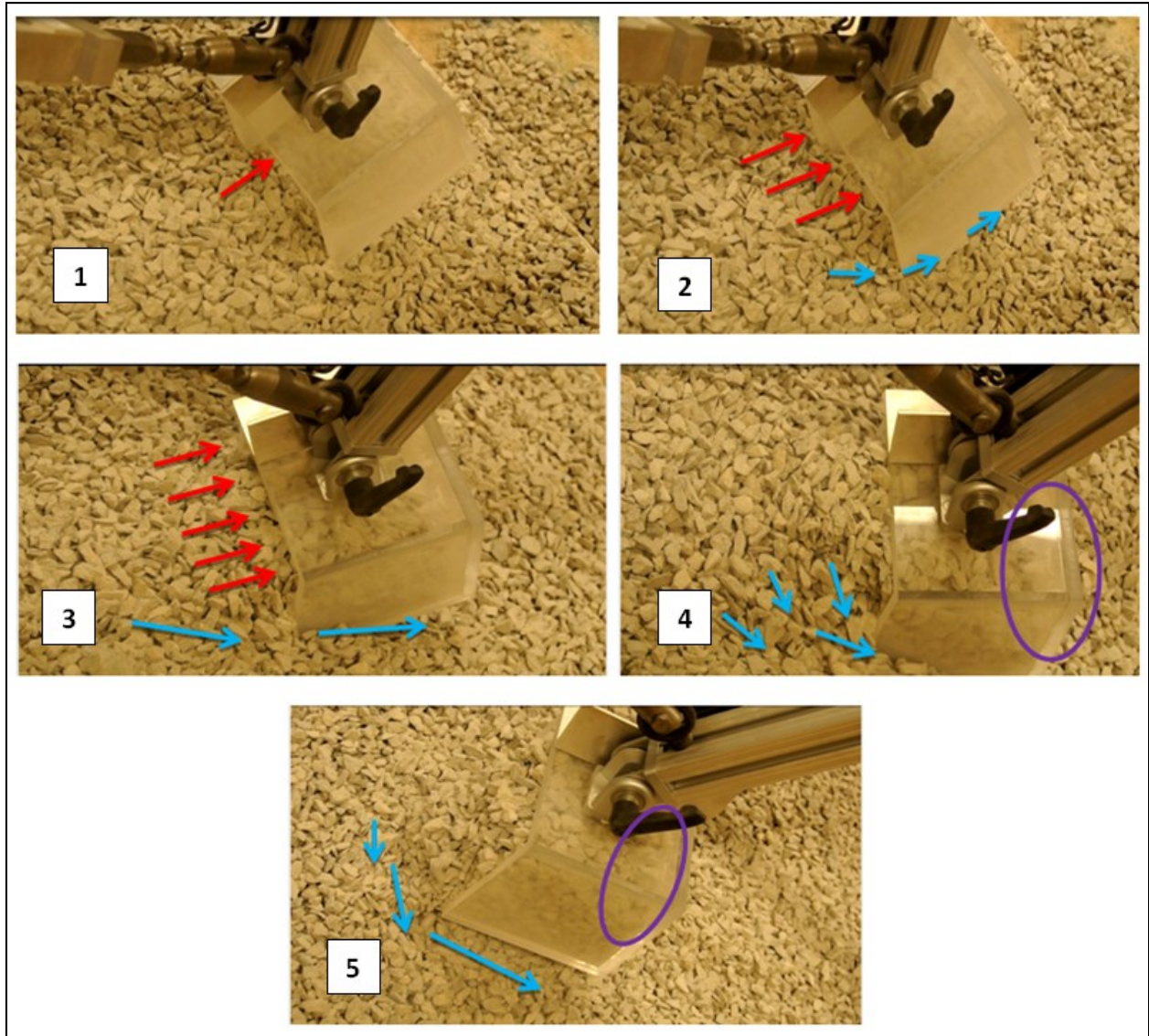


Figure 4-2 Snapshots of different steps of the particle flow into the dipper of scaled model

Stage 3: At steeper rake angles, more material is induced to flow into the dipper as well as to flow around two sides of the dipper. By increasing the thickness of the flowing material into the dipper, the particles which are in contact with the front wall of the dipper, interlock relative to each other and lose their mode of motion. These particles generate a new zone, named the “bulk zone” beneath the “flow zone” at the entry to the dipper. Movement of particles at this zone is more like movement of an interlocked bulk material. As the digging action continues, more particles from

the “flow zone” interlock the particles from the “bulk zone” which leads to an increasing thickness of the “bulk zone”, while the thickness of the “flow zone” remains approximately constant.

Inside the dipper, additional gravitational assistance makes the material flow move rapidly towards the rear of the dipper. However, particles in the “flow zone” keep their mode of motion until reaching the internal rear wall of the dipper (Figure 4-2, 3).

Stage 4: In continuing the dig cycle, a region of accumulated material just in front of the dipper’s lip was created and bulldozed upwards by the dipper, while a considerable space at the back corner of the dipper remains empty (Figure 4-3).

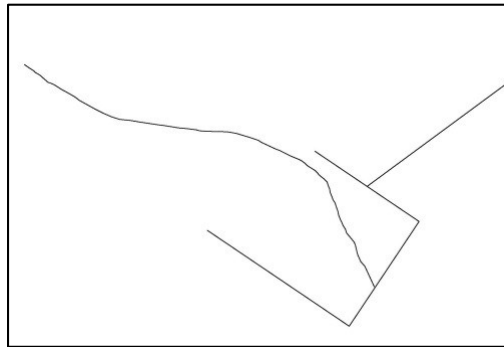


Figure 4-3 Creating and bulldozing material in front of the dipper

At this stage, depending on the dipper depth of cut, the thickness of the flowing material may reach to a maximum height (the height of dipper) and the entry of the dipper becomes blocked (situation that happened for the main model at the current study). In this state, the thickness of the “bulk zone” will remain constant while the thickness of the “flow zone” will be reduced due to a minimum rate of passing of material. By changing the orientation of the dipper, more material may then flow into the dipper with gravitational help (via rotational motion) and create greater opportunity for the dipper to accommodate more material (Figure 4-2, 4). Moreover, at this stage, the dipper may experience a maximum digging force which is due to the summation of the resistive forces beneath the dipper, the weight of material inside the dipper, and the resistance of material bulldozing ahead of the dipper. Also, the flow of material around the dipper is at its maximum rate and, due to the steeper slope of the rockpile, the mode of motion is more likely free fall rather than rotation, or a combination of both.

Stage 5: In the final stage of the digging, the contact between the material beneath the dipper and the underside of the dipper is decreased, and the dipper begins to detach from the slope. Moreover, as the dipper disconnects from the slope, not only will bulldozed particles fall down, but also excess particles will fall out of the dipper. Meanwhile, by changing the orientation of the dipper a very thin layer of “flow zone” may be created which directs more particles towards the rear of the dipper to fill the empty space at the rear (Figure 4-2, 5). However, even at the time of disengaging the dipper from the rockpile, the empty space may still be seen at the top of the inside of the rear dipper, between the front wall and the rear wall (door). This phenomenon is not known to be observed previously in dipper development.

Previous researches have indicated that a curved front dipper with original back creates a void space at the top of the back wall, and that this void is generated at the end of the dig cycle (Figure 4-4). Shi (2007) attributed this void to the tendency of cut material to flow and create a cap of material at the end of a dig cycle on top of the material excavated into the dipper during the dig cycle.

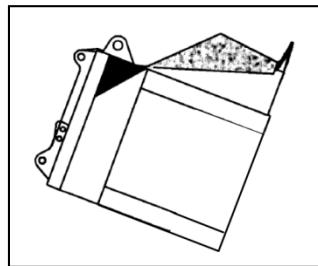


Figure 4-4 Traditional design of shovel dipper with void space at top area of the back wall (Adapted after Shi, 2007)

An outstanding finding of this study was to identify the procedure of creating such a void space inside the dipper. One of the advantages of using transparent walls dipper was to show how this void space may be generated. Observations of the dig cycle made through the dippers transparent wall indicated that, in contrast to previous beliefs, the void space is actually generated during the dig cycle and that its initial location is between the bottom door and back wall. At the end of the dig cycle the void space transitions to its final location as the changing orientation of the dipper causes a portion of the particles from the “flow zone” to drop towards the rear of the dipper, shifting the void space from the bottom to the top side of the back wall (Figure 4-5). Based on the

work of Shi (2007), replacing the common back wall with a skewed one will help reduce the volume of this void space, this is still believed to be valid.

Another consideration is the angle that the flowing material inside the dipper makes with the dipper front wall (the base of the dipper). This angle which was named “dynamic angle” by Hadjigeorgiou (1993) is related to the material properties, particularly the angle of internal friction. Based on the observations, after reaching to the rear of the dipper, this angle will reduce. However, the initial magnitude of this angle depends on the angularity of fragments. More angular material tends to create a steeper “dynamic angle”. According to Hadjigeorgiou (1993) as the internal friction angle increases the maximum value of “dynamic angle” increases which results in a decreased dipper productivity.

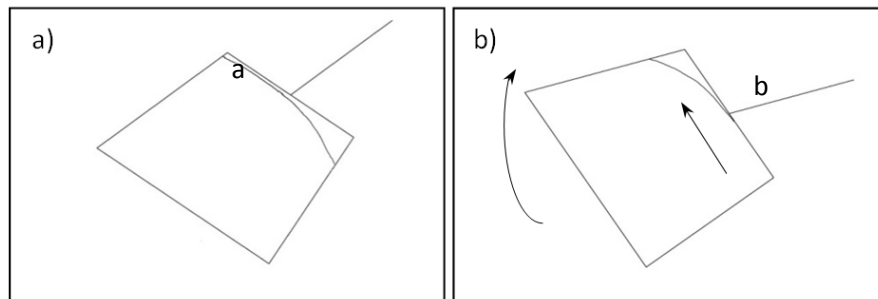


Figure 4-5 Moving the location of the void space from the bottom side (a) to the top side (b) of the back wall by changing the orientation of the dipper

4-3- Influence of pitch angle on the particle flow mechanism

Quantitative comparisons of material flow are difficult due to complex flow patterns; however, some qualitative observations and inferences can be made. Qualitatively, the results showed that the dipper angle had no influence on the general flow pattern, but pitch angle did affect the shape of the flowing material and bulk zones, and therefore the fill factor. When the dipper engages the face, the front wall of the dipper is at an angle to the slope of the rockpile (Figure 4-6). This angle is inversely proportional to the pitch angle (Figure 4-6, a and c). When flowing material reached the ingress of the dipper, it accumulated at the dipper entrance. At larger pitch angles, the volume of flowing material had greater height but shorter length (in relation to the face of the rockpile); in contrast, at lower pitch angles, flowing material had a shorter height. A narrower flowing layer resulted in a greater chance for particles to flow into the dipper before the ingress of the dipper

becomes blocked. This greater probability for particles to flow into a dipper led to a higher fill factor and less void space generated at the rear of the dipper.

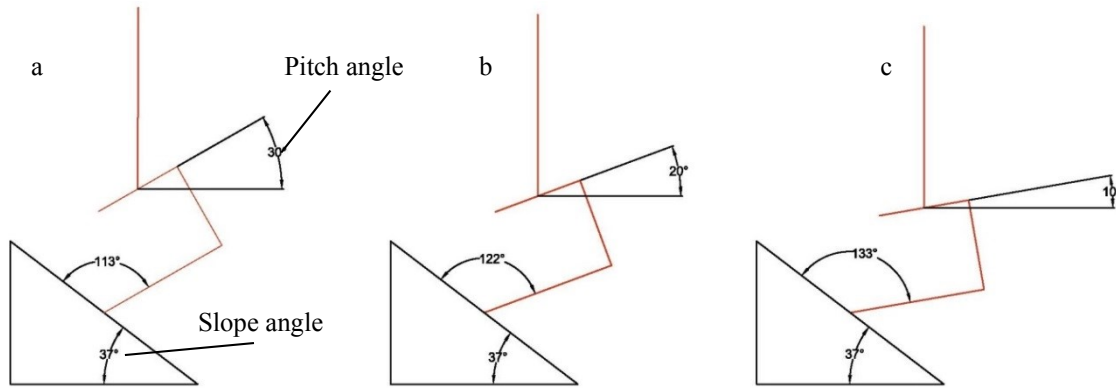


Figure 4-6 Angle between the dipper and rockpile with slope angle of 37° at the time of engaging at examined pitch angle

Review of the recorded dig cycles at each hoist speed showed that as the fragmented particles reached the back wall of the dipper, with a pitch angle of 30°, the thickness of the flowing layer at the entry of the dipper is nearly equal to the height of the dipper (Figure 4-7, a). At a pitch angle of 10°, the thickness of the layer at entry of the dipper is about half the height of the dipper (Figure 4-7, c) and, a pitch angle of 20° generated a flow layer with thickness between 50% and 100% of the dipper height (Figure 4-7, b). At each of the three hoist speeds, the thickness of material inside the dipper, and the size of the void space at the rear of the dipper were affected by different pitch angles (Figure 4-8 and Figure 4-9). From these observations it can be concluded that for constant hoist speed and digging conditions the pitch angle influences the amount of flowing material entering the dipper while having no significant change on the flow pattern of granular particles. Quantitative investigations regarding to the influence of pitch angle on the performance of the machine will be discussed later.

4-4- Influence of hoist speed on the particle flow mechanism

Qualitative comparisons of the flow pattern of granular material into the dipper profile showed that hoist speed variation within examined range have no significant influence on the flow mechanism of particles into the dipper. Quantitative investigations into the influence of hoist speed on the performance of machine will also be discussed later on.

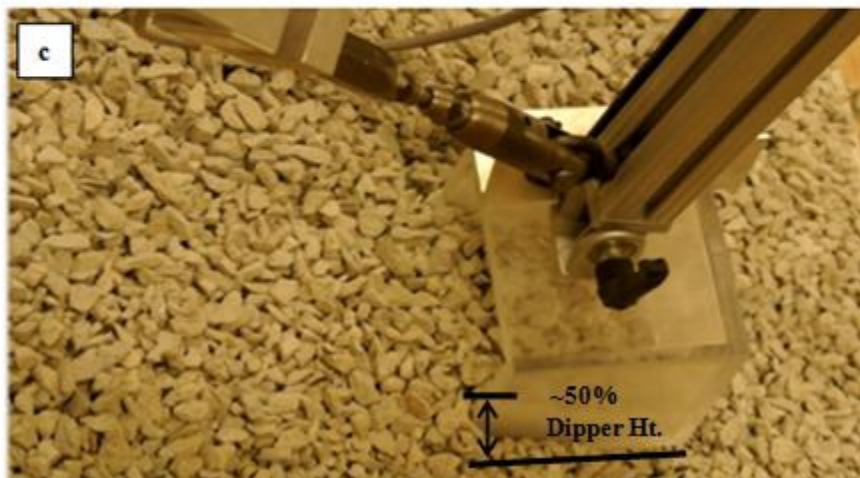


Figure 4-7 Low hoist speed, a) pitch angle 30°, b) pitch angle 20° and c) pitch angle 10° -the moment material reaches to the rear of the dipper



Figure 4-8 Moderate hoist speed, a) pitch angle 30°, b) pitch angle 20° and c) pitch angle 10° -the moment material reaches to the rear of the dipper



Figure 4-9 High hoist speed, a) pitch angle 30°, b) pitch angle 20° and c) pitch angle 10° -the moment material reaches to the rear of the dipper

4-5- Influence of dipper size on the particle flow mechanism

To investigate the influence of dipper size on flow patterns, a second set of tests were performed using a larger secondary dipper model, which had been constructed with a 17cm lip length as opposed to the 11cm lip length of the first dipper. This second dipper was tested at the low hoist speed, 30° pitch angle dig condition with all other parameters held constant.

Review of the recorded dig cycles indicated that the flow pattern with the larger dipper matched the different stages observed with the smaller dipper model. Per Figure 4-3, it was anticipated that a larger bucket would generate less accumulated and bulldozed material than a smaller dipper. However, the study showed the height of the bulldozed region generated from any dipper was nearly equivalent. The size (height) of the accumulated region in front of the dipper was interpreted as being more dependent on the depth of cut rather than the size of the dipper. Where a shallower depth of cut resulted in less likelihood of blockage at the dipper entry, resulting in more material loading into the dipper, but a lower fill factor was realized at the end of dig cycle. In contrast, a deeper depth of cut led to a higher fill factor but higher probability of blockage at the entry which caused the machine to consume non-productive energy in the form of greater bulldozed material per unit material loaded into the dipper. Thus, based on the visual observations, it can be concluded that the size of the dipper had no influence on the particle flow mechanism.

However, it was observed that at the end of a dig cycle, although the bigger dipper had a higher amount of payload due to a wider lip length, it showed a lower fill factor in comparison to the smaller dipper. The only reason for such a result was employing the same depth of penetration for both dippers. The present investigations indicated that there might be a relationship between the dipper capacity and the optimum applied depth of penetration. Employing the same depth of cut for one dipper might result in a high fill factor while for another dipper with different capacity might end up with a very low or a very deep depth of penetration, and therefore inappropriate efficiency. Further investigations should be conducted with the goal of identifying an optimal cut depth at a given dipper width with respect to energy consumption.

4-6- Influence of dig speed and pitch angle on performance of modeled cable shovel dipper

Several key performance indicators were used to determine the influence of hoist speed and pitch angle on the first (smaller) dipper model performance. These indicators included dig time, achieved payload, hoist force, dig speed, dig trajectory, dig energy, specific dig energy and energy consumption rate. These metrics were calculated using the recorded hoist force, dig speed, measured payload per dig cycle and dig time which was obtained from the video recorded of each dig cycle. The following section discusses the effect of hoist speed and pitch angle on these metrics.

Figure 4-10 illustrates an example of the hoist force recorded during a single dig cycle at a frequency of 100Hz. Attention is brought to the fact that it is possible to estimate the location of five stages of the proposed flowing theory on the recorded graph as the following:

- I. Engaging the dipper to the rockpile. The small value just before beginning the dig action is related to the dipper weight,
- II. Beginning of the loading cycle which shows a sharp increase in the dig force,
- III. Steeper rake angles result in deeper penetrations and therefore greater dig forces (it is difficult to accurately separate phases II and III in the graph, however increasing the dig force due to the increasing the depth of penetration and increasing the thickness of the flowing material into the dipper is obvious),
- IV. Experiencing maximum dig forces which is due to the summation of the resistive forces beneath the dipper, the weight of material inside the dipper, and the weight of material bulldozing ahead of the dipper
- V. Detaching the dipper from the rockpile which results in a decreased dig force. The final recorded forces after exiting the dipper reflects the weight of the dipper and the loaded material.

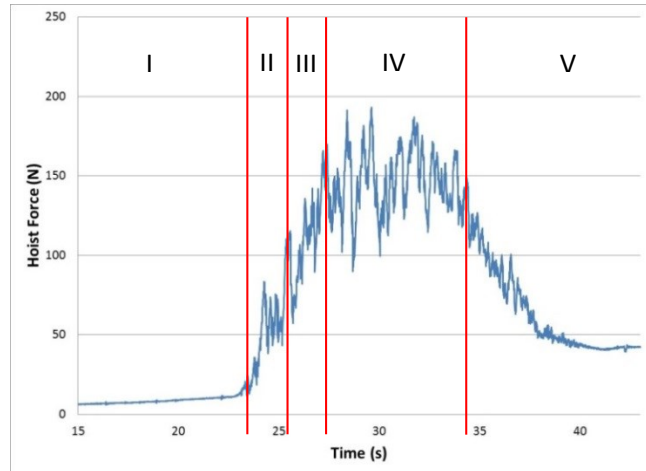


Figure 4-10 An example plot of hoist force vs time resulted from the data acquisition system

The effect of dipper lip velocity on the lip draft force has been investigated by a number of researchers; a comparison of these studies by Coetzee (2004) concluded that the velocity affects ground-engaging tools at high magnitudes (> 1 km/h), and at such magnitude, has a less significant impact on non-cohesive materials, such as broken limestone (Awuah-Offei, 2011). This agrees with the results of Frimpong et al. (2004) who observed that the shovel performance may be influenced by the material surface friction angle and/or the dipper trajectory, while dipper velocity does not have any predictable influence on it.

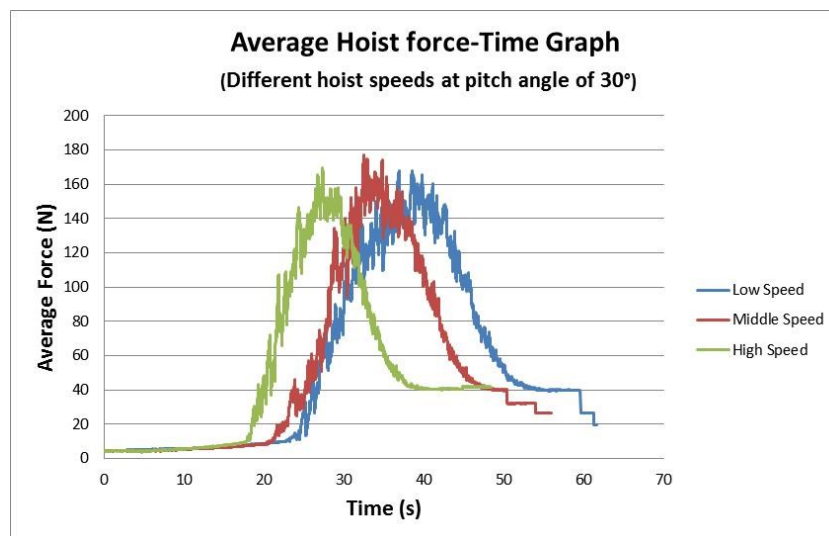


Figure 4-11 Hoist force values with different hoist speeds at pitch angle of 30°

Figure 4-11 shows the average recorded hoist force for low, medium and high hoist speed at a 30° pitch angle. The results shown in this figure agree with previous studies in suggesting that hoist speed does not affect hoist force.

Figure 4-12 shows the average cycle time for all dig conditions with the minimum and maximum ranges. It is apparent that by increasing the dig speed, the dig time decreases. Also, the figure shows that the pitch angle has little to no influence on dig time.

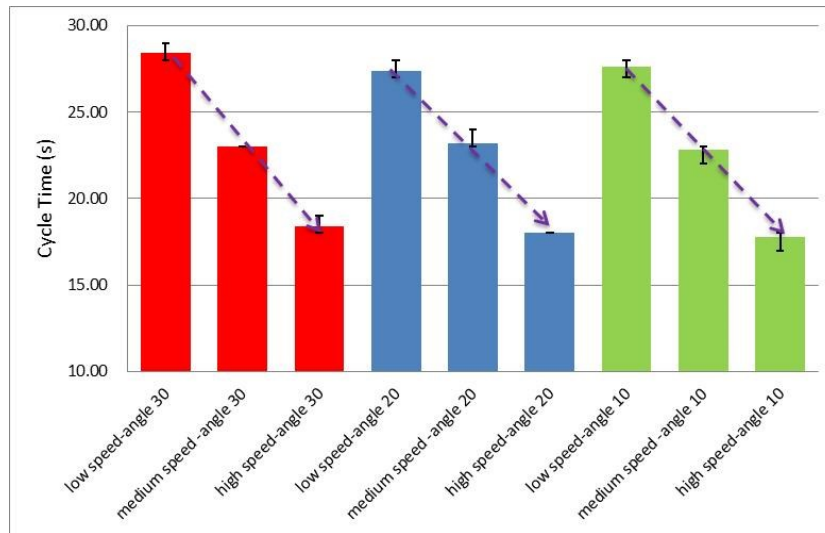


Figure 4-12 Cycle time range

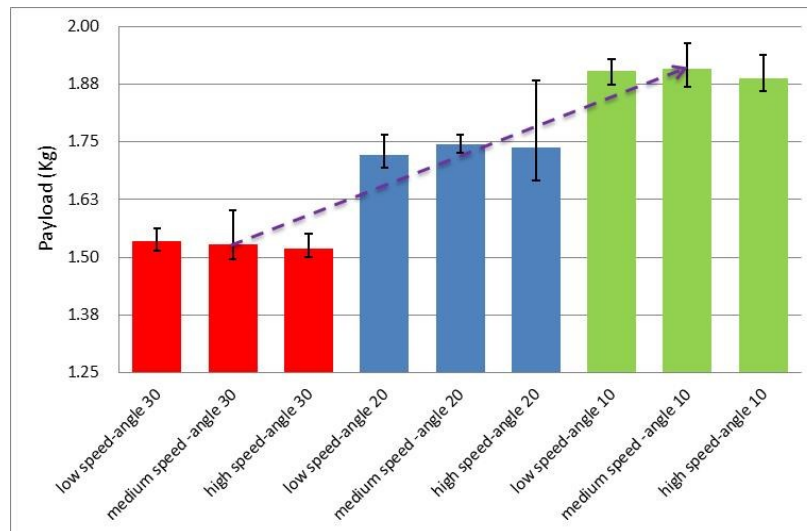


Figure 4-13 Payload range for different conditions

The payloads obtained from each test are illustrated in Figure 4-13. It was found that pitch angle had a substantial influence on dipper payload with a low pitch angle resulting in a higher average payload. In contrast, varying dig speeds had little impact on loading action except under the high hoist speed and 20° pitch angle dig condition which yielded higher variability in payload.

Figure 4-14 to Figure 4-16 illustrate dig energy, rate of consuming energy and specific dig energy, respectively, for different dig conditions. Comparing the dig energy under the tested conditions (Figure 4-14) showed there was no distinct trend corresponding to dig energy. Dig energy is a function of dig force and dig trajectory, but it does not consider other parameters, such as payload or cycle time which, are directly related to pitch angle and dig speed, respectively (Appendix A). Given this, dig energy may not solely be used as a performance indicator for comparing the efficiency of different dig conditions. To make an efficiency comparison, two other indicators were used which better relate power consumption to digging characteristics. First, the rate of consumed energy, calculated as the required energy to excavate 1 m³ of material per second, which depends on energy, dig time, and amount of excavated material (payload). Second, the specific dig energy is dependent on power consumption, dig time and payload. The results of these indicators highlighted the significant influence of dig speed and pitch angle in the performance of the shovel system.

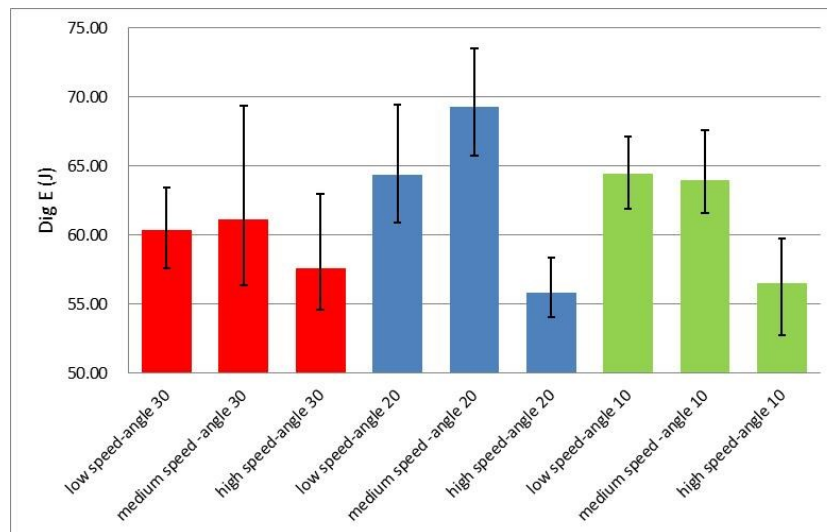


Figure 4-14 Dig energy

As shown in Figure 4-15, an increase in dig speed for a fixed pitch angle increases the rate of energy consumption and, at constant speed, lower pitch angles result in a lower rate of energy consumption which can be attributed to the larger payload at lower pitch angles. Figure 4-16 shows that at a constant pitch angle, the energy (consumed) per unit volume of material excavated decreases with increasing dig speed. This implies that, for a typical shift, although a higher dig speed will result in a higher rate of energy consumption at the end of the shift the shovel will have completed more cycles and moved more payloads. Given this interpretation it may be concluded that employing a lower dipper pitch angle and faster hoist speed results in a greater productivity and higher efficiency.

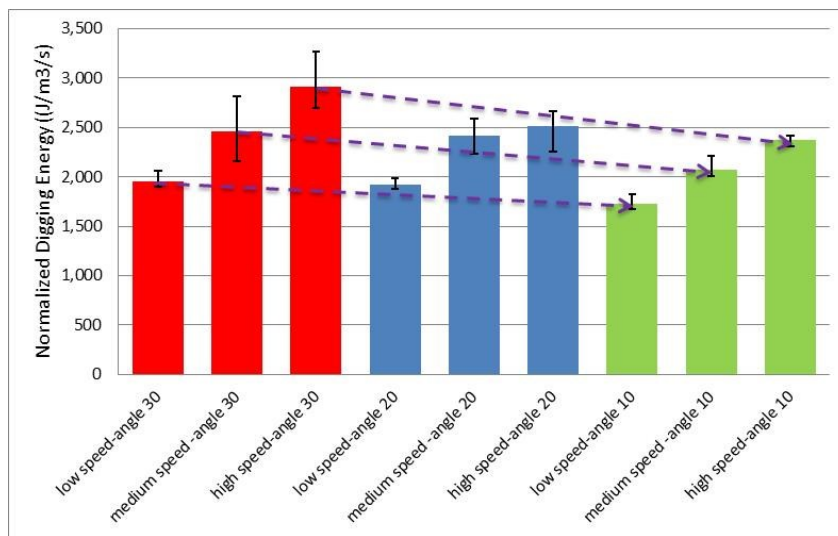


Figure 4-15 Average rate of consuming energy

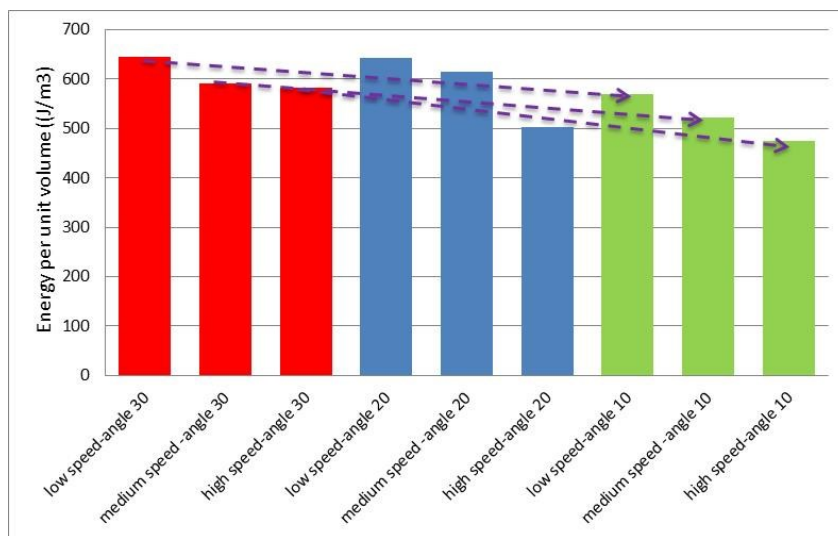


Figure 4-16 Specific dig energy

4-7- Particle flow mechanism

As the lip of the dipper contacts the rockpile, particles above this level are displaced and flow into the dipper as a thin layer with rotational and sliding modes of motion (flow zone).

As the dipper penetrates further into the rockpile, more material is lifted by the dipper and developed a thicker layer of flowing particles. The lifted particles collapse and fall into the dipper. The particles which are in contact with or close to the front wall of the dipper lose their modes of motion due to interlocking to each other and create another layer of flowing material (bulk zone). Particles in the “flow zone” keep their modes of motion until reaching the internal rear wall of the dipper. By increasing the thickness of the layer of flowing material into the dipper, more particles lose their mode of motion and transfer into the “bulk zone”.

In continuing the dig cycle, in addition to the small pile of material inside the dipper, a wedge of material is created in front of the dipper which is pushed upward by further advancing the dipper. The piles inside and outside the bucket are closely linked and grow together. In non-shallow runs, the entry of the dipper may be blocked via this wedge of material, prevents further particles from entering into the dipper. By changing the orientation of the dipper, more material may then flow into the dipper with gravitational help (via rotational motion) and create a greater opportunity for the dipper to accommodate more material.

During the dig cycle, a void space is generated inside the dipper which is surrounded by the material pile and the rear and back walls of the dipper. By increasing the thickness of the flowing material inside the dipper the size of this void space reduces.

Furthermore, there is another flow of material at the two sides of the dipper, which is created in the initial stages of a dig cycle via deeper penetration of the dipper and exists up to the end of the cycle. The penetration action of the dipper causes this material to fall towards the toe of the rockpile with rotational and free fall modes of motion.

At the end of the dig cycle, the dipper detached from the rockpile and will let excess particles fall out of the dipper. By changing the orientation of the dipper at the end stage, the empty space transfers from the bottom to the top side of the back wall.

Figure 4-17 summarizes the different stages of particle flow mechanism, and the void space generation inside the dipper.

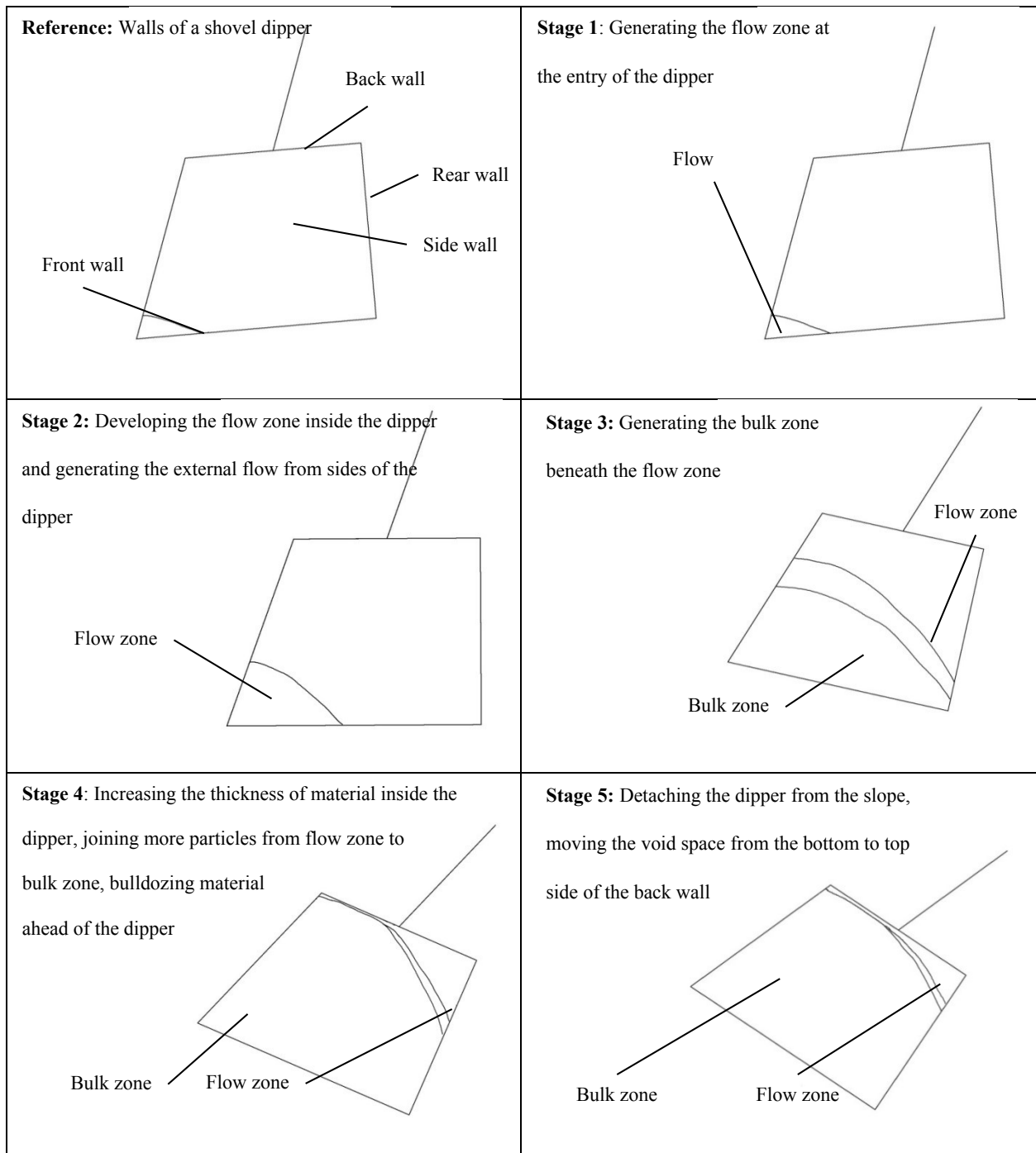


Figure 4-17 Diagram of different steps of the particle flow into the dipper of a cable shovel

Although the general flow pattern is anticipated to be independent on the dig condition and material properties, it may be influenced by them.

In digging a crushed cohesion-less angular material which is considered as a heavy digging condition, particles resist to flow into the dipper. This will result in generating small piles inside and in front of the dipper. The initial slope of these piles is dependent on the material internal friction angle and therefore particles angularity (Hadjigeorgiou, 1993). It is believed that the maximum value of this slope before it fails is equal to the angle of repose of material. When particles pass this maximum value, they collapse and flow towards the rear of the dipper (Hadjigeorgiou, 1993). Rougher and more angular particles have a higher friction coefficient and show more resistance against flowing. This results in a steeper pile of material at the dipper's ingress, and therefore, more probability of entry blockage while the rear of the dipper has a considerable void space. In this case, the empty space usually remains at its initial location even if the dipper ingress gets blocked with the material in front of the dipper.

The dipper rake angle has an undeniable influence on the dipper fill factor and the energy consumed during a dig cycle; therefore, employing an improved rack angle would significantly increase the efficiency and productivity of cable shovels (P&H, 2001). Increasing the rake angle or decreasing the pitch angle flattens the approach of the dipper's lip, which results in a smoother flow of material into the dipper and less probability of entry blockage of the dipper. This will increase dipper's fill factor and reduce rate of energy consumption and specific dig energy, which means lower power consumption and higher machine productivity.

The speed of digging has no influence on the flow mechanism, however it directly affects the cycle time. Higher hoist speed results in a shorter dig time but a higher rate of consuming energy. However, in a specific period of time such as a typical shift, the shovel will have completed more cycles and moved more material which means greater productivity.

The slope and shape of material piles inside and in front of the dipper are the functions of material properties and independent on the dipper size. Employing a bigger dipper in comparison to the particle sizes reduces the likelihood of the dipper's entry blockage under the same depth of cut. However, it will end up with a lower fill factor and productivity.

It should be noted that this is a generalised interpretation and it is anticipated that there may be variations resulting from different materials and digging conditions. Further studies are recommended regarding to investigate the influence of other factors such as dipper shape, and material properties (size distribution, density, etc.)

4-8- Conclusion

The primary objective of this chapter was to investigate the flow mechanism of cohesion-less granular material entering the dipper of a cable shovel. A set of experimental tests were performed to simulate dig conditions by varying the dipper size, dipper pitch angle and hoist speed. From test observations, it has been proposed that the flow behaviour of material during a dig cycle may be described relative to the dipper. It was found that, in contrast to previous beliefs (Shi, 2007), the typically observed void space inside the dipper is generated during the dig cycle and that its initial location is between the bottom door and front wall. This void space changes location during the latter stages of the dig cycle as the orientation of the dipper changes resulting in the void space moving from the front wall to the dipper's back wall.

Qualitatively; the tests revealed that the flow pattern is independent of digging conditions. However; the thickness of the flowing layers, and therefore, the amount of material loading into a dipper is influenced by the dipper's pitch angle and dipper's depth of cut. Lower pitch angles resulted in a narrower flowing layer which leads to a higher amount of payload and less dead empty space at the rear of the dipper. An optimum depth of cut reduces the likelihood of blockages at the dipper entry resulting in a continuous loading procedure with a higher bucket fill factor and lower energy consumption.

Quantitatively, an efficiency comparison was performed between the different dig conditions using several key performance indicators including; cycle time, payload, dig energy and specific dig energy. These comparisons showed that a lower pitch angle and a faster hoist speed resulted in a lower specific dig energy due to a larger payload moved per unit of time.

Chapter 5

Failure curvatures developed by digging

The dipper trajectory is controlled by a combination of hoist and crowd motion. However, according to Hendricks (1990), the hoist and crowd motor responses are not good indicators because they are related not only to the material properties, but also to the cut depth. For example, a hard digging condition can be experienced as an easy condition under shallow cut depth. In the same way, in easy digging conditions if excessive crowd is applied to reach a deeper cut depth, the machine will experience a hard digging condition (Hendricks, 1990).

Figure 5-1 shows a typical shovel dipper trajectory. As can be seen, a complete dig cycle involves three parts: placing the dipper in proximity to the bank, filling the dipper, and pulling the dipper up to clear the bank (Stavropoulou et al., 2013). At the first phase (AB), the shovel moves from the start point towards the toe of the rockpile and scoops loose materials. At the second phase (BC), the dipper penetrates the rockpile and digs the material up to the coasting phase. At the third phase (CD), the dipper clears the bank (Stavropoulou et al., 2013). If the dipper digs constantly, the final shape of the dipper trajectory would be logarithmic spiral (Hendricks, 1990). Variation from this trajectory results in overextended or very shallow paths, and therefore inappropriate productivity (Hadjigeorgiou, 1993).

In addition to the logarithmic spiral path as the shovel dipper trajectory, there is another similar path in the material (Hadjigeorgiou, 1993). Previous studies have indicated that the failure plane at the rockpile generated during a dig cycle is represented by a logarithmic spiral slip plane (Hadjigeorgiou, 1993). Also, based on the theory of soil cutting, the failure plane is best described by a logarithmic spiral slip plane (Reece, 1965). Figure 5-2 illustrates a non-planar crack trajectory inside a rockpile with a logarithmic spiral shape (BC) that connects to a linear part (CD). Based on this assumption, the cutting process of a shovel dipper has been modeled and defined as the following (Stavropoulou et al., 2013):

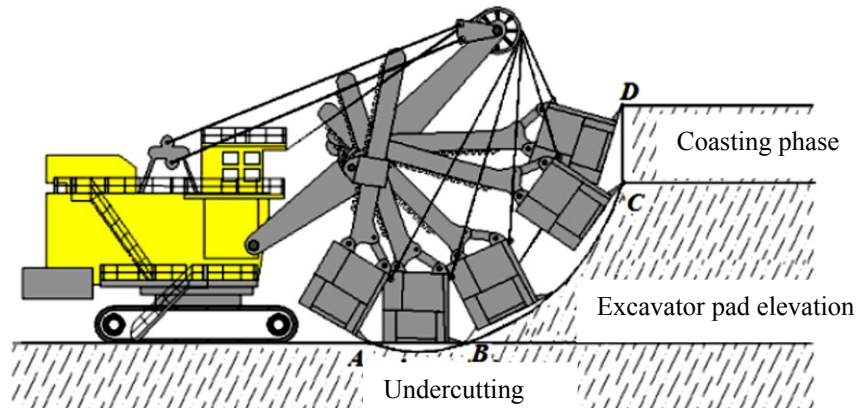


Figure 5-1 The three distinct digging phases performed by a cable shovel (adapted after Stavropoulou et al., 2013)

1. The first area ABC in Figure 5-3 consists of three parts of AB, BC, and AC. The part BC that is a vertical plane of the dipper teeth has the same orientation and length as the dipper teeth. This slip line takes into account penetration work of the teeth into the rockpile. The part AC that is the shear localization plane connects the teeth tip to the point at which the dipper side wall connects to the free surface, and the part AB is “the dipper cutting edge inside the material”. If the length of the dipper side wall inside the material (AB), and the length of the dipper teeth (BC) are known, then the angle formed between the side wall and the failure plane with part AC may be known (angle ρ in Figure 5-3).
2. The second area ACD represents a logarithmic spiral slip line surrounded with two areas of ABC and ADE.
3. The third area ADE is surrounded between AD, DE, and AE. Part AE is a shear band that forms the angle Ω to a horizontal line.

This chapter presents an analysis of this planar failure (focusing on the filling part from B to C in Figure 5-1) as a part of the experimental lab tests performed.

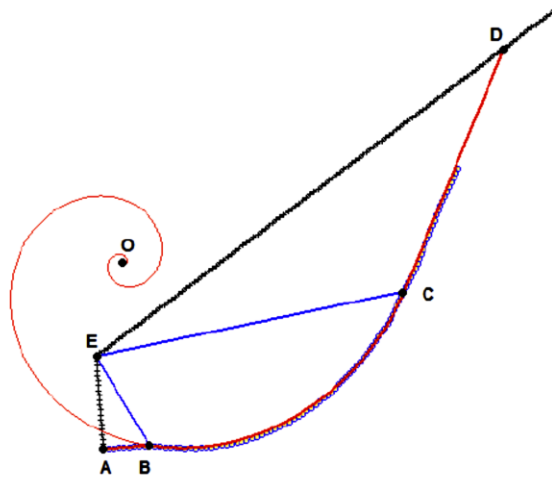


Figure 5-2 Crack trajectory (dotted line) resembling a normal fault (adapted after Stavropoulou et al., 2013)

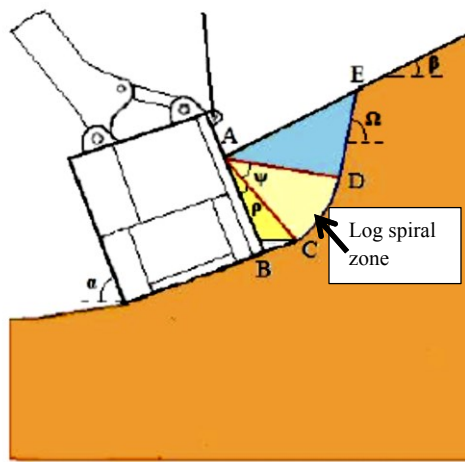


Figure 5-3 Soil cutting mechanism (adapted after Stavropoulou et al., 2013)

5-1- Test procedure

At the second set of the experiment, the main dipper profile and the same test bin were used. All setups were similar except the location of the camera. At this set of the experiment, the camera was mounted on a tripod outside of the transparent wall and the side view of the digging action was recorded to investigate the failure curvatures of the rockpile during each dig cycle.

The tests were run for the same hoist speeds and dipper pitch angles used at the first set of experiment. Each test was comprised of three runs that were considered representative of the

specific digging condition. The qualitative digging action was documented for each run. The following procedure was employed for each run of the test:

1. Mount the camera on the tripod outside of the box (on the side of the transparent wall).
2. Set the desired pitch angle and the desired motor speed.
3. Reshape the slope of the rock pile to avoid the influence of rockpile properties on the failure envelope creations.
4. Check the length of handle, to be constant to all tests.
5. Turn on the hoist motor to pull up the dipper and turn on the camera to record the dig cycle.
6. Stop the motor, and turn off the camera, when the dipper disengages from the rock pile.
7. Dump the dipper payload into a container.
8. Repeat the test three times.
9. Adjust the dipper pitch angle and motor speed for another condition.
10. Repeat the test.

5-2- Results and discussion

As mentioned previously, while the dipper digs the rockpile and filling (Figure 5-1, from B to C), two particle flows are formed: flow of material into the dipper and flow of material from two sides of the dipper. In addition to these particle displacements, another disturbance can be seen ahead of the dipper that is related to the movement of the dipper inside the rockpile. This disturbance is common with most of the tool-ground interaction theoretical models that assume there is a failure mechanism (planar or non-planar) of the material in front of the cutting edge of the dipper. Figure 5-4 shows these three flows.

As the dipper cutting the face and moving forward, some particles far from ahead of the dipper begin to drop off towards the dipper or toe of the rockpile. Observation of the dig action from the side view when performing the second set of the experimental lab tests contributed to the opportunity to investigate the failure of these particles. At each run of the test, the range of disturbed particles ahead of the dipper and the motion of their movements were recorded.

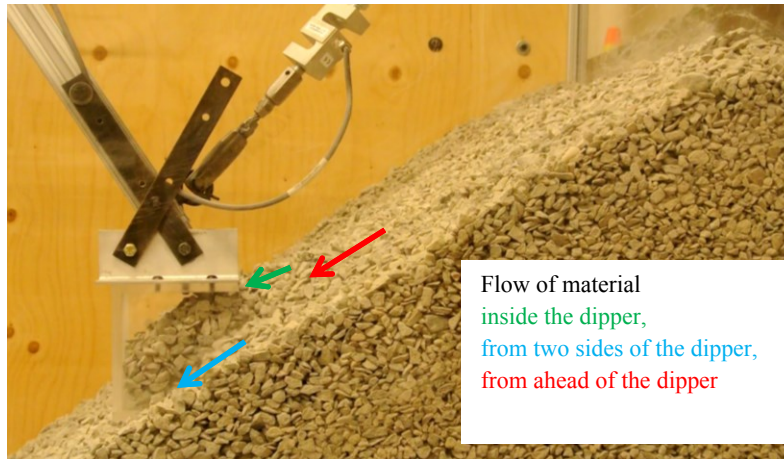


Figure 5-4 Different flow of material at the rockpile

The approximate distance of the beginning of such failures on the face to the lip of the dipper was recorded at each stage of the proposed particle flow pattern (described in Chapter 4) under different examined dig conditions (different hoist speeds and pitch angles). The failure lengths were recorded analytically based on the number of the dipper length (Table 5-1).

It was observed that the number of dropping particles and their distance to the dipper may vary from one cycle to another; therefore, to ensure the reliable and repeatable results, each experiment was repeated three times.

Table 5-1 shows the recorded results. As can be seen, at the first, second, and the last loading stages, the length of failure may be as small as a quarter of the dipper length, usually one length of the dipper, but during the third and fourth stages, it may be more than twice as large as the dipper length. Also, as was observed, hoist speed and pitch angle had no significant influence on variation of the failure's length.

The experiments demonstrated that the shape of the failure envelope depends on the relative position of the dipper to the rockpile. Where the dipper penetrates more into the rockpile, there will be longer failure curvature (middle stages), and in contrast, a shallower depth of cut that occurs at the first and last parts of the dig cycle causes shorter failure curvature. Deeper penetration causes more disturbances in the rockpile and results in a greater failure envelope. It is worth noting that in the current study, the trajectory of the dipper was circular rather than the common Spiro shape.

The circular trajectory enhances shallower depth of cuts at the first and last parts of the dig cycle and a deeper one at the middle parts.

Table 5-1 Length of failures ahead of the dipper estimated based on the dipper length at 9 different dig conditions

Condition	stage 1			stage 2			stage 3			stage 4			stage 5		
	run 1	run 2	run 3	run 1	run 2	run 3	run 1	run 2	run 3	run 1	run 2	run 3	run 1	run 2	run 3
low speed-pitch angle 30	1	1	1	1	1.5	1	1.5	1.5	2	1	2	2	0.25	0.25	1
medium speed - pitch angle 30	1	1	1	1	1	1	1.5	1.5	1.5	1.5	1.5	1.5	1	1	0.25
high speed- pitch angle 30	1	1	1	1	1	1	2	2	2	2	2	1.5	1	1	1
low speed- pitch angle 20	1	1	1	1	1.5	1.5	2	2	2	2	2	2	1	1	0.5
medium speed - pitch angle 20	1	1	1	1.5	1	1	1.5	1.5	2	2	2	1.5	0.5	0.5	0.5
high speed- pitch angle 20	1	1	1	1	1	1	2	2	1.5	2	2	2	1	0.5	1
low speed- pitch angle 10	1	1	1	1	1	1	2	2	2	2	2	2	1	0.75	1
medium speed - pitch angle 10	1	1	1	2	2	2	2	2	2	2	2	2	0.75	1	1
high speed- pitch angle 10	1	1	1	1	1	1	2	2	2	2	2	2	1	1	1
Mode of the observations	1			1			2			2			1		

The results of the experiment demonstrated that the mode of motion of the dropping particles were sliding and rolling (mostly sliding), and the intersection of the assumed failure envelope with the face of the rockpile (Figure 5-5) was the zone in which most of the particles displacements were observed. One explanation for the dislocation of this zone is, due to the increasing slope of the rockpile, gravity will assist the displacement of the failed particles and the longer distance to the dipper gives the particles enough time to show their mode of motions before reaching to the dipper.

One of the considerations was overlapping the failure envelopes on the dipper trajectory. It is believed that when the dipper follows such a logarithmic spiral path as digging trajectory, there will result less digging resistance and thus, higher productivity (Hadjigeorgiou, 1993; Stavropoulou et al., 2013). As reported by Hadjigeorgiou (1993), to follow such a path, the attack angle of the dipper needs to be fixed during a dig cycle. The attack angle is defined as “the angle between the base of the dipper and the tangent of the digging trajectory at any given point” (Hadjigeorgiou. 1993).

It was observed that there was not just a single failure envelope. As the dipper penetrates into the rockpile and cuts the material, new failure curvatures are generated; based on the dipper position and depth of cut, their length and probably curvature are different. The optimum dipper trajectory would be a tangent to the all failure curvatures developed during the dig cycle (Figure 5-6). It is expected that if the dipper follows such a path, there would result the maximum productivity. Further investigations are required to examine this hypothesis. Material properties are an important factor that must be considered. Compaction and particle interlocking, especially in angular particles, increase the material strength. Failures are more expected to be apparent in loose and less angular materials due to lower digging resistance.

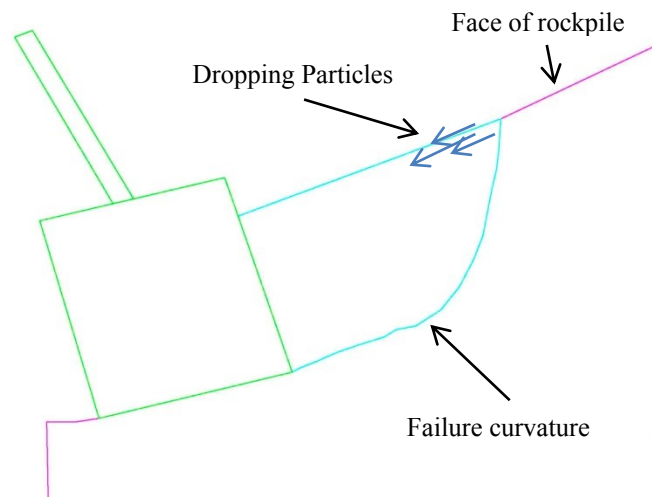


Figure 5-5 Failure envelope inside the rockpile

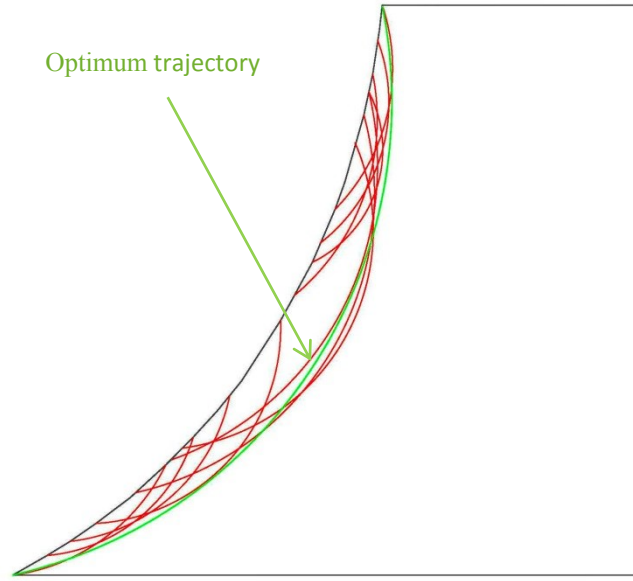


Figure 5-6 Optimum dipper trajectory

5-3- Conclusion

Granular particle flow into the modeled cable shovel was observed from the side view to investigate developing failure envelopes in the material during a dig cycle. It was found that a number of failure curvatures were developed at the rockpile during a dig cycle. These failure envelopes are different in their lengths and curvatures. The dipper cut depth and material properties influence the developing of such differently shaped failure paths. It was observed that deeper penetrations impact a wider area around the dipper, and therefore provide a bigger failure curvature. Material with higher diggability, more angularity, and more compaction resists more against digging and would result in a shorter failure path with a smaller curvature radius. The modes of motion of failed particles are mostly sliding and rotation. In loose material or more rounded particles, the number of dropping particles would be higher.

The final failure envelope is a tangent to the all failure curvatures developed during a dig cycle. If the dipper trajectory lays on such a path, that would be an optimum trajectory that results in maximum productivity. Investigation of such an optimum dipper trajectory was beyond the scope of this study, and is recommended for future studies.

Chapter 6

Scaling to full size dipper

Based on the experimental lab tests, the flow mechanism of granular material into a cable shovel dipper was investigated and a general flow pattern was proposed. However, the question is can we conclude in the full size cable shovel dippers, the same flow pattern will be observed.

The best answer for this question is a full size prototype test, but considering the cost of experimentation and the capability to repeat tests in a controlled environment, this is not a good application (Shi, 2007). However, if a relation can be derived from the existing data that connects the dipper performance and the dipper capacity (Shi, 2007; Joseph, 2010), and the similarity of the interaction of granular material and the dipper both in the lab and real size scale can be proven, this confirmation would allow a greater confidence in scaling the obtained results to the full size scale. In other words, if it can be shown that the performance of the scaled cable shovel dipper model is same as the performance of its full size dipper, and the interaction of the experimental lab material with the scaled dipper is same as the interaction of blasted material and full scale dipper, then it can be concluded that the behaviour of granular material in the field would be similar to the behaviour of material during the experimental lab tests.

6-1- Physical models

Modelling is a method of study that mimics rather than studying the actual entity or phenomenon (Hadjigeorgiou, 1993). Models that are used in different scales in industries and academic areas can be categorised as the following (Hadjigeorgiou, 1993):

- “Physical”, regarding to the characteristic of the object needed to be examined
- “Computer”, based on numerical formulas or learning bases
- “Analog”, in case of using electrical systems
- “Limited”, modeling only certain features of the object
- “Distorted”, in a case that various elements follow various regulations

The first category (physical models) consists of models used in fundamental researches, when decreasing essential elements of model performance is endeavoured (Hadjigeorgiou, 1993). Suggested by Hadjigeorgiou (1993), developing such a model has three operation stages. The first task is identifying a desired prototype, in order to simplify the real object and remove all unessential elements, and based on that, constructing a model. The second stage is performing the test under different operational conditions. The third stage lies in investigating the likelihood of extrapolating the results from the experiment to the actual object, which needs adapting the results to be useable in the prototype (Hadjigeorgiou, 1993).

One of the main benefits of using models is that they only need to focus on the elements of the prototype that are critical for a study. Therefore, it is not necessary to model all aspects of a design, but only those that are important for an analysis (Hadjigeorgiou, 1993).

6-2- Dipper analogy

6-2-1- Geometry analogy of the dipper

Geometry, construction, and composition similarity of a designed and a full scale dipper is one of the initial principles in obtaining a relationship between dipper capacity and dipper performance (Shi, 2007; Joseph, 2010).

Figure 6-1 illustrates the comparison of the geometry configurations of the dipper of P&H4100 with the capacity of 44 m³ and a prototype of the main scaled model dipper used at the current study. If the dimensions of the dipper model are scaled up to 32 times, they will match the size of P&H4100 dipper. By ignoring the minor geometric differences, the scaled model dipper has a very similar configuration to that of the current P&H dipper. The main difference is that the dipper model does not have teeth, for the simplicity of the model. A favourable tooth configuration penetrates more into the face and possibly results in a higher fill factor and therefore, possible increased power consumption (Patnayak, 2006). In other words, the smaller the teeth angle, the lower the digging resistance. Therefore, it may be assumed that the model has a single short tooth that makes an angle of 0 to the front wall of the dipper. In reality, due to severe wear on the rake front, employing the lowest attack angle in all conditions is not a good idea (Shi, 2007). In the current study, to minimize the influence of the lack of traditional teeth that resulted in reducing

the ground impact and a lower fill factor, an optimum depth of cut was employed to achieve a reasonable fill factor at the end of the dig cycle.

Another difference is due to the angle η , which is the hoist rope angle with the horizon. However, this angle in the scaled model was smaller; it was therefore not expected to appreciably affect the comparison between the two shovel models.

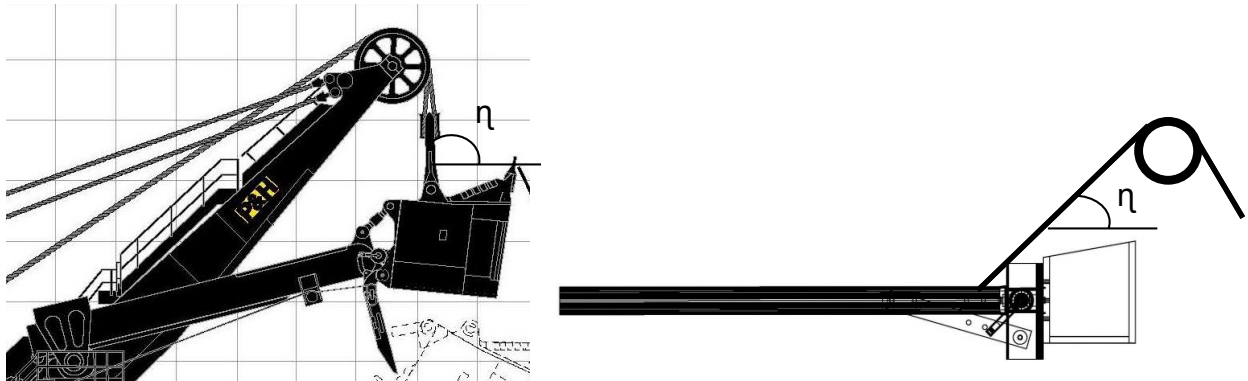


Figure 6-1 Geometry of P&H 4100 dipper (Joy Global, 2012) vs. examined scaled model

6-2-2- Crowd analogy

The dig action of a cable shovel is performed by the hoist and crowd assemblies. In hoisting, the dipper is dragged up through the face, whereas crowding makes sure that the dipper has penetrated sufficiently into the rockpile during the dig action (Patnayak, 2006; Patnayak, et al, 2008). In the current study, the crowding action was eliminated by fixing the length of the handle.

In a crowding action, the dipper engages the rockpile and makes the material around the dipper teeth and lip has shearing and volumetric displacements; however, the hoisting action has the main influence in material fragmentation, shearing and fluffing (Patnayak, 2006; Patnayak, et al, 2008). Therefore, the role of crowding is minor in comparison to the hoisting in shearing and moving the material (Patnayak, 2006; Patnayak, et al, 2008). If the crowd element for each dig cycle is kept constant, there will be the same depth of penetration during each dig cycle, and then the required dig effort can be signified only with the hoist system. This issue has been mentioned in many cable shovel performance investigations by different authors (Karpuz et al., 2001; Patnayak, et al, 2005; Patnayak, 2006; Shi, 2007; Patnayak, et al, 2008; Joseph et al., 2010). In the current study, by

fixing the length of the handle at a specific value, and maintaining the equivalent depth of cut during each dig cycle, the same concept was employed and therefore, the hoist effort was considered as the total required effort for digging material.

Another concern may be the trajectory of the dipper. In general, a cable shovel dipper has a logarithmic spiral shape during a dig cycle (Hadjigeorgiou, 1993; Shi, 2007; Wei and Gao, 2012). In the present experiment, however, a fixed handle resulted in a circular shape trajectory (Figure 6-2).

Based on the previous studies, in the cable shovels, the dipper trajectory depends on the hoisting and crowding actions (Hadjigeorgiou, 1993; Wei and Gao, 2012). By employing continuous motions, the log spiral trajectory would be the optimal digging trajectory with less energy consumption. The reason is that by following such a path, the digging angle is unchanged (Hadjigeorgiou, 1993; Wei and Gao, 2012). Deviation from this trajectory results in over-extending or very shallow paths, and thus, improper energy consumption and low productivity (Hadjigeorgiou, 1993; Wei and Gao, 2012). However, since an ideal resulting digging trajectory allows for the dipper to be filled as it reaches the top of its digging trajectory, in the current study a laboratory set-up was exploited that gave the dipper a high fill factor with reasonable digging effort. This experiment was performed by examining different dipper handle lengths that lead to different depths of cuts and by then comparing their results.

It is of interest to note that, as Hadjigeorgiou (1993) concluded, although it is usually expected that all scaled models be geometrically comparative to the full size prototypes, as long as the features that interact with the ground are completely simulated, the model is satisfactory, and only if they do not impact the machine efficiency, are they allowed to be simplified (Hadjigeorgiou, 1993). It was not the purpose of this research to produce an identity of the prototype. Rather, the project was planned to study certain aspects of the digging cycle, deriving a clear understanding of the fundamental digging mechanism. Thus, certain choices were made at the time of construction to ensure that the model would perform as similarly to the prototype as possible.

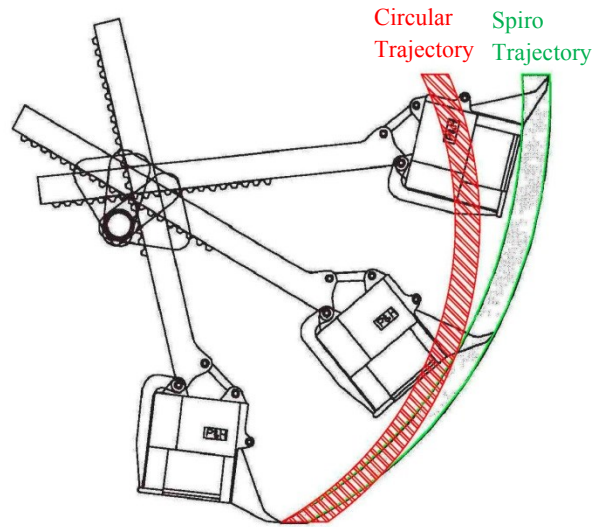


Figure 6-2 Spiro shape trajectory versus circular shape trajectory

6-2-3- Performance analogy of the dipper

To analyse the performance of the scaled models, the performance of two full size cable shovel dippers was compared with the performance of two scaled models used in the current study. All field performance data in this section came from P&H medium-sized (capacity of 23 m³) and ultra-sized shovels (capacity of 44 m³) that were compared with the results of the two scaled dipper models with the nominal capacity of 1.3*10⁻³ and 4.9*10⁻³ m³, representing the main dipper model with the scale size of 1:32 and the secondary dipper model with the scale size of 1:23 in the current study, respectively.

A summary of the four shovels' specifications and hoist performance is illustrated in Table 6-1. All field data derived from hard broken rocks. It was assumed that the reference point for a free suspended load condition was a condition during which the dipper fill factor is 1 and the handle is parallel to the horizon (Shi, 2007; Joseph, 2010). Also, to make sure that all the dippers were considered under the same condition, it was assumed that in all conditions the dipper was fully loaded, so when the fill factor of a dipper was less than 1, the equivalent capacity was used.

With the data from Table 6-1, the relation between dipper capacity versus suspended load and peak force is shown in Figure 6-3. The traces show that the hoist force is relative to the dipper capacity, as is common with the findings of Hadjigeorgiou (1993), Shi (2007), and Joseph (2010). In other

words, the scaled dippers followed the rule of linear relationship between the hoist force and the dipper capacity.

Table 6-1 Shovel specifications and performance

Parameter Model	Main scaled model	Secondary scaled model	P&H 2300	P&H 4100
Capacity (m3)	0.0013	0.0049	23	44
Fill factor	0.9	0.6	1	1
Equivalent capacity (m3) (fill factor=1)	0.0012	0.0032	23	40
Payload (kg)	1.72	4.45	39000	61380
Dipper handle (kg)	1.98	2.79	51480	90325
Peak hoist force (kg)	14.46	15.78	125280	237694
Suspended load (kg)	4.27	9.62	90480	151705
Reference	lab experiment	lab experiment	Shi (2007)	field data (Appendix B)+Shi (2007)

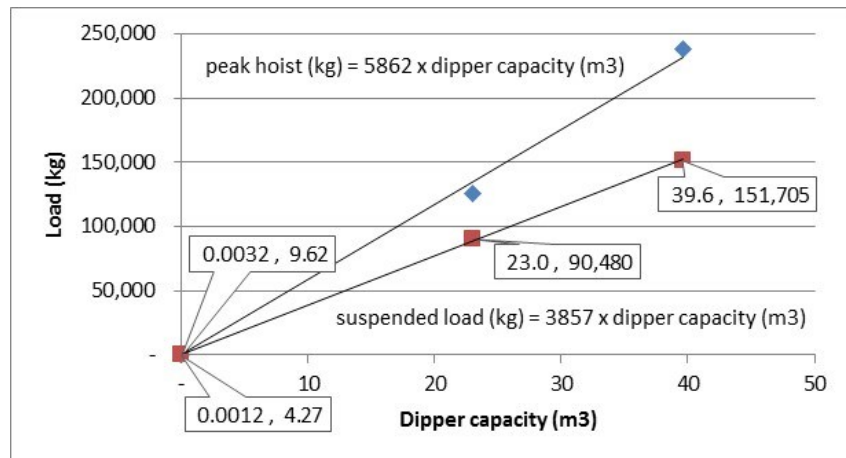


Figure 6-3 Dipper capacity versus suspended load and peak hoist force

Figure 6-4 illustrates the linear relationship between hoist force and dipper capacity of the two scaled models. Based on this relation, the peak hoist force and the suspended load of the full scale

dippers were predicted. As Table 6-2 shows, the ratio of measured to predicted values implies that the hoist performance of the scaled models can be extrapolated to the full scale dippers. Therefore, obtaining a high correlation between the dipper size and the hoist force would allow the extrapolation of the obtained results of the physical model to the full size dipper.

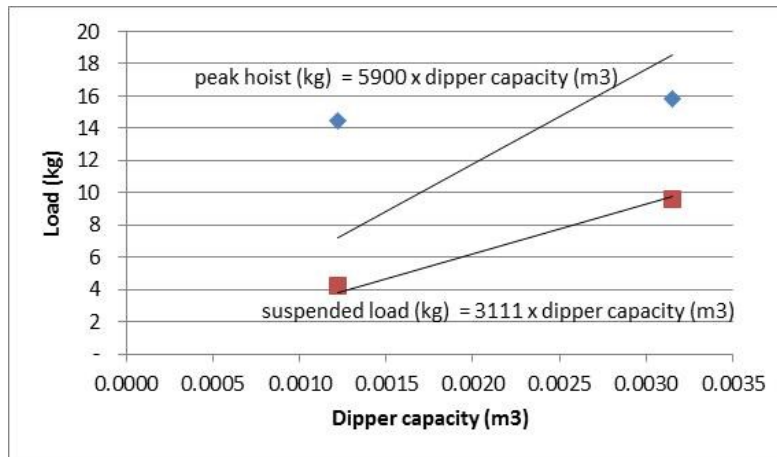


Figure 6-4 Dipper capacity versus suspended load and peak hoist force of scaled dippers

Table 6-2 Predicted key performance for full scale dippers

Model	Capacity (m3)	Performance	Measured (kg)	Predicted (kg)	Ratio
P&H 4100	44	peak hoist force	237694	233640	1.02
		suspended load	151705	123196	1.23
P&H 2300	23	peak hoist force	125280	135700	0.92
		suspended load	90480	71553	1.26

6-3- Material analogy

6-3-1- Size distribution analogy

Particle size and size distribution are probably the most important physical characteristics of the material. Since these characteristics influence the flow characteristics of granular material, it is critical to exploit a method to assess the size distribution of material. There are different methods

for this purpose, ranging from empirical to numerical models. The Rosin-Rammler size distribution is one of the most well-known and popular distribution functions used in a broad range of application areas, especially in fragmentation processes including grinding, milling, and crushing operations (Morrell, et al., 1998; Macias-Garcia, et al., 2004; Alderliesten, 2013).

The usual expression of the Rosin-Rammler (RR) model is as follows (Macias-Garcia, et al., 2004):

$$F(d) = 1 - \exp \left[-\left(\frac{d}{d_m}\right)^n \right] \quad [6- 1]$$

where $F(d)$ is the distribution function, d is the particle size (mm), d_m is the mean particle size (mm), and n is a measure of the spread of particle sizes. d_m and n are adjustable parameters characteristics of the distribution. This equation can be rewritten as follows (Macias-Garcia, et al., 2004):

$$\ln\{-\ln[1 - f(d)]\} = n \ln(d) - n \ln(d_m) \quad [6- 2]$$

If the plot of the left side of the above relation versus $\ln(d)$ makes a straight line with slope n , then the size distribution of the examined granules fit RR model (Macias-Garcia, et al., 2004).

To examine the applicability of this model on available data, it is required to plot $\ln\{-\ln[1 - f(d)]\}$ versus $\ln(d)$, and apply a least-squares regression analysis. Then, to estimate the accuracy of fit, the correlation coefficient parameter is calculated (Macias-Garcia, et al., 2004).

Figure 6-5 shows the result of estimating the size distribution of the used crushed limestone by employing WipFrag software, which is the digital image processing system used for the current study. Table 6-3 lists the required parameters to be fitted with the RR model based on the results of the size distribution analysis. Figure 6-6 depicts the fit of the experimental data to the RR model. From the observation of the figure and the corresponding linear correlation coefficient, it can be concluded that the RR model provides a good fit to the experimental particle size distribution curve.

Also, based on the trend-line equation, n (slope of the straight line) is equal to 1.4779 and $n \cdot \ln(d_m)$ is equal to 4.51. Therefore, d_m (mean particle size) will be estimated as 1.3 cm, which is very close

to the nominal mean particle size of the used material that is approximately 1 cm. This may be considered as another confirmation that the size distribution of the material follows RR model.

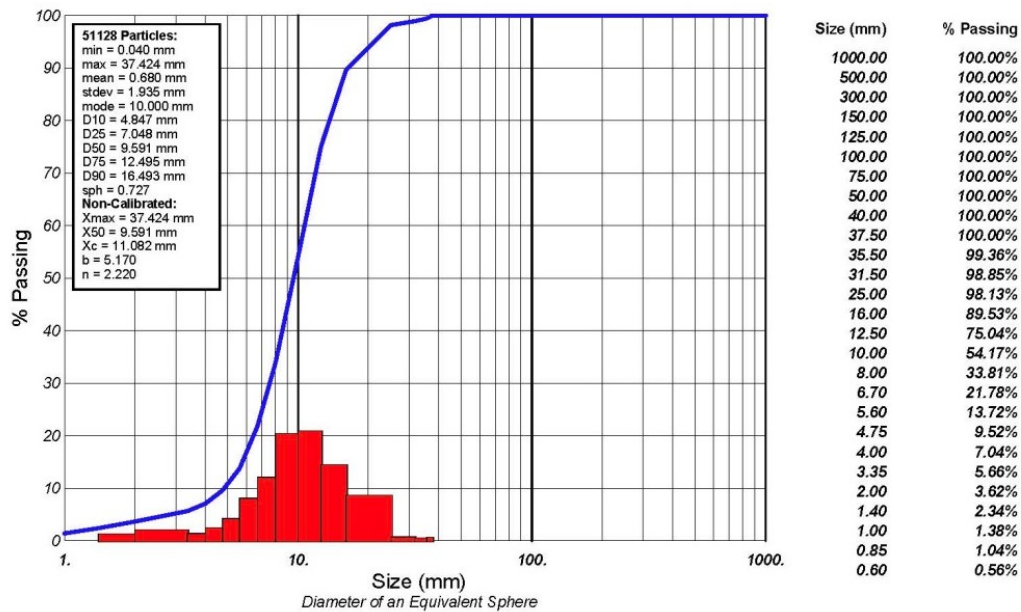


Figure 6-5 Size distribution of crushed limestone

Table 6-3 Required parameters to fit to RR

d (mm)	cumulative weight %	F (d)	ln(-ln(1-F(d)))	ln (d)
37.5	100	1.000	-	3.624
35.5	99.36	0.994	1.620	3.570
31.5	98.85	0.989	1.496	3.450
25	98.13	0.981	1.381	3.219
16	89.53	0.895	0.814	2.773
12.5	75.04	0.750	0.328	2.526
10	54.17	0.542	-0.248	2.303
8	33.81	0.338	-0.885	2.079
6.7	21.78	0.218	-1.404	1.902
5.6	13.72	0.137	-1.913	1.723
4.75	9.52	0.095	-2.302	1.558
4	7.04	0.070	-2.617	1.386
3.35	5.66	0.057	-2.843	1.209
2	3.62	0.036	-3.300	0.693
1.4	2.34	0.023	-3.743	0.336
1	1.38	0.014	-4.276	0.000
0.85	1.04	0.010	-4.561	-0.163
0.6	0.56	0.006	-5.182	-0.511

Since the size distribution of most materials, resulted from the blasting, follows the RR model (Macias-Garcia, et al., 2004; Onederra et al., 2004; Osanloo, 2005; Müller et al., 2010; Strelec et

al., 2011), one may deduce that as regards the size distribution, the material used in the current study may represent the blasted material in mining activities, but with scaled particle sizes.

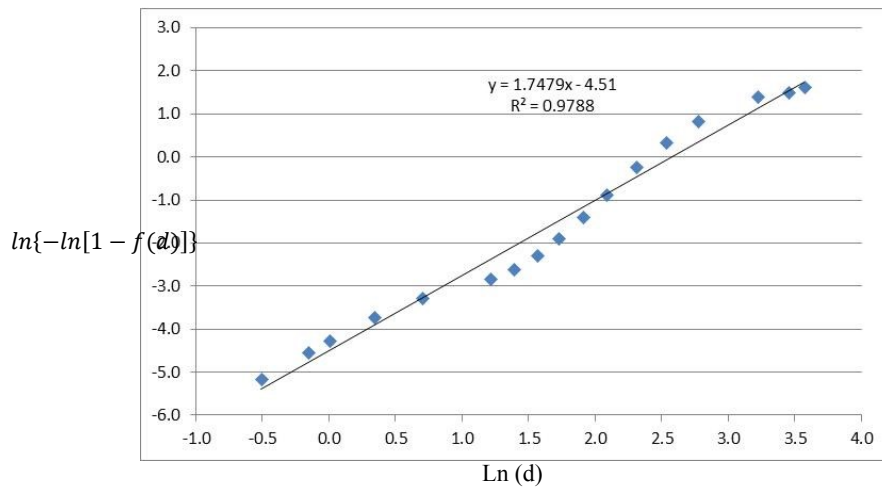


Figure 6-6 Fit to the RR model

6-3-2- Particle size analogy

Based on the general design principle adapted by shovel dipper designers (Joseph, 2013, personal communication), the material largest particle size should not be greater than one-third of the width of the dipper lip; otherwise the big particles will cause entry blockage and will dramatically reduce the granule flow into the dipper. This assumption is considered at the phase of equipment selection.

In the current study, the scaled dipper was designed in respect to the mentioned hypothesis. Therefore, the used granular material (crushed limestone) was scaled as well as the dipper itself. In other words, the ratio between the maximum particle size and the dipper size was kept constant.

6-4- Conclusion

Different scaling approaches including geometry and operating were used to evaluate the extrapolation of the results of the experimental lab test to the full scale. The geometry of the main scaled model dipper was shown to be similar to the full size dipper by a linear increase of 32. Although there were some differences in the structure and mechanical configurations of the model, an appropriate cut depth was employed to minimize the influence of dissimilarities. Correlation between different size scaled models and the full size machine performance, using the available filed and lab data, showed the possibility of prediction of full size prototype dippers from small

scaled models. Also, regarding the material, it was demonstrated that the used fragments followed the three times maximum particle size rule with the size distribution fitted to the most common model among blasted and crushed materials. The outcome yielded that the obtained results may be scaled up to full size cable shovel dippers with reasonable confidence.

Chapter 7

Discrete element method

Although in some cases experimental models seem easy and perceptive, one may question their applicability to objects other than the tested ones (Frimpong et al., 2007). A common way to verify their applicability is through theoretical or numerical modelling. Today there is a large number of software with different approaches, such as limit equilibrium techniques, computational limit analysis methods such as finite element limit analysis and discontinuity layout optimization, and very complicated and high-tech numerical modeling such as finite and distinct element codes (Wikipedia). These methods differ in simplifications and accuracy. In this chapter, the two most common and important methods were explained and discussed under the categories of “Limit Equilibrium Methods” and “Numerical Analysis Methods”. Further, particle flow code (PFC), a numerical model, used in the current study to investigate cable shovel filling numerically, was described in detail.

7-1- Limit equilibrium analysis

The methods of limit equilibrium analysis have been applied extensively for the stability analysis of earth slopes in engineering problems (Krahn, 2003). These methods compare the shear strength of both sides of each slice and use them to estimate the factor of safety of the slope under the condition that the slope is stable (Chiwaye, 2010).

In some cases, it is highly recommended to use slice methods, as reported by Bishop (1955), Janbu (1954), Nonveiller (1965), Spencer (1967), Morgenstern and Price (1965) or Sarma (1979), for instance, when the slope has a non-uniform shape, and the generated failure envelope has a circular curve that does not cross the toe of the slope (Chiwaye, 2010).

In all the slope stability analysis methods, a failure zone is divided into slices (Sinha, 2008). To predict the stress on the mobilized surface, the static equilibrium state for each slice is used (Chang, 1992) through summation of moments, and vertical and horizontal forces (Krahn, 2003). A slice of earth subjected to the forces is shown in Figure 7-1.

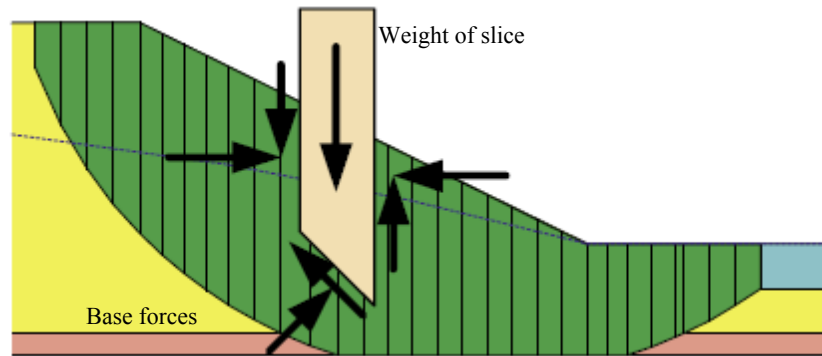


Figure 7-1 slices and forces in a sliding mass (adapted after Krahn, 2003)

To calculate the factor of safety, each method assumes different equilibrium conditions, therefore the obtained factor of safety from each method would be different from the other ones (Sinha, 2008). For instance, the force equilibrium condition is not considered by some methods such as the ordinary method of slices and Bishop's method. In contrast, in some methods the moment of equilibrium condition is not satisfied; methods such as the infinite slope analysis, wedge analysis, and Janbu's are examples. However, the methods of Spencer, Morgenstern and Price, and Janbu consider both force and moment equilibrium conditions, and therefore are more advanced and complicated (Chang, 1992). The equilibrium conditions for different methods are shown in Table 7-1.

Since there is not a specific way for rockpile failures, selecting the best analysing method depends on the designer's decision (Sinha, 2008). Moreover, the value of some parameters, such as base normal force, inter slice shear and normal forces, and factor of safety, are unknown and independent together. Consequently, to calculate the factor of safety, it is necessary to assume a value for some of them (Sinha, 2008).

7-1-1- Limitation of common limit equilibrium method

A more detailed look at the limit equilibrium method of slices reveals that this method has some serious limitations (Krahn, 2003). For instance, strains and movements are not considered, and as a result it does not satisfy particle displacements (Krahn, 2003; Sinha, 2008; Chang, 1992; Chiwaye, 2010).

The limit equilibrium method is unable to give true stress distributions, because it is basically based on static conditions, and does not consider displacements (Krahn, 2003). Therefore, when a movement happens, its effect cannot be considered in the stability of the slope (Chiwaye, 2010). Moreover, they simplify problems in their scope of application, while in reality, lots of complications might exist regarding “geometry, material anisotropy, non-linear behaviour, in situ stresses, and the presence of several coupled processes” (Chiwaye, 2010). In addition, the limit equilibrium analysis assumes that the failure is sliding a mass of material on a mobilized surface (Chang, 1992). Hence, it is not suitable for dis-continuum cases like excavating granular material through a ground engaging tool. Therefore, one of the best methods to solve such problems is to employ numerical methods (Chiwaye, 2010).

Table 7-1 Different method of stability analysis indicating equilibrium conditions, forces and factor of safety considered (adapted after Sinha, 2008)

No.	methods	moment equilibrium	force equilibrium	inter slice normal force	inter slice shear force	moment of factor of safety	force of factor of safety	inter slice force function
1	Culman wedge block method (no-slice)	No	Yes	No	No	No	Yes	No
2	Fellenius, Swedish circle or ordinary method (1936)	Yes	No	No	No	Yes	No	No
3	Bishop Simlified method (1955)	Yes	No	Yes	No	Yes	No	No
4	Janbu Simlified method (1954)	No	Yes	Yes	No	No	Yes	No
5	Spencer method (1967)	Yes	Yes	Yes	Yes	Yes	Yes	constant
6	Morgenstern-Price method (1965)	Yes	Yes	Yes	Yes	Yes	Yes	constant half-sine clipped- slice trapezod specifid
7	Corps of Enginnering #1 method	No	Yes	Yes	Yes	No	Yes	Yes
8	Corps of Enginnering #2 method	No	Yes	Yes	Yes	No	Yes	Yes
9	Lowe-Karafiath method	No	Yes	Yes	Yes	No	Yes	Yes
10	Sarma method (1973)	Yes	Yes	Yes	Yes	Yes	Yes	Yes
11	Janbu Generalized method (1957)	No	Yes	Yes	Yes	No	Yes	Yes

7-2- Numerical modelling

In numerical modelling, a slope is broken down into a few parts, and then specific formulas are used to estimate forces and displacements of each part (Chiwaye, 2010). The numerical methods may be categorised into continuum and dis-continuum methods. In continuum codes, the material body is supposed to be continuous; for instance, intact, weak, or heavily jointed rocks (Chiwaye, 2010). Dis-continuum methods consider interfaces between the parts that are continuum, and are used when the slopes have discontinuities (Chiwaye, 2010).

Currently, different numerical methods are available. The common methods for continuum modelling are Finite Difference Method (FDM), Finite Element Method (FEM), and Boundary Element Method (BEM), and for dis-continuum modelling, Distinct Element Method (DEM), Discontinuous Deformation Analysis (DDA), and Bonded Particle Model (BPM) (Pourkhosravani et al., 2011). To decide which method should be used, it is necessary to compare the size or scale of the discontinuities and the problem in question (Pourkhosravani et al., 2011).

In the current study, DEM method was used to investigate the behaviour of granular particles at the rockpile during the dig action of a cable shove dipper. The used DEM code is PFC v5.0 which was developed by Itasca Codes and was based on the Cundall and Strack (1979) code.

7-3- Discrete element method

According to Cundall and Strack (1979), the discrete element method (DEM), which is a numerical model, is used to study the interaction of granular materials that may be modeled as discs in 2D or spheres in 3D. Particles influence each other only at their contact areas; however, the movement of each particle is an independent parameter. At each time step, all contacts of each particle are checked, and the final position of the particle is modeled. This process is performed for all particles in the system. This assumption can help to define the location of the particles based on the resultant contact forces (Cundall and Strack, 1979). The method is based upon four assumptions for an explicit numerical model (Tiphavonnukul, 2002-A&B):

1. Simulated particles representing a granular material are expected to be stiff.
2. A soft contact approach is used to model particle contacts.
3. The contact area is assumed to be very small.

4. The force-displacement relationship determines how contact forces influence the value of particle overlaps.

In the discrete element method, the displacements of each particle are monitored to calculate the applied forces and position of each particle (Cundall and Strack, 1979). Therefore, it is required to set a time step during which all velocities and accelerations are unchanged. Otherwise, the system is numerically unstable (Cundall and Strack, 1979). In addition, since the response of a system to a change depends on the material properties, based on these properties, the critical time-step of each system is different (Tiphavonnukul, 2002 -A&B). PFC (particle flow code) is one of the DEM methods, which was used for the current study.

7-3-1- A brief description of PFC

PFC (2D/3D) is a dis-continuum code that is a useful method to study the behaviour of individual particles with huge displacements or breakages (Itasca Consulting Group Inc., 2014-A). PFC can be used widely in many areas, for instance, any dynamic system ranging “from rapid flow to brittle fracture of a rigid solid” (Itasca Consulting Group Inc., 2014-A). PFC, which has documented all the mathematical relations, uses a stable method to solve unstable systems (Itasca Consulting Group Inc., 2014-A). The accuracy of the described non-linear behavior and localization cannot be compared to any typical finite element programs (Itasca Consulting Group Inc., 2014-A).

PFC is a command-based solver in FISH programming language that requires being written by a user to specify the desired simulation properties (Dymond, 2007). PFC has two principal elements to define granules and rigid bodies, namely balls and walls, respectively (Dymond, 2007). Moreover, simulated granules could be modeled as bonded particles to represent cemented material, or as a combination of two or more balls to represent non-circular particles named clumps (Itasca Consulting Group Inc., 2014-A).

7-3-2- Force displacement law

According to Cundall and Strack (1979), all calculations in DEM are based on two fundamental laws; Newton’s second law, and the force-displacement law. The first law is applied to the particles, and the second law is applied to the contacts. The force-displacement law in DEM

connects the contact force and the particle overlap together as equation [7-1] (Cundall and Strack, 1979):

$$\Delta F_n = K_n \Delta_n \quad ; \quad \Delta F_t = K_t \Delta_t \quad [7-1]$$

where ΔF_n and ΔF_t are normal and shear forces, respectively; K_n and K_t are the normal and shear stiffness, respectively; and Δ_n and Δ_t are the normal and shear particle overlaps, respectively (Cundall and Strack, 1979, Tiphavonnukul, 2002-B).

Primarily, by knowing the location of each particle in the system, a list of all particle contacts can be provided, and based on the particle overlaps, and applying the force-displacement law, the resultant force will be calculated (Tiphavonnukul, 2002-B).

Using a soft particle approach, linear springs are employed to simulate normal and tangential contacts, and friction coefficient (μ) is used to add a frictional slip in the tangential direction, Figure 7-2 (Coetzee et al., 2010). Since in DEM two particles may overlap, their contact force can be estimated using the amount of their overlap and the stiffness of the spring between them, so the normal contact force may be written as (Coetzee et al., 2010):

$$\mathbf{F}_n = -\sum \mathbf{k}_n \mathbf{U}_n \quad [7-2]$$

where U_n is the overlap in the contact normal direction. The contact shear force may be written as

$$\mathbf{F}_s = \begin{cases} \sum \mathbf{k}_s \Delta \mathbf{U}_s & \text{for } |\mathbf{F}_s| < |\mu \mathbf{F}_n| \\ \mu \mathbf{F}_n \text{sign}(\sum \Delta \mathbf{U}_s) & \text{for } |\mathbf{F}_s| \geq |\mu \mathbf{F}_n| \end{cases} \quad [7-3]$$

where ΔU_s is the overlap in the contact tangential direction.

The mentioned equations are used to model linear contact models. In addition, DEM has non-linear contact models that are as effective as linear contact models (Coetzee et al., 2010). It is worth mentioning that by providing more bonds at the particle contacts, it is possible to add cohesion between the simulated particles (Coetzee et al., 2010).

After calculating the resultant forces between particles, and by assuming that during a time-step the particle location, velocity and acceleration will not change, a researcher can calculate the new position of each particle using Newton's second law of motion (Tiphavonnukul, 2002-B).

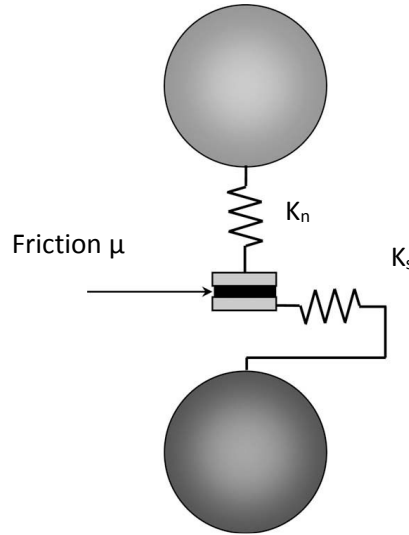


Figure 7-2 Typical DEM particle contact model (adapted after Coetzee et al., 2010)

7-3-3- Law of motion

Based on the translational and rotational velocities of each particle, Newton's second law applied to a particle may be written as follows (Cundall and Strack, 1979; Tiphavonnukul, 2002-B):

$$m_x \ddot{x}_i = \sum F_{xi} \quad [7-4]$$

$$I_x \ddot{\Theta}_x = \sum M_x \quad [7-5]$$

where m_x represents the particle mass x , and I_x represent the moment of inertia of particle x (Cundall and Strack, 1979; Tiphavonnukul, 2002-B). Taking the translational and angular acceleration constant over the time interval Δt , equations (7-4) and (7-5) lead to the following expressions for the next time step velocities (Tiphavonnukul, 2002-B):

$$(\dot{x}_i)_{N+1} = (\dot{x}_i)_N + (\sum F_{xi} / m_x)_N \Delta t \quad [7-6]$$

$$(\Theta_x)_{N+1} = (\Theta_x)_N + (\sum M_{xi} / I_x)_N \Delta t \quad [7-7]$$

where $\sum F_{xi}$ represents the summation of all forces acting on the particle x , including contact forces, body forces, drag forces, buoyant forces, and etc. (Tiphavonnukul, 2002-B).

By applying the mentioned equations to the all particles in a system, each particle may have a new velocity that will be used for the calculations of the next time-step, and also for renewing the location and rotation of the particles (Cundall and Strack, 1979; Tiphavonnukul, 2002-B):

$$(\dot{x}_i)_{N+1} = (\dot{x}_i)_N + (\dot{x}_i)_N \Delta t \quad [7-8]$$

$$(\Theta_x)_{N+1} = (\Theta_x)_N + (\Theta_x)_N \Delta t \quad [7-9]$$

In case of the existence of gravitational forces as body forces, equation (7-4) will have an additional parameter, $m_{(x)}g_i$, which will be totaled with the force sum $\sum F_{xi}$. Thus the two components of the acceleration vector resulting from body force will be shown as $g_i = (g_1, g_2)$ (Cundall and Strack, 1979).

7-3-4- Contact models

Collision generates a force that drives particles apart (Dymond, 2007). In DEM, the methods of “rigid” and “soft” body contacts are available to model the velocity of particles after collision; however, these methods employ different approaches (Dymond, 2007). In rigid body contacts, the original particle velocity and the coefficient of restitution are used, while in soft body contacts, such overlapping is not restricted, and the contact force is estimated based on the value of particle overlaps (Dymond, 2007). PFC usually considers soft body contacts, including linear and non-linear models. Only linear contact models will be discussed in detail in this chapter.

7-3-4-1- Linear contact models (Tiphavonnukul, 2002-A)

The linear contact models relate movements of particles in contact with their contact forces (Tiphavonnukul, 2002-A). According to Tiphavonnukul (2002-A), the contact force has two principals, namely, normal and shear contact forces, relative to the contact surface. Figure 7-3 shows particles A and B in contact with center coordination of (x_{A1}, x_{A2}) and (x_{B1}, x_{B2}) , respectively, and vector velocities of $(\dot{x}_{z1}, \dot{x}_{z2})$ in a Cartesian coordinate system. In velocity vectors, the subscript letter represents the particle, and the subscript number represents the axis. Also, the angular velocities are Θ_A and Θ_B , and are considered positive in a counter clockwise direction (Tiphavonnukul, 2002-A). In Figure 7-3, R_A and R_B are particle radiuses, m_A and m_B are particle masses, and P_A and P_B are the intersection points where the particles’ center line crosses the particle boundaries (Tiphavonnukul, 2002-A).

Based on Tiphavonnukul (2002-A), two particles are considered to be in contact when the total of their radiuses is smaller than the distance of their centers:

$$D < R_{(x)} + R_{(y)} \quad [7-10]$$

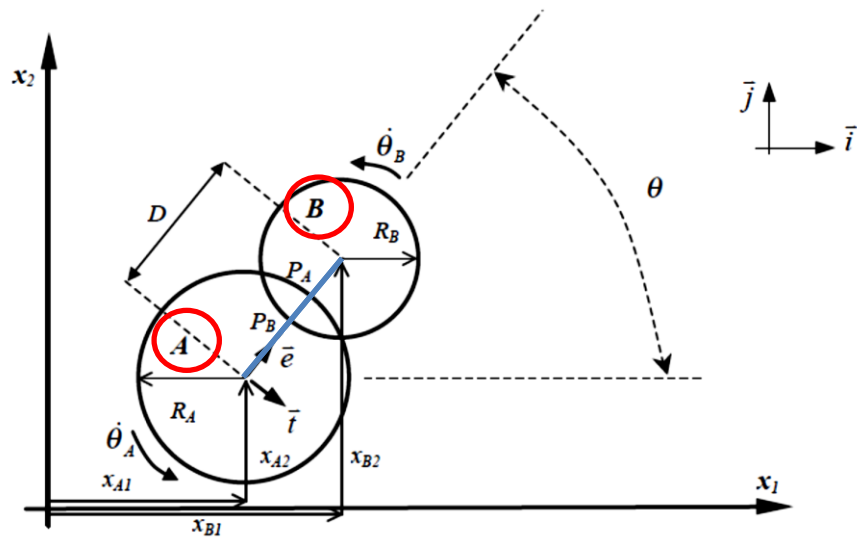


Figure 7-3 Two particles in contact (adapted after Tiphavonnukul, 2002-A)

As illustrated in Figure 7-3, the unit vector $\bar{e} = (\cos\theta, \sin\theta)$ faces towards the center of the particle B from the center of the particle A (Tiphavonnukul, 2002-A):

$$\bar{e} = \cos\theta \bar{i} + \sin\theta \bar{j} = e_1 \bar{i} + e_2 \bar{j} \quad [7-11]$$

where e_1 is $\cos\theta$ and e_2 is $\sin\theta$. Clockwise rotation of \bar{e} by 90° results in the unit vector \bar{t} as:

$$\bar{t} = \sin\theta \bar{i} - \cos\theta \bar{j} = e_2 \bar{i} - e_1 \bar{j} \quad [7-12]$$

Therefore, the coordinate and the velocity of the point P_A will be (Tiphavonnukul, 2002-A):

$$x_{pi} = x_{Ai} + R_A e_i \quad [7-13]$$

$$\dot{x}_{PAi} = \dot{x}_{Ai} + R_A \dot{e}_i = \dot{x}_A - R_A \dot{\theta} t_i \quad [7-14]$$

With the same equations, but replacing the angle θ in the equation (7-14) by $180 + \theta$, the velocity of the point P_B and the relative velocity of the two points may be calculated as follows (Tiphavonnukul, 2002-A):

$$\dot{x}_{PBi} = \dot{x}_{Bi} + R_A \Theta_B t_i \quad [7-15]$$

$$\dot{x}_i = \dot{x}_{PAi} - \dot{x}_{PBi} = (\dot{x}_{Ai} - \dot{x}_{Bi}) - (R_A \Theta_A + R_B \Theta_B) t_i \quad [7-16]$$

From the above equation, the normal (\dot{n}) and tangential (\dot{s}) components of the relative velocities can be expressed as (Tiphavonnukul, 2002-A):

$$\dot{n} = (\dot{x}_{Ai} - \dot{x}_{Bi}) e_i \quad [7-17]$$

$$\dot{s} = (\dot{x}_{Ai} - \dot{x}_{Bi}) t_i - (R_A \Theta_A + R_B \Theta_B) \quad [7-18]$$

The relative velocity principals may be combined with the time to obtain the relative displacement increment, Δn and Δs (Tiphavonnukul, 2002-A):

$$\Delta n = (\dot{n}_i) \Delta t = \{ (\dot{x}_{Ai} - \dot{x}_{Bi}) e_i \} \Delta t \quad [7-19]$$

$$\Delta s = (\dot{s}_i) \Delta t = \{ (\dot{x}_{Ai} - \dot{x}_{Bi}) t_i - (R_A \Theta_A + R_B \Theta_B) \} \Delta t \quad [7-20]$$

Employing the force-displacement law, and the relative displacement increments, the normal and shear forces increments, ΔF_n and ΔF_s , are calculated as (Tiphavonnukul, 2002-A):

$$\Delta F_n = (k_n) \Delta n = k_n \{ (\dot{x}_{Ai} - \dot{x}_{Bi}) e_i \} \Delta t \quad [7-21]$$

$$\Delta F_s = (k_s) \Delta s = k_s \{ (\dot{x}_{Ai} - \dot{x}_{Bi}) t_i - (R_A \Theta_A + R_B \Theta_B) \} \Delta t \quad [7-22]$$

where k_n and k_s represent the normal and shear stiffness, respectively. At each time-step, the force increments of F_n and F_s are estimated by summation of the all force increments from the previous time-steps with ΔF_n and ΔF_s as follows (Tiphavonnukul, 2002-A):

$$(F_n)_N = (F_n)_{N-1} + \Delta F_n ; (F_s)_N = (F_s)_{N-1} + \Delta F_s \quad [7-23]$$

where $t_N - t_{N-1} = \Delta t$ (t refers to time). Figure 7-4 illustrates the condition that normal and shear forces on a particle are opposed to \bar{e} and \bar{t} , which are assumed to be the positive direction (Tiphavonnukul, 2002-A).

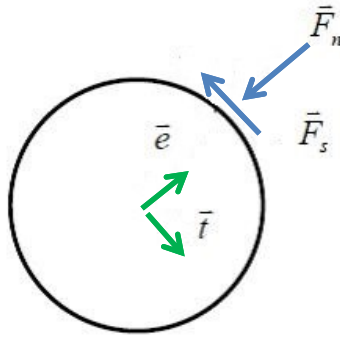


Figure 7-4 Sign convention for F_n and F_s (adapted after Tiphavonnukul, 2002-A)

Finally, with a comparison of the value of shear force F_s from the equation (7-23) and the maximum possible value $(F_s)_{\max}$, the Coulomb friction law may be written as (Tiphavonnukul, 2002-A):

$$(F_s)_{\max} = F_n \tan(\phi) + c \quad [7-24]$$

where c is the cohesion, and ϕ is the inter-particle friction angle. In the case where $(F_s)_{\max}$ is smaller than the absolute value of $(F_s)_N$ from equation (7-23), the value of $(F_s)_{\max}$ will be replaced by the value of $(F_s)_N$ in equation (7-24) (Tiphavonnukul, 2002-A). For each contact of a particle, normal and shear forces are calculated, and then considering all contact forces of particle Z , the resultant force will be obtained. By having the resultant force, $\sum F_{zi}$, the resultant moments, $\sum M_z$, can be estimated from $\sum M_z = \sum F_s R_z$ where $\sum M_z$ is considered negative by acting in clockwise direction (Tiphavonnukul, 2002-A). At the end, the new position of the particle is calculated by having the resultant forces and moments of a particle and employing Newton's second law of motion (Tiphavonnukul, 2002- A).

7-3-4-2- Non-linear contact models

Reported by Dymond (2007), DEM benefits different contact models. The most common and the easiest one is the linear contact model; however, more advanced computers have provided a chance of using more complicated contact models. These non-linear contact models have similar algorithms to linear models, but calculate the normal and shear stress differently; therefore, they may result in more accurate estimations of contact forces (Dymond, 2007).

Two common non-linear available contact models in PFC are the Hertz Contact Model and the Hysteretic Contact Model. The Hertz contact model in PFC is based on an approximation of the theory of Mindlin and Deresiewicz. Unlike the linear contact model that needs a value to be assigned to the stiffness by the user, the Hertz contact model calculates the stiffness through the modulus of elasticity (E) and the radius(R) of the particle (Dymond, 2007). The Hertz model introduces the term “activity distance”. Two particles are active if their activity distance is less than zero (Itasca Consulting Group Inc., 2014-A):

$$\left\{ \begin{array}{l} g_c \leq 0.0 \rightarrow \text{contact active} \\ g_c > 0.0 \rightarrow \text{contact inactive} \end{array} \right\} \quad [7-25]$$

Only active contacts are considered for force-displacement calculations (Itasca Consulting Group Inc., 2014-A). The Hysteretic contact model includes “a combination of the elastic portion of the Hertz model and an alternate dashpot group including three different dashpot modes, consisting in a nonlinear visco-elastic element in the normal direction” (Itasca Consulting Group Inc., 2014-A). The activity criterion is the same as the Hertz model. In the hysteretic model, only force is transferred, not moment, which is common with Hertz model (Itasca Consulting Group Inc., 2014-A). The force is obtained by the summation of a non-linear elastic component F^h , and a viscous component F^d (Itasca Consulting Group Inc., 2014-A):

$$\left\{ \begin{array}{l} \mathbf{F} = \mathbf{F}^h + \mathbf{F}^d \\ \mathbf{M} = \mathbf{0} \end{array} \right\} \quad [7-26]$$

Since the Hertz contact model did not allow particles to be clumped, therefore, it was not employed in this study.

7-3-5- Damping models

Frictional sliding between the components of a system reduces the energy of the system; however, frictional sliding may be insufficient to reach a state of equilibrium for all conditions (Itasca Consulting Group Inc., 2014-A). Local damping and viscous damping are two options to reduce kinetic energy in PFC. Local damping provides a damping force on each particle that has a value comparative to the unbalanced force, while viscous damping provides a damping force with a value comparative to the relative velocity difference between the two particles in contact (Itasca Consulting Group Inc., 2014-A).

When a system needs to rapidly reach to an equilibrium state, as static systems do, local damping works the best (Dymond, 2007). For systems with dynamic behaviour, or systems that particles are free to move in the domain area or have huge impacts, viscous damping suits the best (Itasca Consulting Group Inc., 2014-A).

7-3-6- Balls and Clumps

There are two elements in PFC to simulate granular material: balls and clumps. In PFC2D, a ball is a stiff circle with unit thickness, while in PFC3D, a ball refers to a sphere (Itasca Consulting Group Inc., 2014-A). A clump is a combination of two or more balls that remains rigid under all conditions (Itasca Consulting Group Inc., 2014-A).

As mentioned before, balls are usually used to simulate the granular materials. However, most particles in nature do not have a smooth and circular shape like a sphere (Dymond, 2007). Consequently, an assembly of such particles has a very low friction coefficient in comparison to the natural angular crushed material (Coetzee, 2010). To overcome this problem, PFC offers the use of clumps to generate more angular particles. The balls arranged as a clump do not move relative to each other, and can have any amount of overlaps. These balls cannot be separated during a simulation, and contact forces do not exist between them (Coetzee, 2010).

7-3-7- Boundary Conditions

Generally, a particle does not have any limitation in moving around, unless it touches the boundary conditions (Tiphavonnukul, 2002-A). Boundaries act like other elements in a system when a particle contacts them. Thus particles are not allowed to pass them, but they can move or slide along them, resulting in generation of a frictional force, and therefore loss of energy in the system (Tiphavonnukul, 2002-A). The slippage along the boundary happens when the maximum possible value of the shear force is smaller than the tangential force of the particle (Tiphavonnukul, 2002-A). In this study, boundary conditions refer to the sidewall and bottom wall of the bin, and also to the dipper walls.

Chapter 8

Numerical simulation of filling a cable shovel dipper

A 2D numerical simulation was performed to model the behaviour of angular cohesion-less granules through loading cycle of a cable shovel, using PFC version 5.0 developed by Itasca. The study was motivated by a desire to understand the loading procedure better, and to understand the importance of particle size, shape, and dipper's teeth on the application.

A code was written in Fish language (default programming language in PFC) to determine whether the modern DEM method can be used to accurately model the filling procedure of a cable shovel dipper. To verify the accuracy of the model in predicting the experimental results, the model was simulated based on the properties of the examined material (crushed limestone). The obtained results were then compared against experimentally measured results. Afterwards, a series of models was developed to investigate the influence of particle shapes, particle sizes, and the role of dipper tooth on the material behaviour.

The first drafts of the main model were developed both in the lab and full scales. Since no difference regarding to the number of elements in the system, the total processing time, and the simulated particles behaviour were observed, it was decided unlike the lab experiments, the simulations were modeled in full size scale. Thus, there was no need to extrapolate the numerical results to the full size scale.

8-1- Determination of material properties

DEM simulation method uses micro-properties of material rather than macro-properties. For material with the simple packing arrangement, micro-properties can be predicted from its macro-properties. However, it has been always difficult to determine granular material properties, which usually have arbitrary particle orientations. Therefore, to assign an appropriate micro-properties value for this type of material, calibration methods are required. Following is the list of material properties to define cohesion-less granules in PFC (Majidi, 2012, Coetzee 2010 and Dymond, 2007):

- Density

- Shape of particles
- Size and size distribution of particles
- Normal and shear stiffness
- Friction coefficient
- Damping

Apparent density of material is usually known and can be used as the density of the particles in PFC modeling (Itasca Consulting Group Inc., 2014-B). The procedure of determining the other parameters will be described here.

8-1-1- Particle shape

In DEM modeling, particles are created by discs (in 2D) or spheres (in 3D). Such particles cannot reproduce the behaviour of natural materials due to the over-idealisation. However, DEM is capable of modeling particles with non-circular (or non-spherical) shapes by creating clumps that are a combination of two or more balls (spheres) (Itasca Consulting Group Inc., 2014-A).

To determine the shape of material used in the experimental set up, a random sample of 250 particles was taken from the material used for the experimental test. These particles were classified into three groups based on their overall shape. After that, three particles using clumps were created in PFC, each representing one of the classified shapes. These particles were kept as simple as possible to minimize the total possessing time. Figure 8-1 illustrates the created shapes with their frequency. Since one of the focuses of this study was to investigate the influence of shape of particles (angularity) on crushed material, two additional shapes were generated representing a material with low to moderate angularity and a material with moderate to high angularity (Figure 8-2).

8-1-2- Particle size and size distribution

The result of the digital image processing system (Chapter 3) was used as the size distribution of simulated particles. To simulate the numerical model in the full scale, the scale factor of the experimental set up (1:32) was used to calculate the size of the simulated particles. To produce the size distribution of the material in PFC, a code was written to model the result of the digital image

processing system. As shown in Figure 8-3, the simulated size distribution completely matches the result of the size distribution analysis.

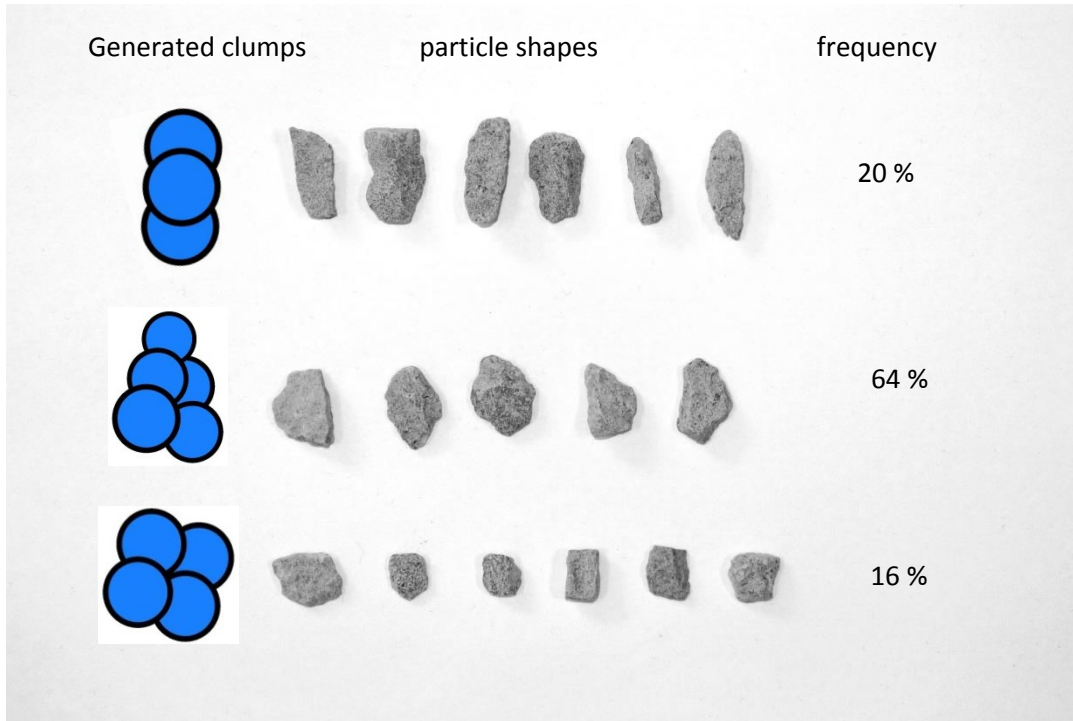


Figure 8-1 Simplified particle shapes used in PFC modeling

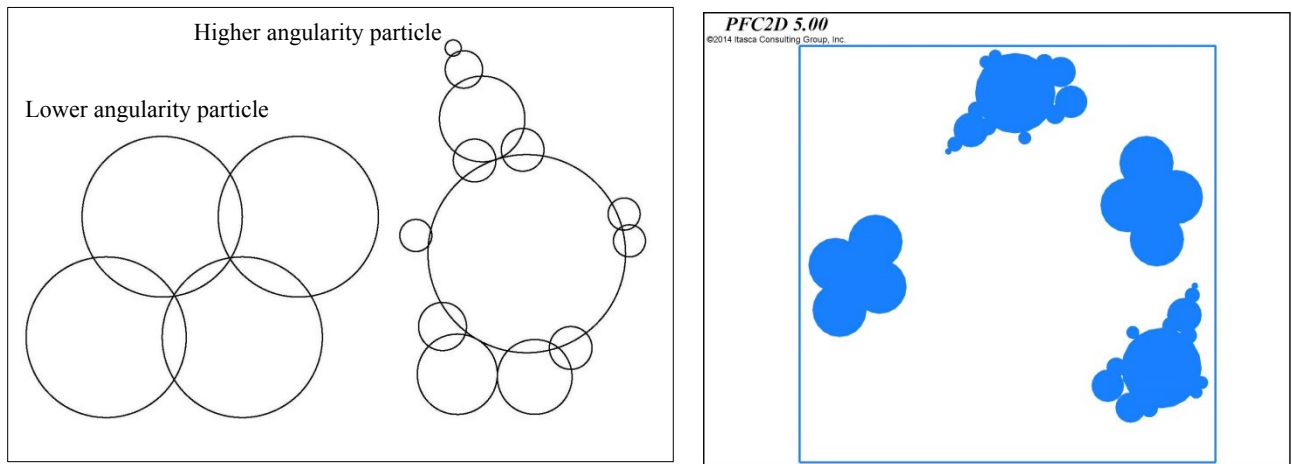


Figure 8-2 Created angular particles used in PFC modeling

Generating a rockpile with such a wide size distribution diversely affected the processing time of the model due to increasing the number of clumps in the system and limiting the number of runs with this system. For this reason, uniform size distribution was used with three different particle sizes for investigating the influence of particle size and shape, as well as of dipper tooth. These sizes included the mean and maximum size particles plus a size in between (corresponding to bins 12, 18, and 15 from the digital image processing analysis, respectively). Table 8-1 shows the detail of these sizes.

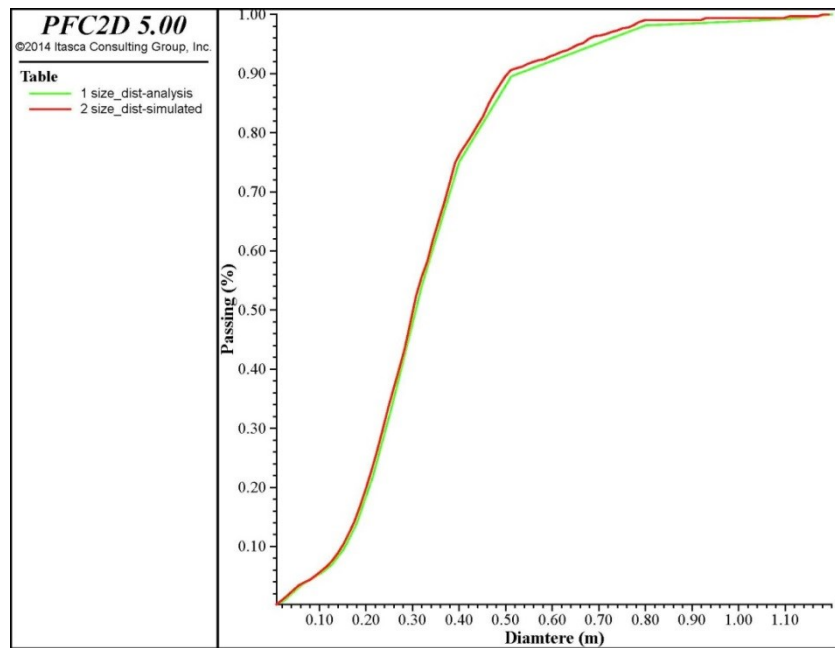


Figure 8-3 Size distribution of examined material vs size distribution of simulated material in PFC

Table 8-1 Different particle sizes used in PFC simulation

Particle size name	Relative bin #	Real size in experimental test (mm)	Scale factor	Scaled size used in simulation (m)
small	12	10	32	0.32
medium	15	25	32	0.8
large	18	37.5	32	1.2

8-1-3- Stiffness

A lower stiffness results in a smaller time step. However, a very small magnitude of stiffness causes unrealistic overlaps between the balls/clumps, and also between the balls/clumps and walls. On the other hand, a high stiffness results in unrealistic behaviours such as exploding in the domain area due to the high forces generated between two particles in contact (Majidi, 2012). In order to estimate an appropriate stiffness that can be assigned to the particles for realistic packing, a simulation was designed. The idea of this simulation was taken from Majidi (2012).

A simple packing simulation was modeled where particles fall into a container due to the gravity force and settle to reach the equilibrium state. It was assumed that normal and shear stiffness were equal. There were eight containers filled with particles with the same characteristics but different stiffnesses. The model was run for two different particle shapes and size distributions. The first model was based on the shape and size distribution of the material used in the experimental set up. The examined clump shape was the one that had the maximum frequency among the others (Figure 8-4, a). In the second model (Figure 8-4, b), the designed clump used was the representative of a low to moderate angular particle with uniform size distribution (Table 8-1, mean particle size).

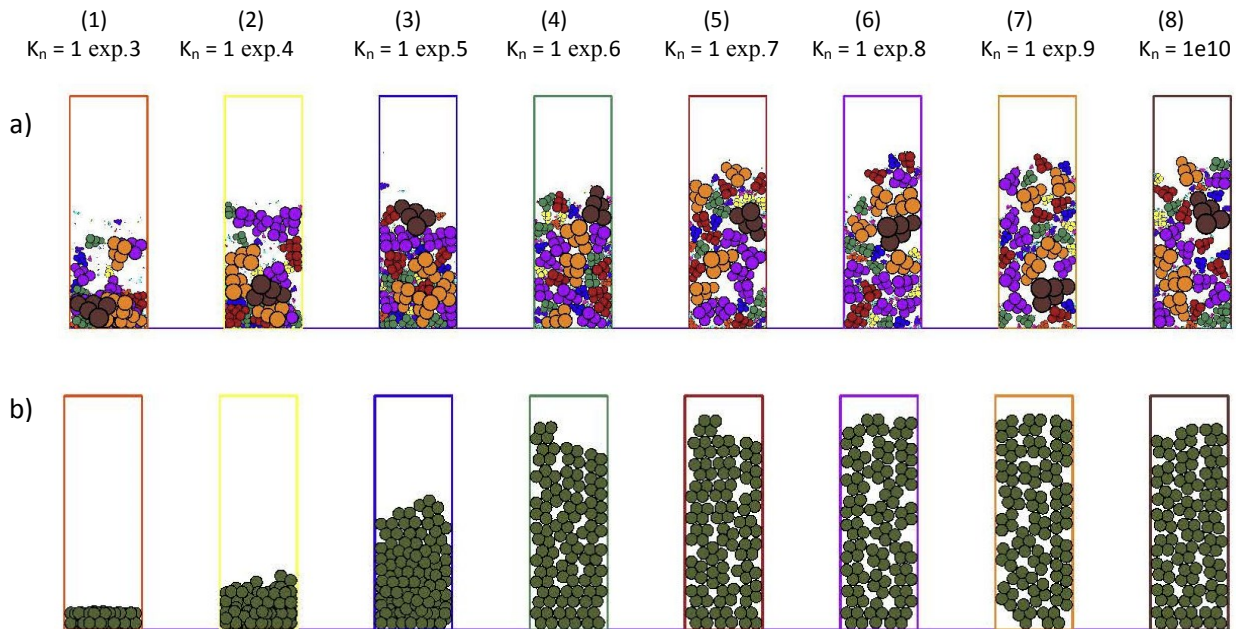


Figure 8-4 Particle packing with different stiffness

As can be seen, two simulations displayed the same results. The first container, which had the lowest particle stiffness, showed enormous overlaps. By increasing the stiffness from the most left container to the rightmost container, it was observed that the height of particles in the container was increased. As mentioned before, all material properties were same, except the stiffness. Therefore, increasing the stiffness resulted in decreasing the particle overlaps and created a higher height of particles in the container. Also, it was observed that changing the stiffness from 1×10^7 to 1×10^{10} (Figure 8-4, 4 to 8), had no significant change in the height of the particles in the containers. According to Majidi (2012), in this case, particles had made a compact assembly with minimum overlaps. To reduce the time step, the minimum acceptable value of stiffness, which was $k_n = k_s = 1 \times 10^7$, was chosen.

8-1-4- Friction coefficient

Friction coefficient of material is one of the critical parameters in the numerical modeling through PFC. Since the angle of repose is a good estimate for the friction coefficient of granular material (Blouin et al., 2001), the angle of repose test is an acceptable method to determine this characteristic of the material.

In the present study, the angle of repose test was used to calibrate the friction coefficient of the simulated material. The limestone particles used for the experimental tests fell down through a funnel and set on a horizontal surface (Figure 8-5). The angle between the created pile and ground was measured as the angle of repose of material. A number of tests were performed and the average of recorded angle of repose was calculated. Then the angle of repose test was simulated through DEM modeling using PFC2D. Different friction coefficients were examined and the results were compared to the results of the experiment. The value that showed the best match between the simulation and the experiment was selected to use in the simulation of granular material flow into a cable shovel dipper (Figure 8-6).



Figure 8-5 Pile of limestone particles in angle of repose test

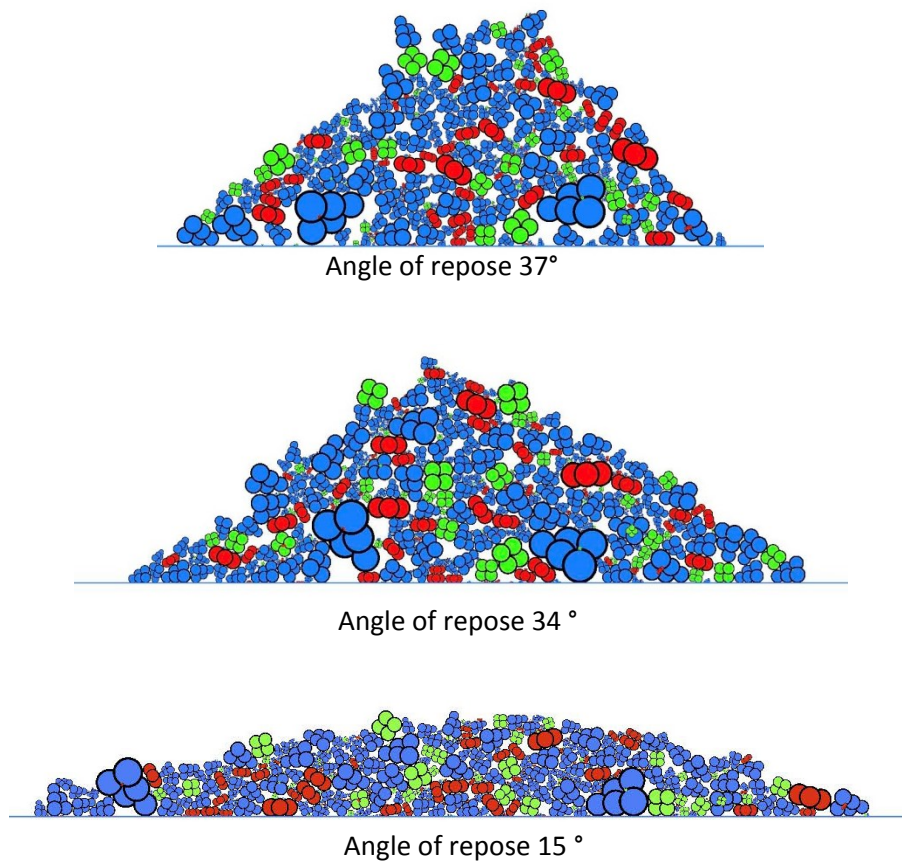


Figure 8-6 Pile of particles in simulated angle of repose test

8-1-5- Damping

Damping is a material property that does not have a specific calibration method (Dymond, 2007). In the current study, a set of runs was conducted to test different damping coefficients. A

comparison of the results implied that a high value for both local and viscose damping was better to use. Viscose damping was a good option for systems involving free flight particles, as in the present study. However, since the modeled particles were forced to dump from a specific height on an inclined surface, they had a huge kinetic energy at the time of collision with the ground, leading to vast movements and longer processing time to reach to the equilibrium state, and therefore, at the end, resulting in a lower rockpile slope. It was necessary to absorb this undesired energy by employing the local damping coefficient even if it was not designed for such a situation and might have adverse consequences.

PFC was basically composed to take care of static systems; consequently, it has weaknesses in the calibration of dynamic models (Dymond, 2007).

8-2- Reducing the processing time

Discrete element models usually require a great deal of computer power and a quick processor (Parker, 2009). At the beginning of this study, it was believed that the current available computer systems were powerful enough to run the designed models. However, very long simulation times revealed that it was necessary to employ appropriate approaches to shorten the total processing times. In PFC, two parameters control the simulation time: time step and cycle time. However, increasing the time step and/or reducing the cycle time shorten the processing time; employing each of them may have inverse consequences (Dymond, 2007).

8-2-1- Decreasing cycle time

In DEM, cycle time is the required time to run one cycle (Dymond, 2007). The possible ways to shorten the process duration, which is principally a function of the simulation setup and parameters, are as follows (Dymond, 2007):

- To reduce the quantity of objects in the system, including balls, clumps, and walls
- To reduce the time taken to upgrade the particles

Although the most efficient way is to decrease the quantity of objects in a model, such a strategy may cause some undesirable impacts to be considered (Dymond, 2007).

The number of calculations performed per cycle was reduced by reducing the number of particles and walls in the system. For this purpose, the dippers (with/without tooth) were modeled as simple as possible (Figure 8-7), and complicated clump shapes and combination of different shapes were avoided.

Moreover, generating a rockpile with a wide size distribution of material, diversely affected the processing time of the model due to increasing the number of clumps in the system and limiting the number of runs with this system. For this reason, to create the rockpile in DEM modeling, instead of filling the whole rockpile with clumps, they were restricted to be created in a layer as the surface of the rockpile (Figure 8-8). The slope of this layer was determined from the result of the angle of repose calibration test. This method dramatically reduced the number of clumps, and therefore the processing time.

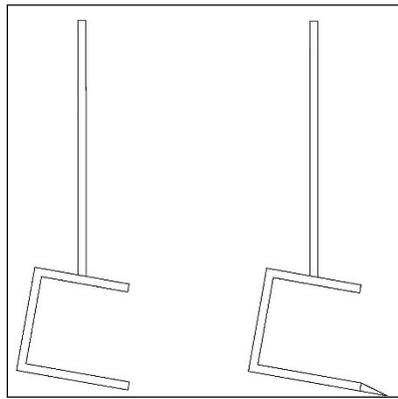


Figure 8-7 Designed dippers for PFC modeling

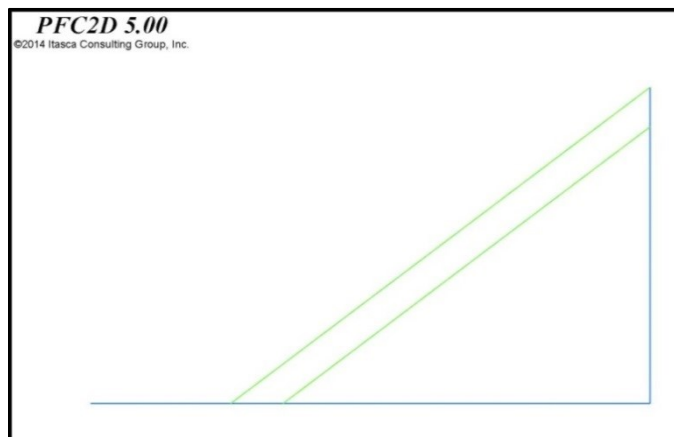


Figure 8-8 Limiting the clumps to be created in a layer at the surface of the rockpile

8-2-2- Increasing time step

Another method that is used to reduce the processing time is to increase the time step (Dymond, 2007). In the linear contact model, the time step is dependent on the particle stiffness, density, and size (Dymond, 2007). To determine an appropriate stiffness, a calibration model explained earlier (section 8-1-3) was employed.

8-3- DEM simulation of cable shovel dipper filling

A 2D numerical model was generated to simulate the filling procedure of a cable shovel dipper, using PFC version 5.0 developed by Itasca. The size of elements in the numerical model was scaled into the full size, using the experimental scale factor of 32; other properties were kept the same. As mentioned earlier, due to the time and computer power limitations, an alternative method was used to create the rockpile to decrease the number of particles in the system.

After creating the particles in the boundary as the surface of the rockpile, they were allowed to reach to the equilibrium state. Then, the upper wall of the boundary was removed and the system again reached to the equilibrium state. Afterwards, a dipper was created using walls and added to the system at the toe of the created rockpile. The dipper was then dragged through the particles, via assigning a rotational speed to the dipper walls. The behaviour of the particles and the loading mechanism were recorded through a number of runs.

The results indicated that, regarding the filling procedure, there was an agreement between the DEM and the lab experiment. The DEM model successfully predicted the trends seen in the experimental set up. Different steps of the flow mechanism and the layers of flowing particles were identified in the numerical simulation. However, it was seen that the numerical model had some weaknesses in reproducing the experimental simulation.

Figure 8-9 compares the results of the DEM model versus the experimental set up. Particles were colored based on their shapes in the DEM model. Figure 8-9-a indicates the initial stage of the digging, when the dipper engages the rockpile. The DEM model accurately simulated this part. Figure 8-9-b shows the time when the flowing material reaches to the rear of the dipper. Although

the height of material at the dipper ingress is the same, the slope of particles inside the dipper is lower in the simulated model. By continuing the digging, the dipper creates a wedge of particles in front of the dipper. The thickness of material inside and in front of the dipper increases together, but the slope of these small piles is noticeably lower in the numerical model. This lower slope results in a very smaller empty space at the rear of the simulated dipper (Figure 8-9-c&d). In the experiment, a considerable space at the back corner of the dipper remains empty while the dipper ingress is blocked via material in front of the dipper, but the size of this space becomes tiny in the DEM model (Figure 8-9-e). At the end of the filling, when the dipper is detached from the rockpile, the dipper payload in the DEM seems higher than the experiment and the empty space is almost diminished (Figure 8-9-f).

Comparing the results indicates that although simulated material showed the same flow pattern as the real examined material, it hardly resisted the digging via the dipper. Simulated particles moved past one another with little resistance and did not behave as angular rough particles. The ease of movement resulted in a flat pile of material inside and in front of the dipper and a smooth flow of particles, which filled the empty space at the rear of the dipper. Possible reasons for the less accurate results of the model were the assumptions made in the creation of the numerical model. Here are some possible causes for these behaviours:

Roughness of particles: As the surface roughness increases, the value of the inter-particle friction coefficient increases, leading to reduced rolling ability and increased interlocking. Smooth particles can move past one another via sliding and rotation with little resistance. One of the difficulties in the current model was to create rough particles. This could be done by creating more complicated clumps to mimic a rough surface particle. Due to computer limitations, the only option was to generate clumps as simple as possible.

Friction coefficient: A low particle friction coefficient would result in the particles moving too easily over one another and would allow the dipper to penetrate deeper into the material. The inter-particle friction coefficient defines how difficult it is for the particles to move over one another. This factor was introduced via the friction coefficient in PFC modelling which was determined from the angle of repose calibration test. However, higher friction coefficients were examined; increasing the friction coefficient had no significant influence on the results. The author believes

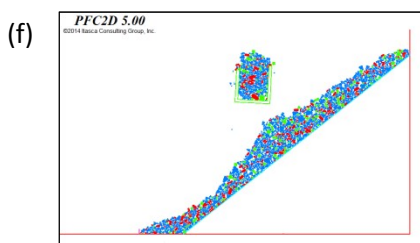
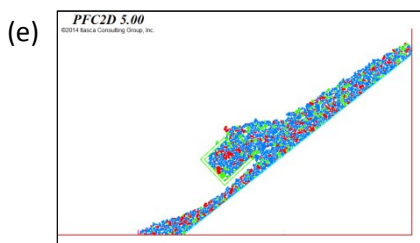
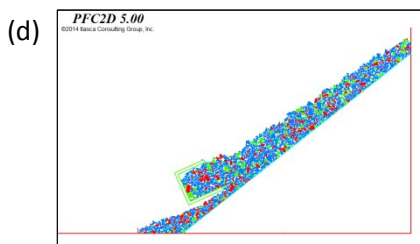
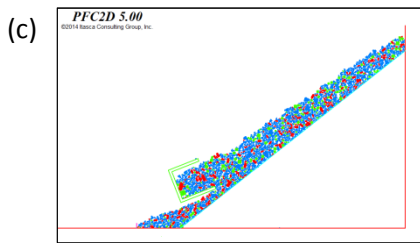
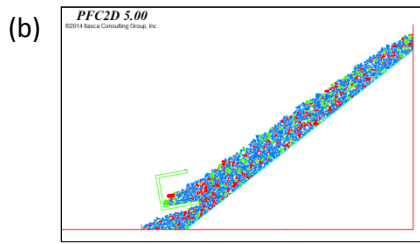
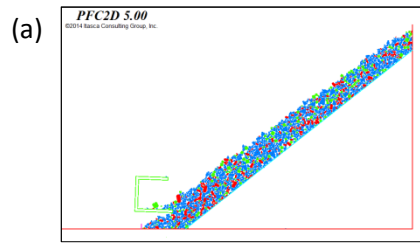


Figure 8-9 Dipper filling procedure, DEM vs experimental set up

that, in this case, the impact of the particle's shape was more significant in reducing the inter-particle friction coefficient than the value of friction coefficient in the model was in such reduction.

Digging mechanism: The modeled dipper digging mechanism also affected the behaviour of material. In the numerical simulation, the dipper had no degree of freedom and was forced to follow the dig trajectory with a fixed velocity. This digging mechanism could have led to the increased drag force that could effortlessly overcome the resistance force of particles and was observed as an easy digging condition.

Contact and damping models: PFC was basically composed to take care of static systems; for instance, the linear contact and local damping models, and calibration methods were designed for static systems (Dymond, 2007). Therefore, employing these methods in dynamic models may have inverse consequences (Dymond, 2007). As mentioned earlier, different damping values were examined and the ones with which the models worked the best were selected. However, the selected values might not be the best choices.

Compaction: The method was used to create an assembly of material as a rockpile, resulted in a low degree of material compaction, and therefore a decreased particle interlocking and frictional resistance. One of the difficulties in this study was to create a compact assembly, to be a better representative of a real pile.

8-3-1- Investigating the generation of the void space inside the dipper

One of the main differences of the current numerical model and the experimental set up was in generating the void space at the rear of the dipper. Due to the importance of generation this empty space, more simulations were performed to investigate the capability of DEM to model this phenomenon.

As mentioned earlier, the main reasons for the different behaviour were the low friction coefficient and roughness of simulated particles that resulted in a smooth flow of material inside the dipper. In order to minimize the easy flow of material, an alternative solution was employed. Previous research showed that in an assembly consisting of fine and coarse particles, the particle resistance to move one over another is reduced due to the lubrication influence of fine particles (Singh et al., 1992, 2006-A and 2006-B). This influence encourages the dipper to penetrate deeper into the

material, thereby resulting in a higher fill factor (Singh et al., 1992, 2006-A and 2006-B). In a new set of simulations, to reduce the influence of fine particles, uniform size distribution was replaced with the wide range of examined size distribution of material.

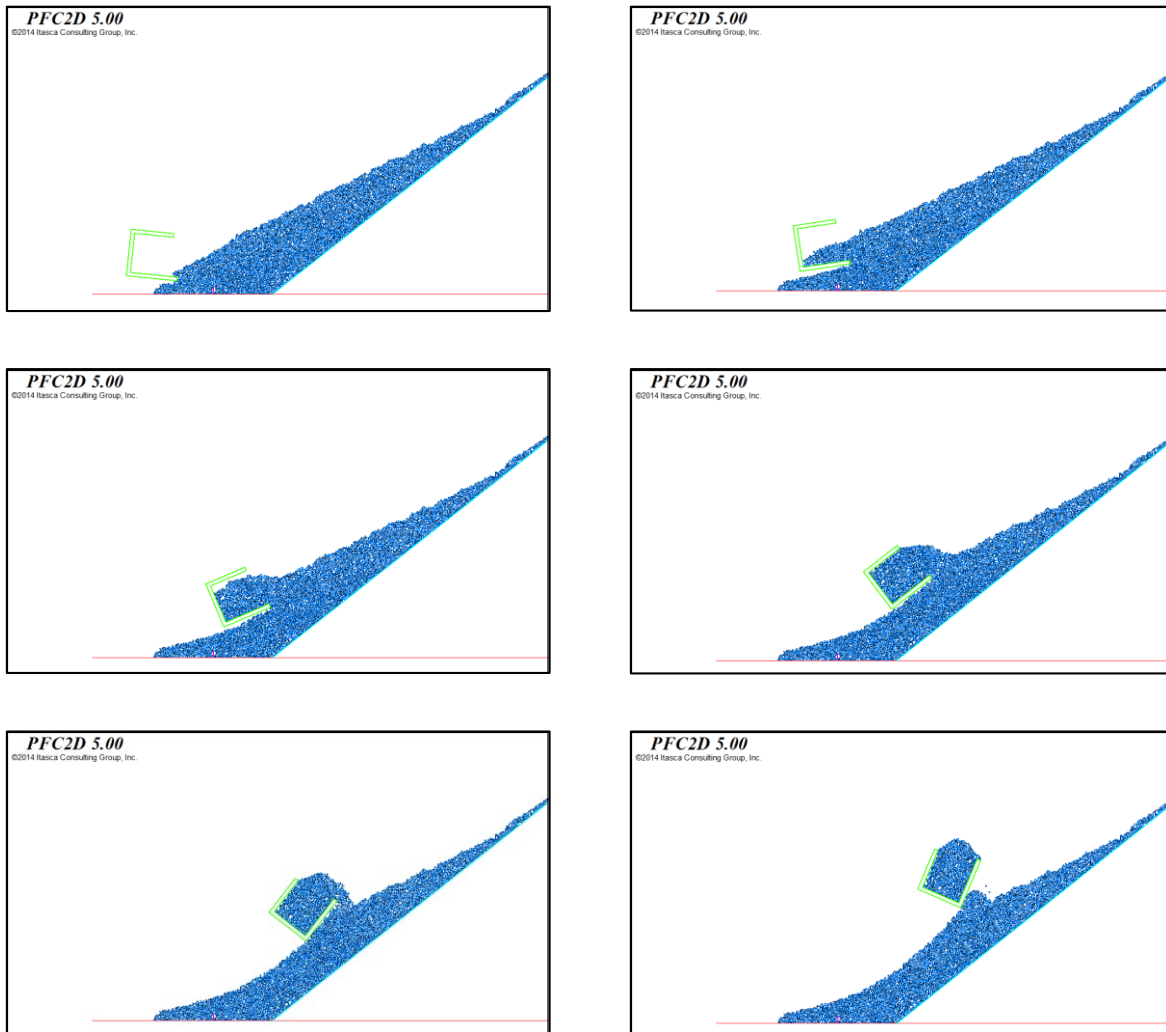


Figure 8-10 Simulated dig cycle with small size particles and uniform size distribution

A different number of simulations were performed with different particle sizes. Other properties were kept constant. The following figures illustrate the results of the simulations with particle sizes of 0.152 m, 0.32 m, and 0.8 m, respectively, which represent small, medium, and large particle sizes (Table 8-1). As can be seen, Figure 8-10, which has small particle sizes, illustrates a smooth flow of material the same as the main model with the wide size distribution. A smooth slope of

material piles inside and in front of the dipper, indicating a low angle of repose of material that is a function of insufficient inter-particle friction coefficient. Thus, particles show little digging resistance due to a low friction coefficient. Under such an easy digging condition, there is less possibility to generate the void space inside the dipper. Less void space results in a higher amount of payload inside the dipper. In Figure 8-11 and Figure 8-12, the increasing of the particle sizes, common with the results of the experimental set up, show the empty space generated during the dig cycle. Also, the void space remains at its initial location while the ingress of the dipper is blocked.

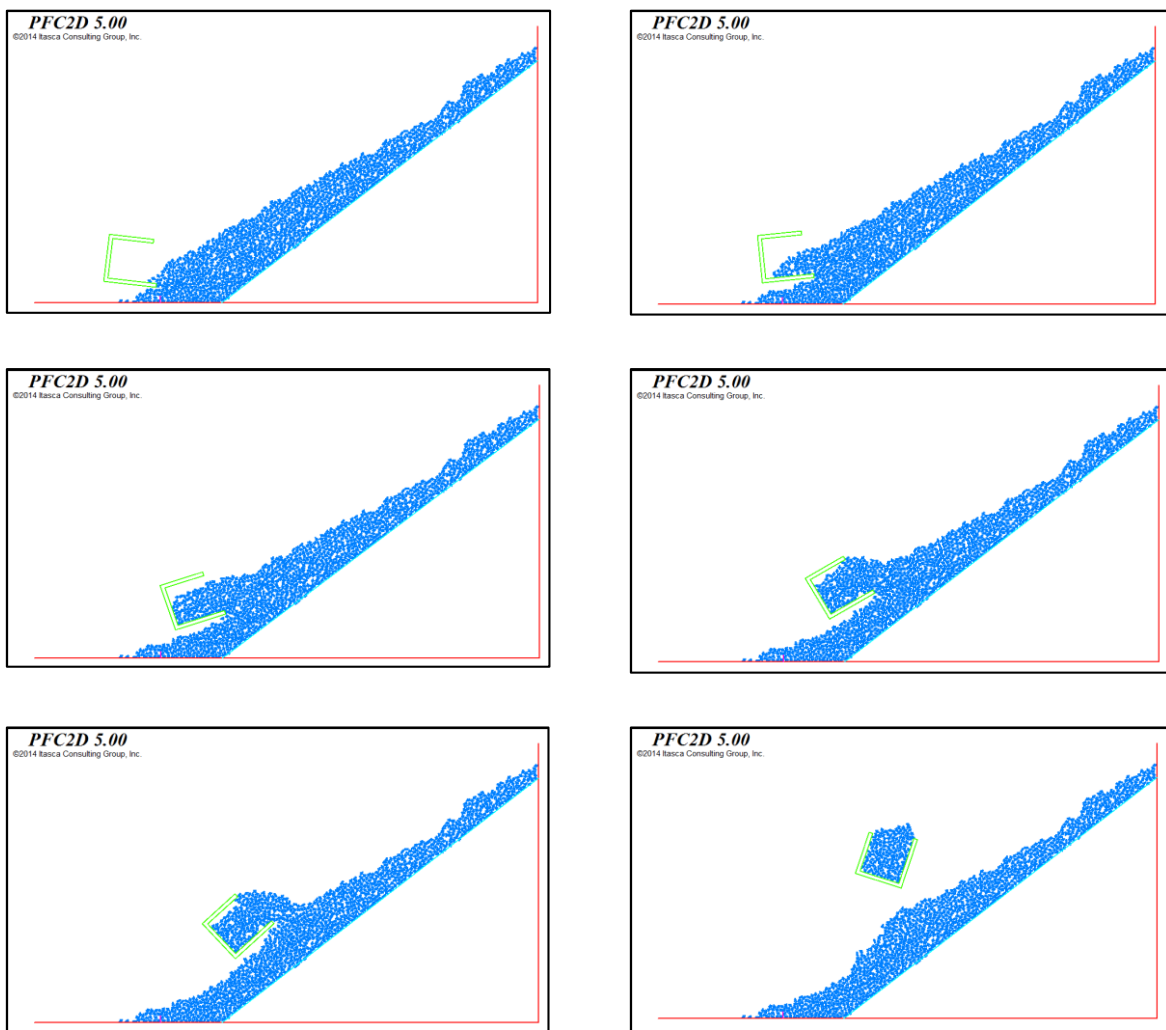


Figure 8-11 Simulated dig cycle with medium size particles and uniform size distribution

In Figure 8-11, changing the dipper orientation at the end of the dig cycle causes some particles from the “flow zone” to drop towards the rear of the dipper, resulting in transition the void space

to its final location. In Figure 8-12, which shows very large particle sizes, even by changing the dipper orientation, material cannot flow towards the rear of the dipper due to huge interlocking, so the void space can be seen up to the end of the dig cycle. This is common with what is expected in reality with the same particle sizes. Modifying the properties of the simulated particles in the DEM model, they were more representative of the real material, produced the same results as the experimental set up.

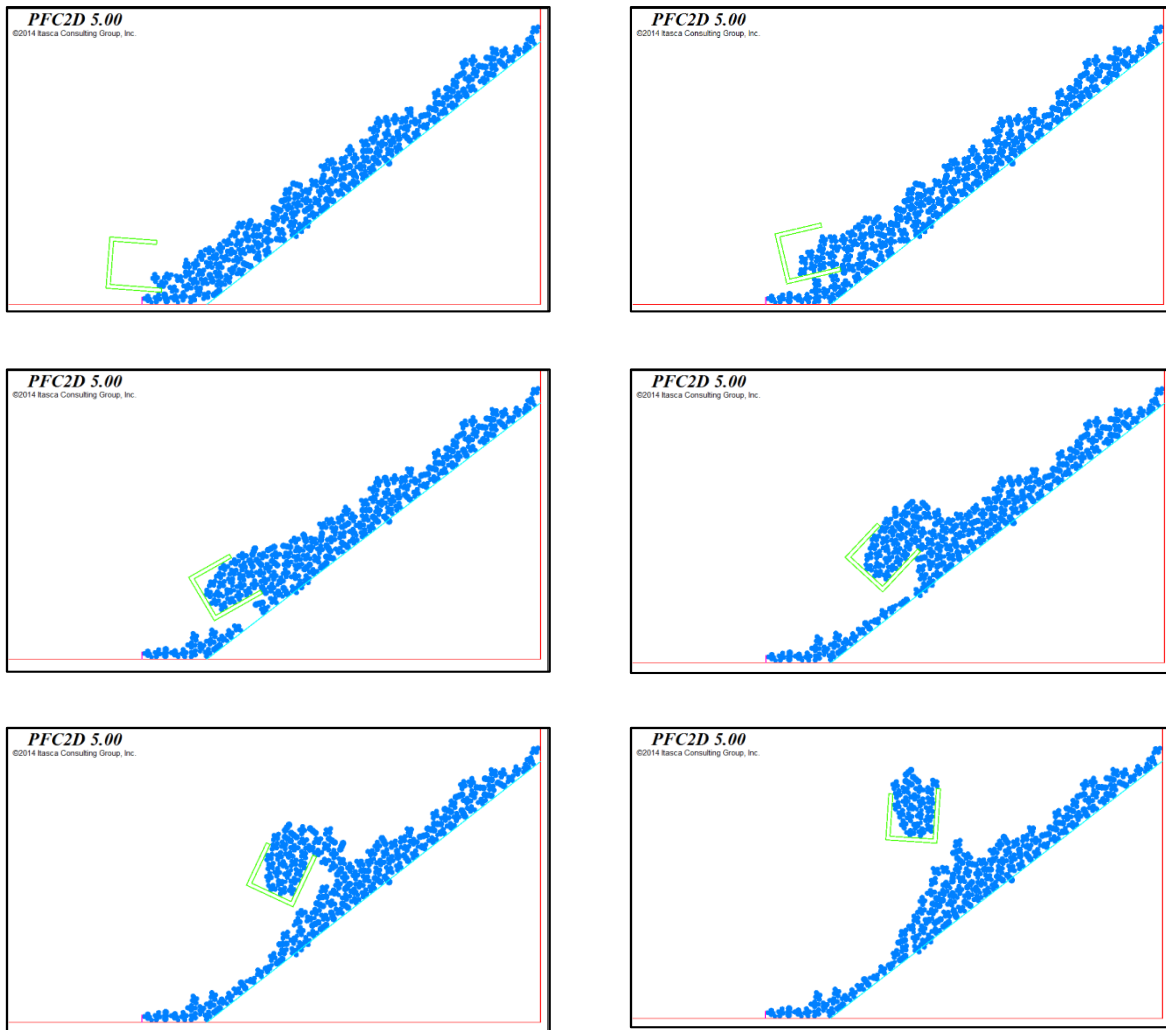


Figure 8-12 Simulated dig cycle with large size particles and uniform size distribution

It should be noted that generally the available time to complete a project is limited; therefore, sometimes it is unfeasible to design a model that works exactly the same as the real system. Consequently, a numerical model is satisfactory that could imitate the physical model and could be verified by deciding a level of accuracy through experimental results (Dymond, 2007). The current DEM model showed that although the simulated material properties were inaccurate, the model was able to predict the general flow pattern correctly. With more realistic contact models and better computer facilities, it is highly probable that numerical models will be capable of simulating the cable shovel dipper filling more accurately. Further study is, therefore, justified.

8-4- Investigating the influence of material properties and dipper tooth on cable shovel dipper filling via DEM modeling

The performed experimental and numerical investigations elucidated that there is a general flow pattern for granular particles loading into a cable shovel dipper. However, some dig conditions and material properties may influence the filling procedure, and therefore the productivity of the machine. Since the simulated DEM model was capable of predicting filling procedure, by modifying the main numerical model explained in the previous section, it was used to perform more investigations to achieve a better understanding of the material behaviour during a dig cycle of a cable shovel dipper.

The main alterations were the method of creating the rockpile, to have a more stable rockpile before initiating digging, and employing a uniform size distribution to limit the number of particles in the system and shorten the processing time. Also, new shapes of clumps were used to simulate low and high angular particles (Figure 8-2). The simulation consisted of two perpendicular base walls and a hopper created using walls (Figure 8-13). The hopper then was filled with clumps to simulate the granular material. Once the clumps had settled, the bottom door of the hopper was opened to let the particles dump. At this stage, the particles were allowed to settle again and to create a rockpile. After that, a dipper was created using walls and added to the system at the toe of the created rockpile. The dipper was then dragged through the particles via assigning a rotational speed to the dipper walls. The behaviour of the particles and the loading mechanism were recorded.

Three particle sizes, two particle shapes, and two dippers (with/without tooth) were analysed to investigate their influence on the material behaviour. The results will be presented here.

Since the created particles in these models did not represent a specific material in reality, as long as their properties could represent an angular crushed material, they met the purpose of the study. All material properties used were the same as the main model, except the particles' shape and size distribution. It should be noted that these models had the same weaknesses as the main model, except the more stable rockpile, but challenges regarding the low digging resistance remained. Also, creating a rockpile with uniform particle size through damping material from a high height resulted in a high void ratio and very loose assembly of material that enhanced the easy dig condition.

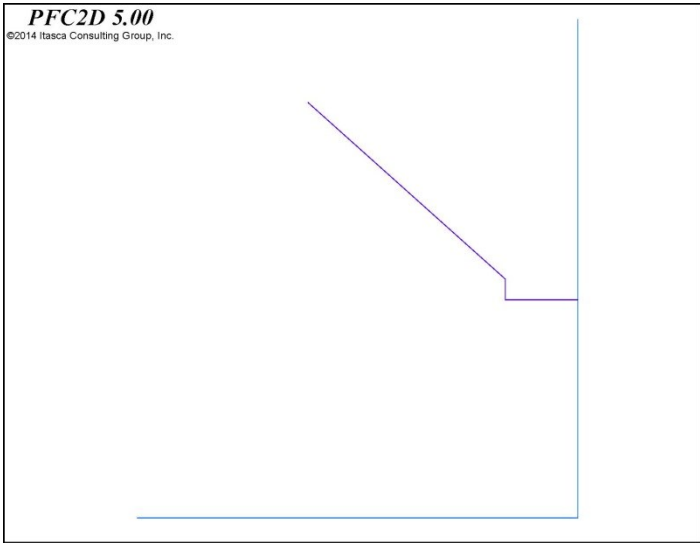


Figure 8-13 Created walls at PFC

8-4-1- Influence of particle size on flow mechanism

Three rock-piles were created using clumps representing low to moderate angularity (Figure 8-3), with three different particle sizes as mentioned in Table 8-1 and a uniform size distribution. Then, a simple simulated dipper dragged through the particles and the flow pattern was recorded. For each particle size, the dig action was repeated through a number of runs. Figure 8-14 to Figure 8-16 illustrate a few snapshots of a dig cycle for each particle size. Particles were colored based on their velocities.

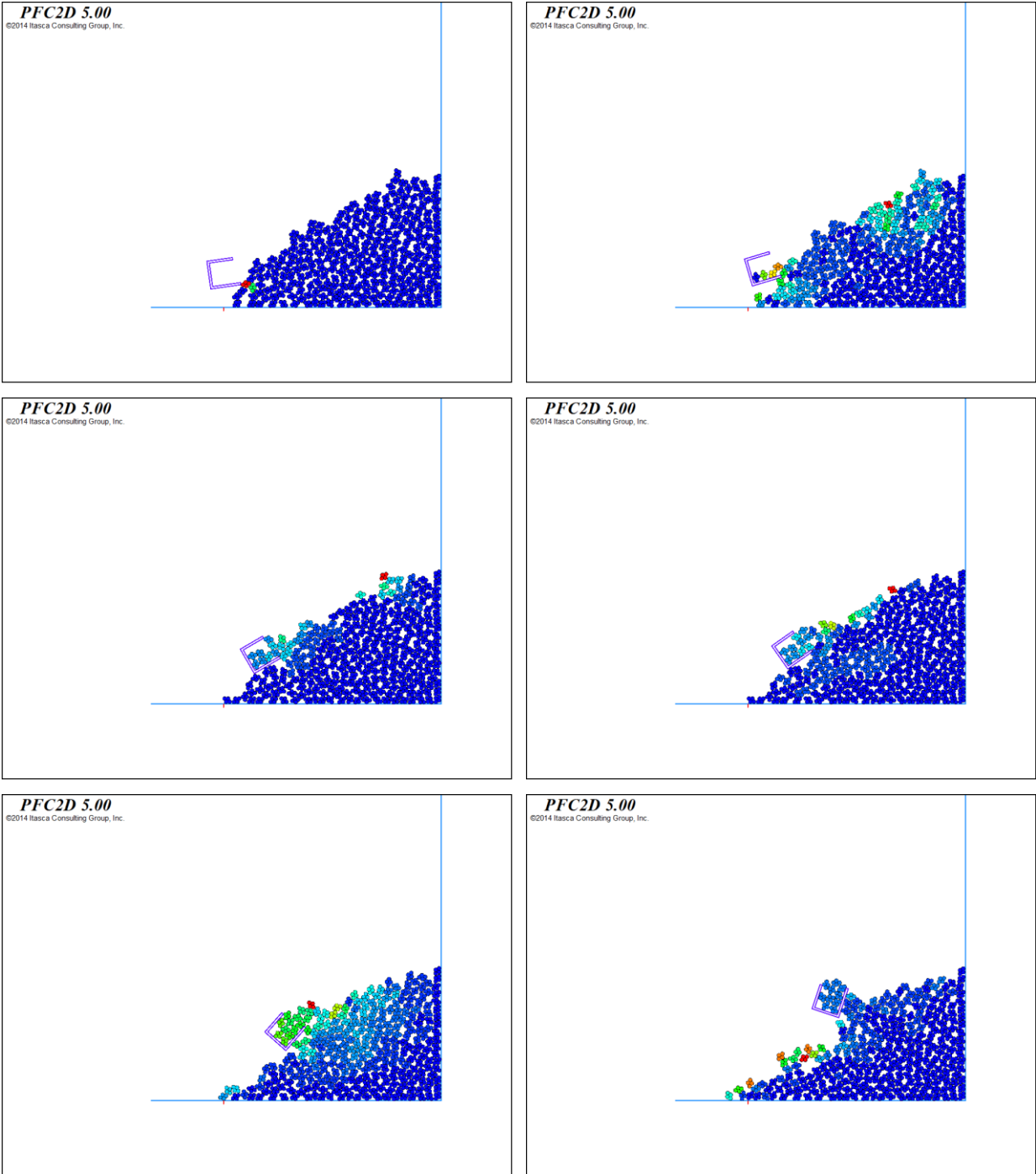


Figure 8-14 Snapshots of a dig cycle with large particle sizes

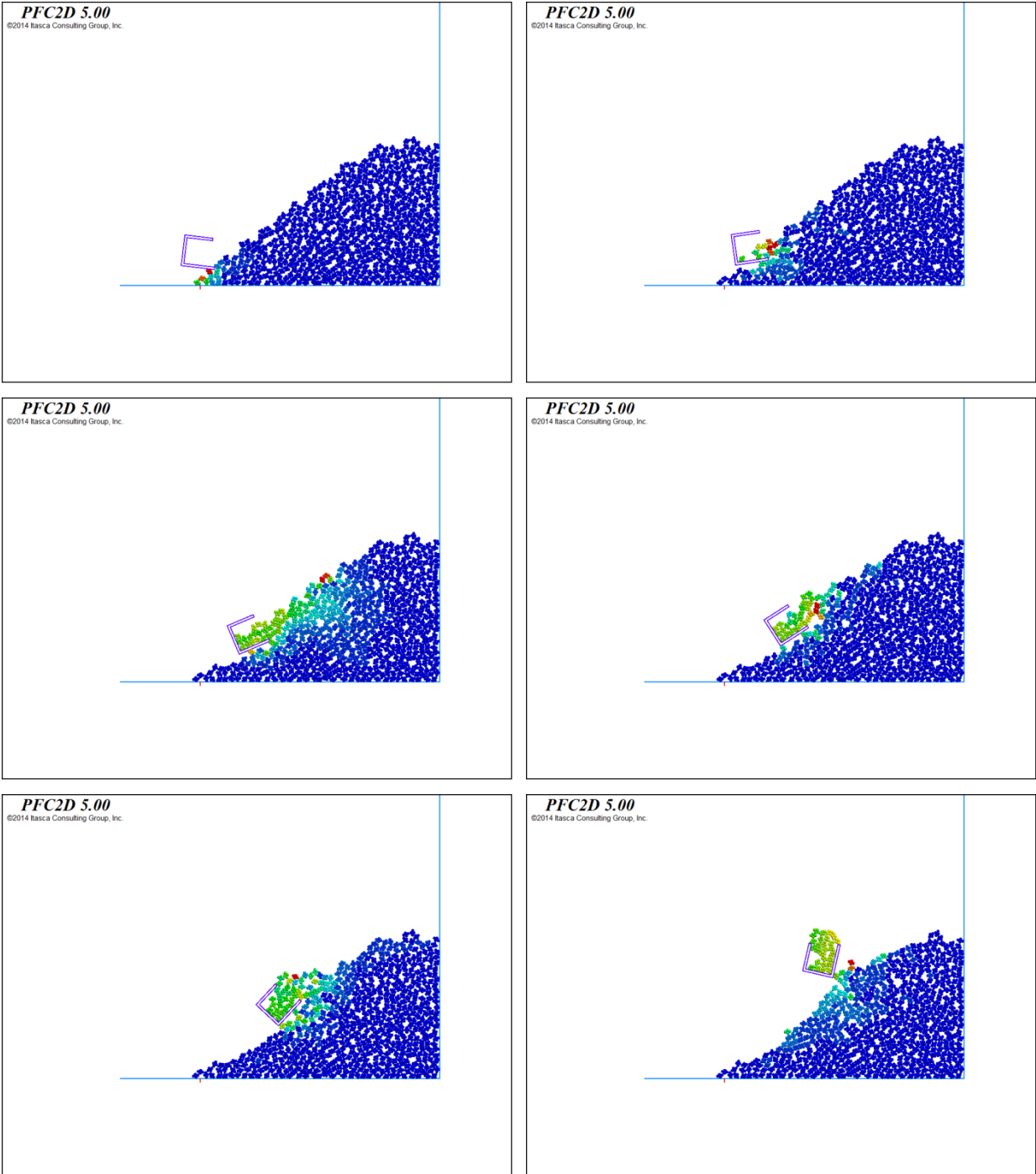


Figure 8-15 Snapshots of a dig cycle with medium particle sizes

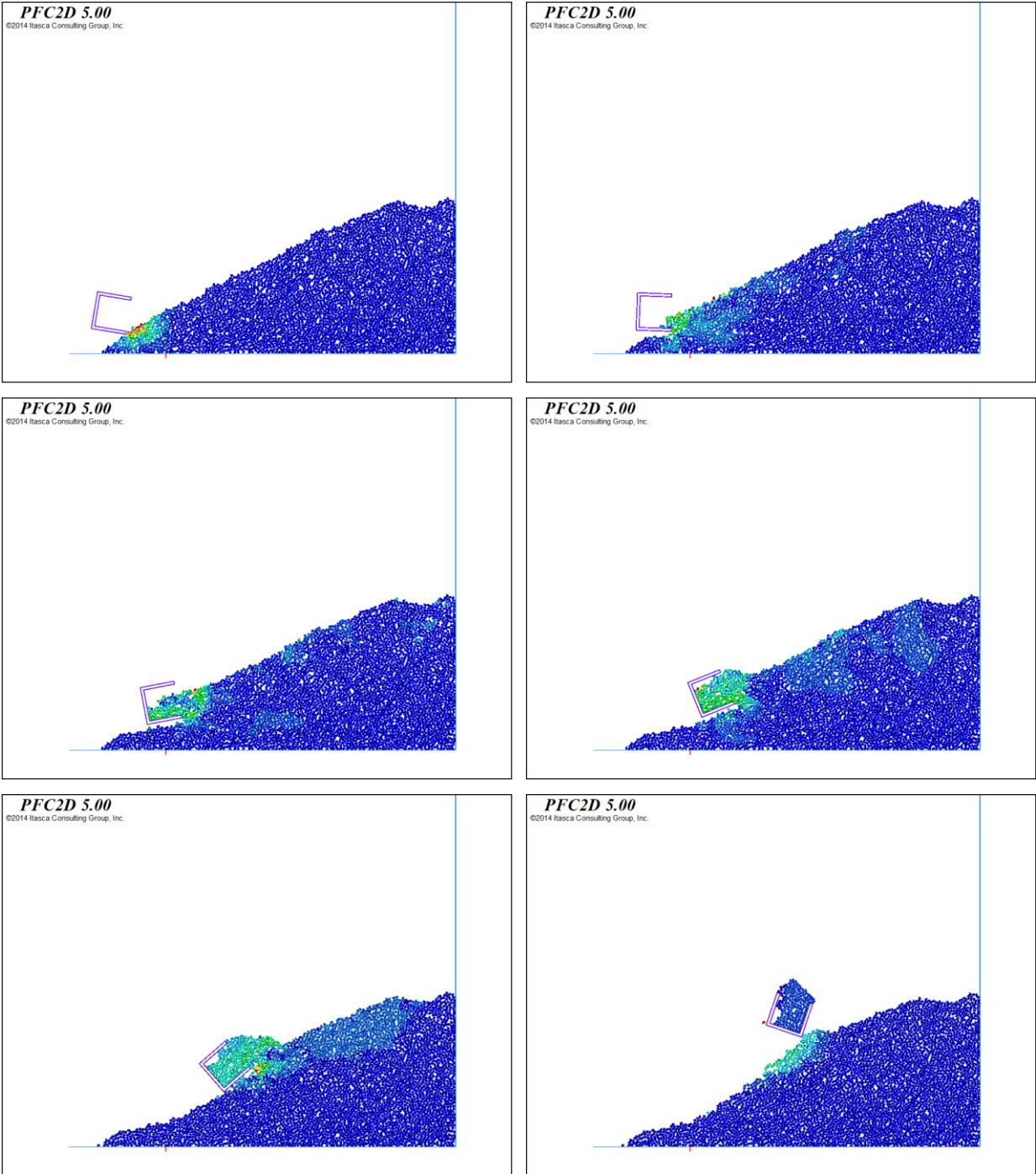


Figure 8-16 Snapshots of a dig cycle with small particle sizes

As expected, the general flow pattern was the same for the examined sizes, but the size of particles impacted the efficiency of the digging. It was observed that increasing the particle size increased the slope of the rockpile. Since the rock-piles were created through dumping material, the final slope of the rockpile would be approximately equal to the angle of repose of the material. As reported by many authors (Van Burkalow, 1945; Fowler and Chodziesner, 1959; Miller and Byrne, 1966; Chen and Cotton, 1988; Froehlich, 2011), the angle of repose increases by increasing the size of particles, which is consistent with the results of the current numerical model.

In Figure 8-14, the large particle size was equal to 1/3 of the dipper's lip. It can be seen that during the first half of the cycle, three particles blocked the dipper entry and did not allow further particles to flow inside the dipper. After that, by changing the orientation of the dipper, and with gravity assistance, those particles fall inside and let more material flow into the dipper. This movement of material did not happen in smaller particles. Figure 8-15 and Figure 8-16 illustrated that smaller particles had no difficulties in loading, and the dipper experienced an easier dig condition.

The empty space was generated in all three simulations, but its size was reduced by decreasing the particle size. Also, according to the results, smaller particles left less void spaces, and resulted in lower void ratio.

Figure 8-16 showed that although the empty space existed until the end of the dig cycle, the amount of payload was higher in comparison to the larger particle sizes. This was due to the decreased void ratio, smaller empty space, and less probability of dipper entry blockage. The results indicated that particle size had significant influence on loading action. This may highlight the importance of blasting efficiency in excavating applications.

8-4-2- Influence of particle shape on flow mechanism

To investigate the influence of particle shape, specifically angularity, on the flow pattern, a new set of rock-piles was generated using moderate to high angular clumps (Figure 8-3) with three mentioned particle sizes and a uniform size distribution. Other properties and the procedure were the same as the simulations in the previous section. For each particle size, the dig action was repeated through a number of runs. Figure 8-17 to Figure 8-19 illustrate a few snapshots of a dig

cycle for each particle size. Particles were colored based on their velocities. The findings showed the same influence of particle size, as mentioned in the previous section. However, the angularity of the material had a significant effect on the final rockpile shape and performance of the dipper.

As can be seen, more angular particles created steeper piles, both inside and in front of the dipper. Angular particles showed more tendencies in blocking the entry of the dipper and creating empty spaces at the rear of the dipper. Figure 8-17 showed entry blockage of the dipper initiated from the beginning stages of the dig cycle in comparison to the lower angular particles with the same size. Also, the size of the empty spaces was bigger in the simulations with more angular particles. This increased size and angularity is more noticeable in Figure 8-17 and Figure 8-18 in comparison to Figure 8-14 and Figure 8-15. More angular particles left more void spaces both in the rockpile and inside the dipper. More rotational and sliding modes of motions were seen in less angular particles. A comparison of the final payloads indicated that more angular material resulted in less amount of payload. This relation can be seen in all three examined particle sizes. As the angularity increases, particles cannot easily pass one another and become interlocked. They need to overcome a higher frictional resistance due to rolling limitations while rounded or less angular particles move past one another via sliding and rotation with little resistance.

Increased angularity leads to increased interlocking, and therefore a higher void ratio. As particles become more angular, they tend to interlock more and provide more frictional resistance at the contact interfaces, which leads to a higher friction angle, and so a steeper pile. Larger particles show a greater possibility to block the entry of the dipper and create empty spaces at the rear of the dipper.

Also, they produce more void spaces and less amount of payload. One can conclude that in conditions with more angular particles, breaking the material into smaller sizes would be more efficient due to a smaller void ratio and less chance of entry blockage, thereby allowing easier loading into the dipper.

It should be noted that the amount of penetration plays an important role in digging efficiency. In all the DEM modeling, it was assumed that the dipper's engagement into the rockpile was the same. In a more efficient dig action, the dipper should move along the rockpile slope. Therefore, the dipper's trajectory needs to be changed on different slopes. Employing the same trajectory as

used in the less angular/smaller particle size rock masses, results in more penetration in the high angular/larger materials, increasing the probability of particle blockage and higher frictional resistance.

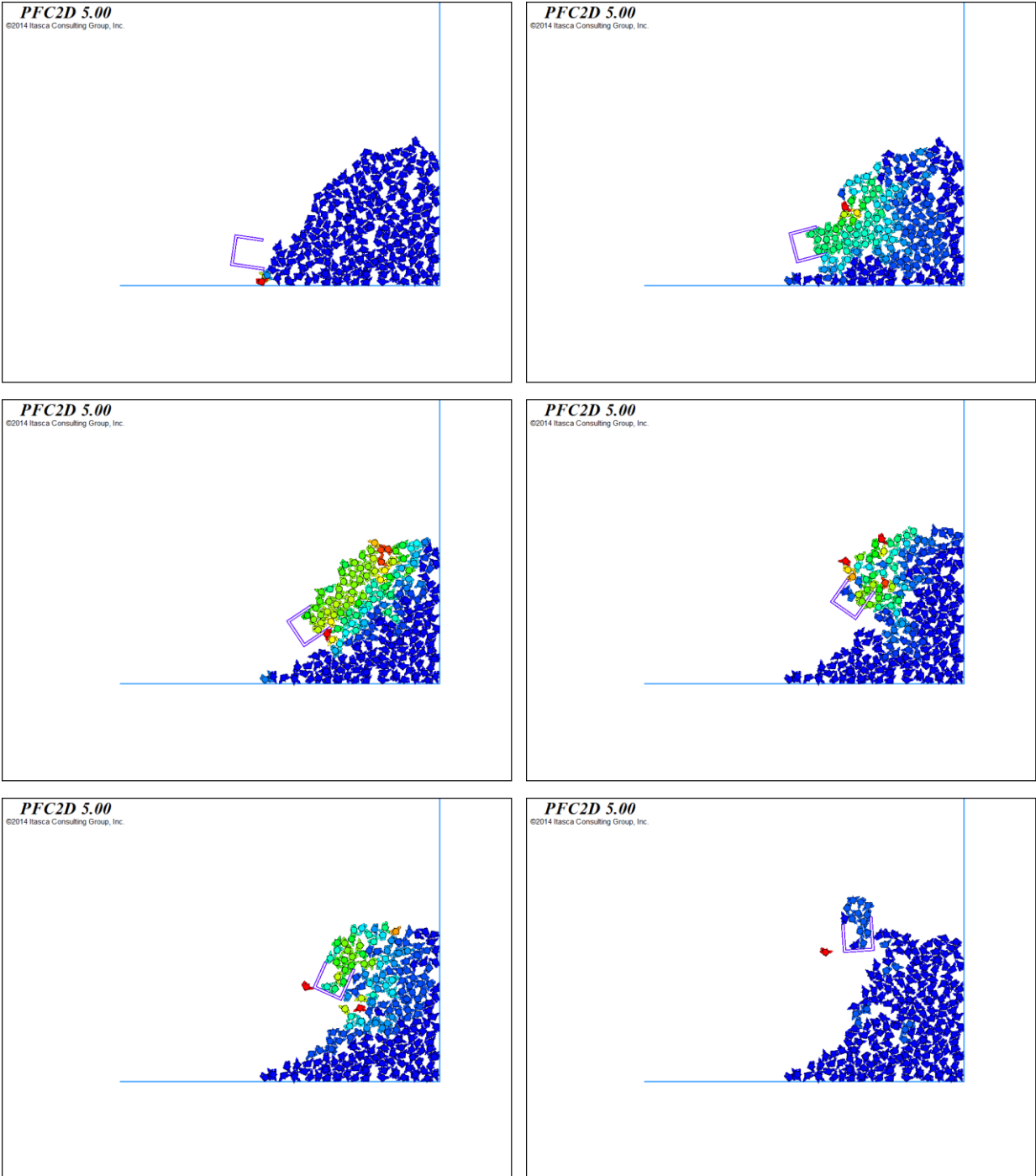


Figure 8-17 Snapshots of dig cycle with large particle sizes with more angular particles

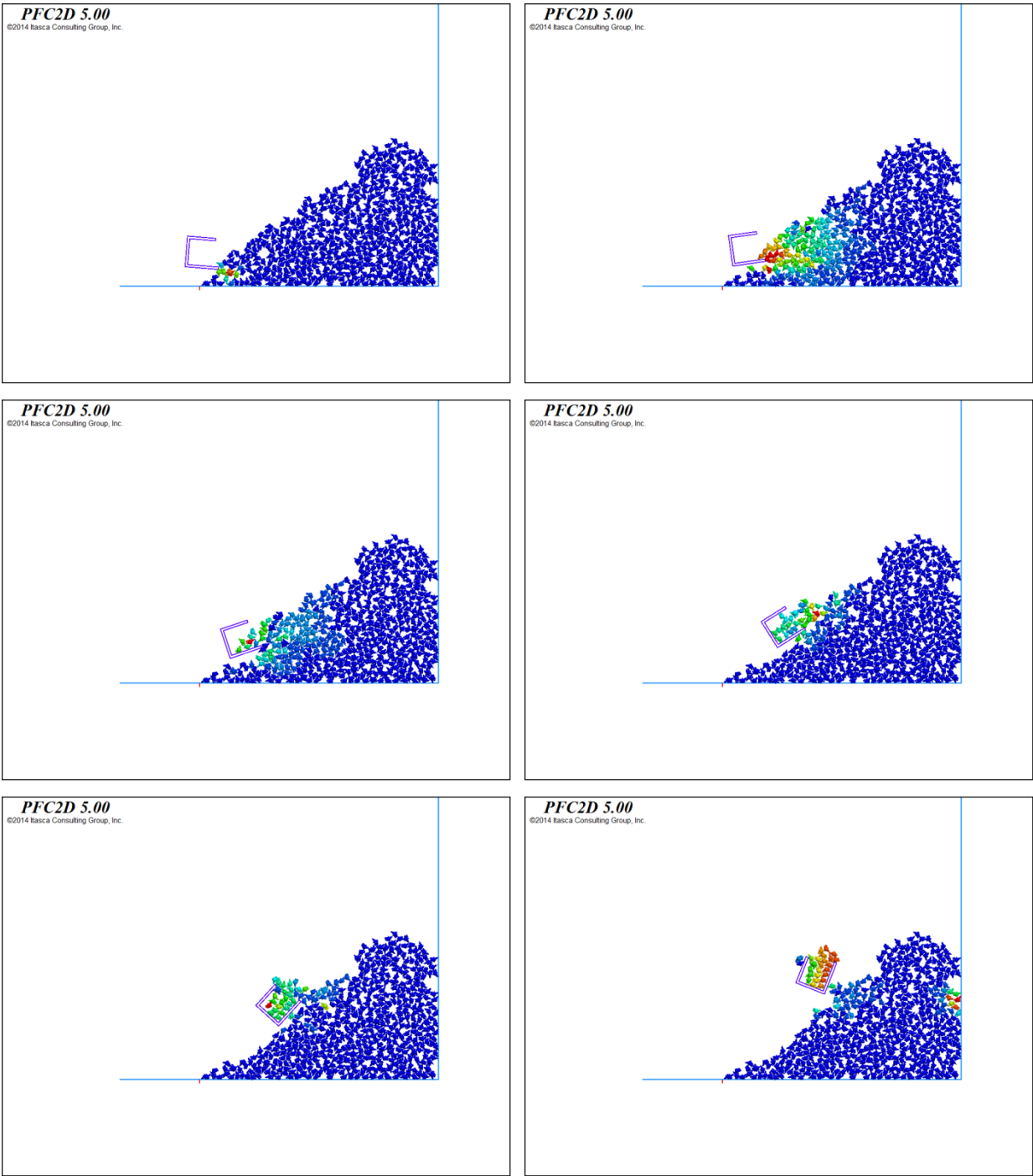


Figure 8-18 Snapshots of dig cycle with medium particle sizes with more angular particles

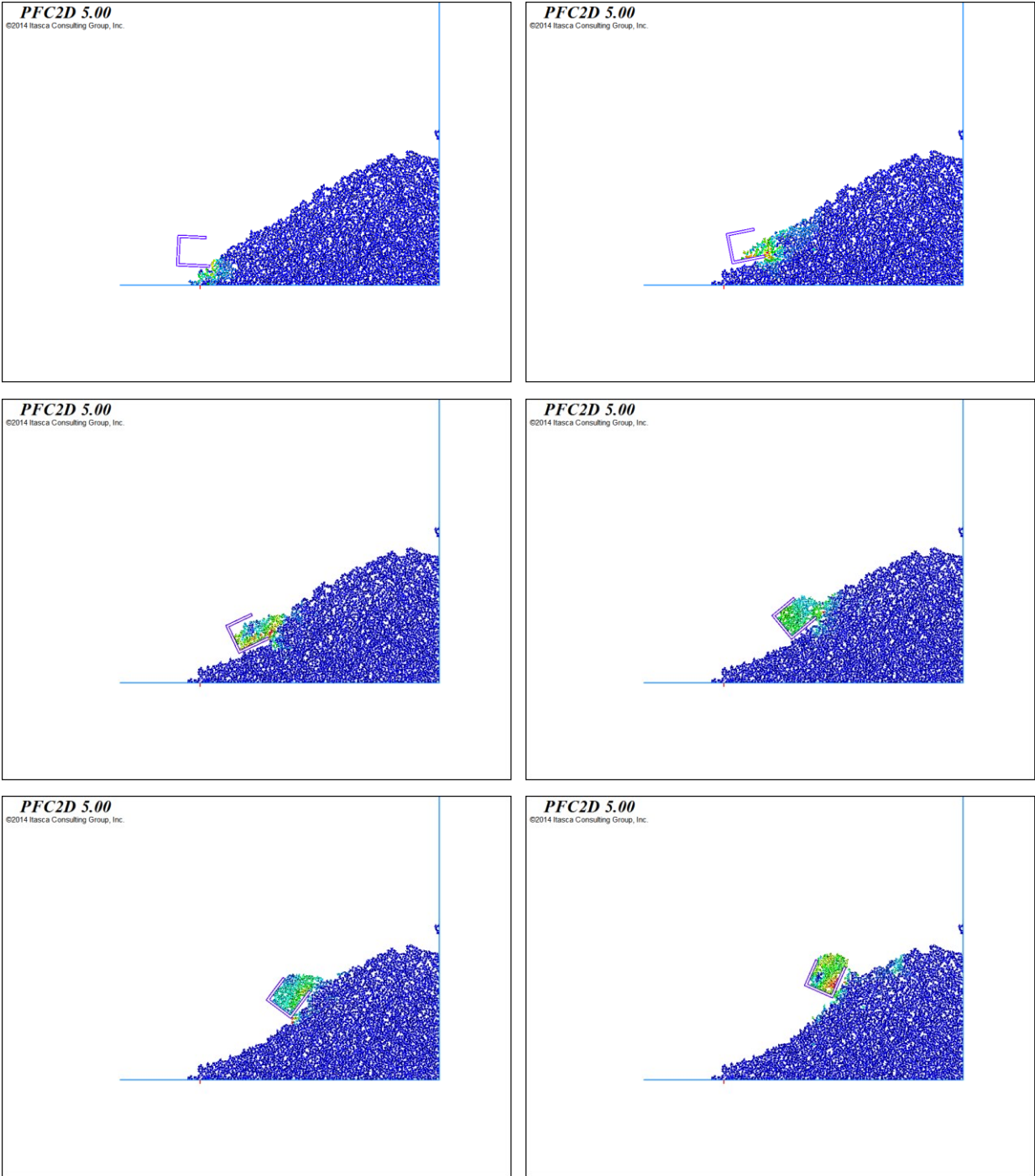


Figure 8-19 Snapshots of dig cycle with small particle sizes with more angular particles

8-4-3- Influence of dipper teeth on flow mechanism

To study the influence of the dipper tooth on the flow pattern, a new dipper was created by adding two walls to the existing simulated dipper to represent a tooth. Then the simulations with minimum size particles with lower and higher angular particles were performed with the new dipper and the results compared to the similar scenarios that used a dipper without teeth. Figure 8-20 and Figure 8-21 show a few snapshots of a recorded dig cycle with minimum simulated particles sizes with a modeled dipper with tooth. Figure 8-22 compares two simulated dig cycles. The left column is related to a dipper without tooth and the right column is related to a dipper with tooth. The original position of the dipper, rockpile properties and material properties (low to moderated angular clumps) were the same in the two models. Particles were colored based on their velocities.

As seen in Figure 8-22, from the initial step, the dipper with teeth had more penetration into the rockpile. By continuing the digging, the dipper with teeth created a thicker layer of flowing material inside, and a bigger wedge of material in front of the dipper. In the second half of the cycle, the thickness of material inside the dippers has the same height, but the size of the wedge was still bigger in the dipper with teeth. At the end of the cycle, when the dipper's rear wall reached to the horizontal, the final payload of the dipper with teeth seemed noticeably higher than the dipper without teeth.

The results suggested that employing a dipper equipped with a tooth increased the penetration depth and lifted more material into the dipper. The teeth broke apart the material more easily and provided a thicker layer of particles at the entry to the dipper, leading to more material inside the dipper, and therefore a greater payload compared to the dipper without tooth. A higher amount of material flowing into the dipper would be a result of a larger shear of failure zone and so, a decreased cutting resistance. However, leading more material into the dipper would increase the total required drag force.

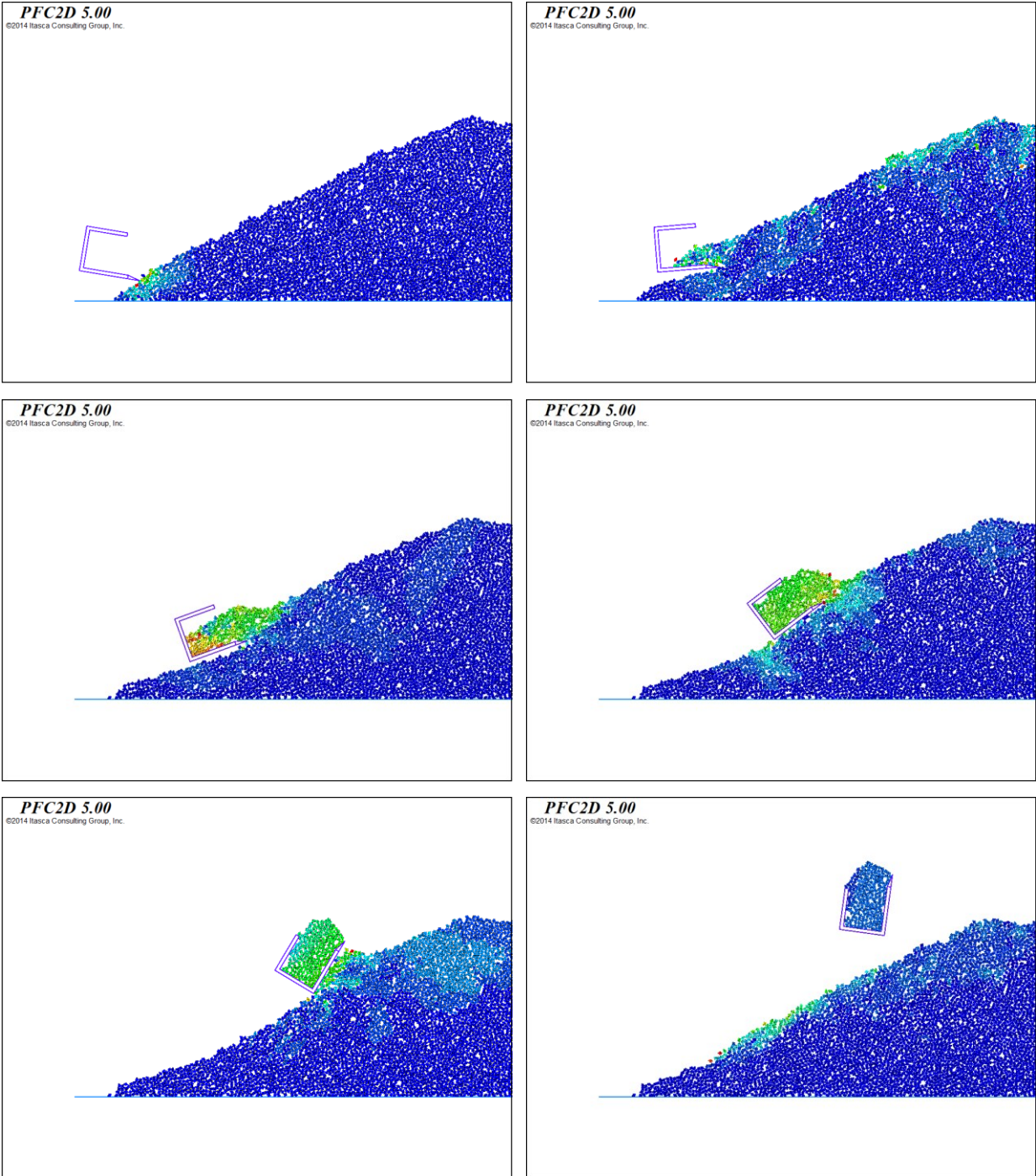


Figure 8-20 Snapshots of a dig cycle of low angular particles with a dipper with tooth

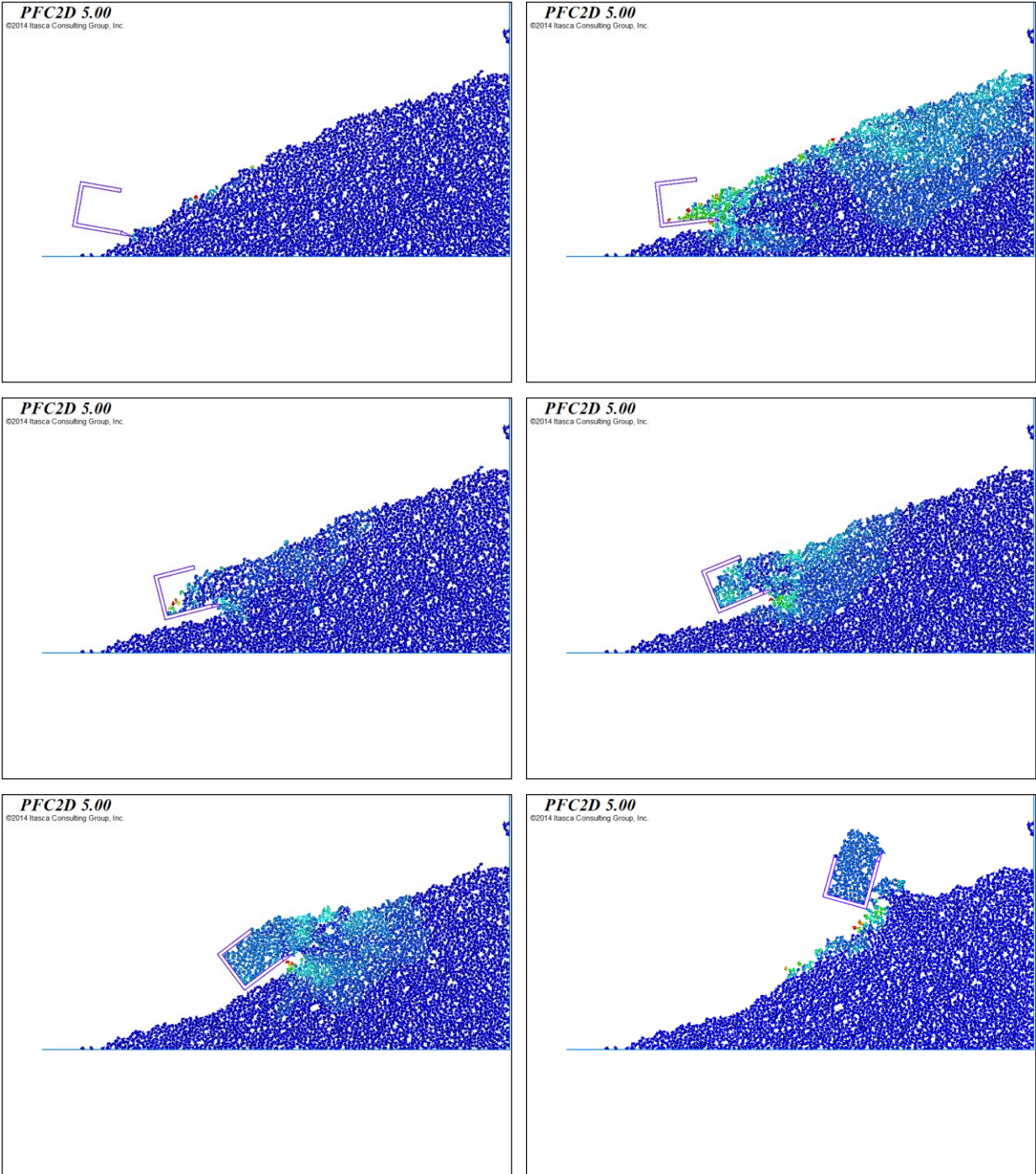


Figure 8-21 Snapshots of a dig cycle of high angular particles with a dipper with tooth

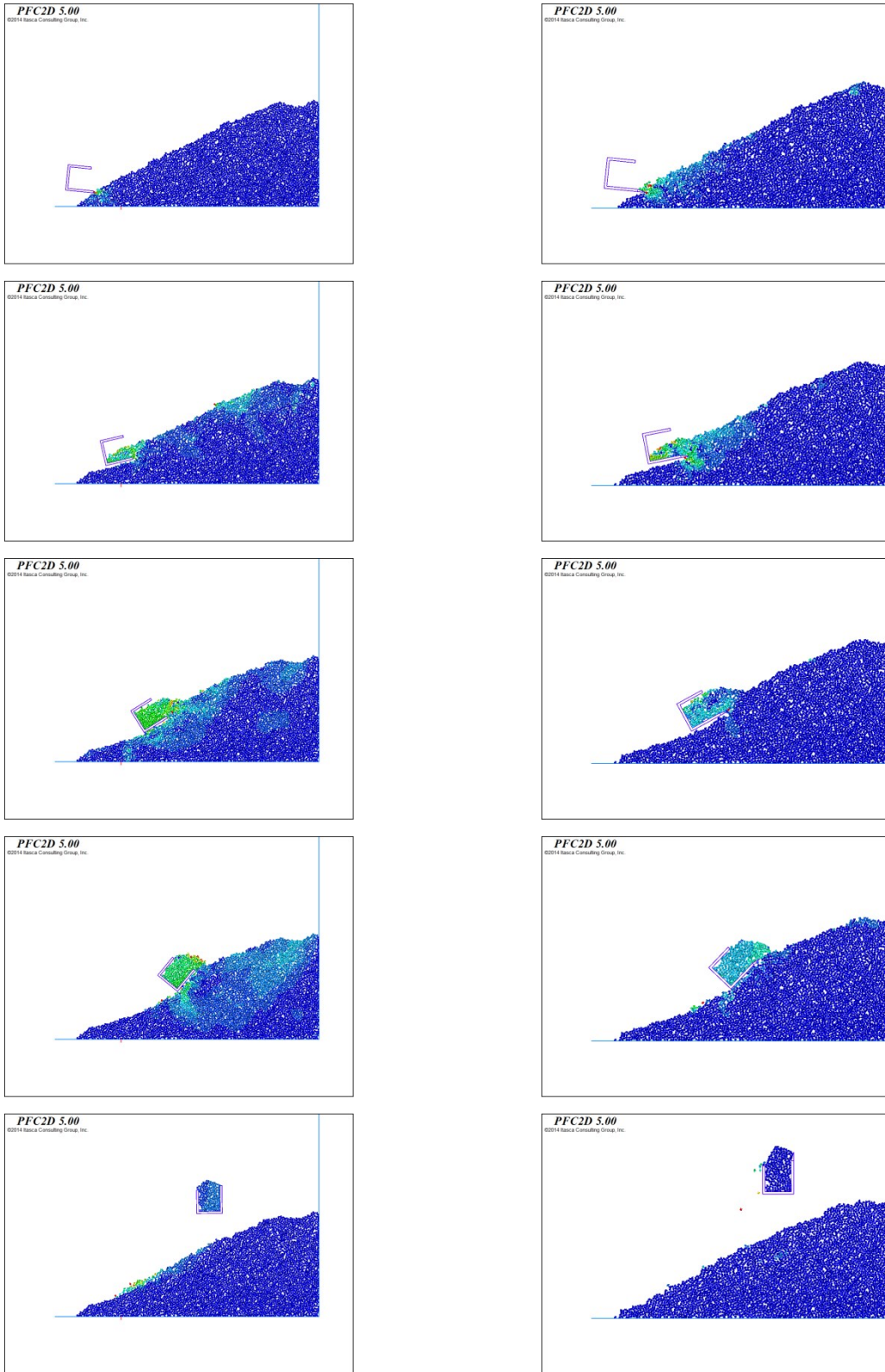


Figure 8-22 Snapshots of a dig cycle; a dipper with tooth vs without tooth

8-4-4- Numerical modeling results

The results of the numerical simulations showed that the flow pattern was independent of the dig condition, but material properties influenced the dig efficiency. Findings of these simulations can be summarized as follows:

Void ratio and material slopes: Void ratio and slope of the material inside and in front of the dipper directly varied with the angularity and size of particles. Larger and more angular particles tended to more interlocking, which resulted in a higher frictional coefficient, and therefore, steeper piles and more inter particle spaces.

Payload: The amount of payload is one of the critical parameters that show the efficiency of a machine. Increasing angularity and size of granules inversely influenced the amount of payload. More angular and larger particles left more void spaces and reduced the available volume inside the dipper, resulting in a lower amount of payload. In contrast, employing a dipper equipped with teeth increases penetration and results in a higher amount of payload under similar dig conditions.

Empty space: Creating the empty space at the rear of the dipper depended on the material properties and dig condition. Angularity, roughness, size of particles, and depth of cut were the main factors that might lead to such a space. Higher angularity and roughness limited rolling ability and increased interlocking. Larger granules caused more possibility of blockage and revealed more resistance. On shallower depth of cuts, the thinner flowing material showed less sliding resistance, and so, less possibility of creating an empty space.

Angle of repose: Angle of repose, which is a fundamental material property, depends on size, shape, angularity, roughness, degree of sorting, degree of packing, and specific gravity of the particles in a system (Van Burkalow, 1945; Fowler and Chodziesner, 1959; Miller and Byrne, 1966; Chen and Cotton, 1988; Froehlich, 2011). Increasing the angle of repose by increasing the particle size and angularity was confirmed with the findings of the current modeling.

Failure curvatures: Consistent with the results of the experimental lab tests, depending on the position of the dipper and rockpile properties such as pile slope, particle size, interlocking, etc., various number of failure curvatures were generated in front of the dipper. Present simulations showed that, independent of the shape of clumps, in rock-piles with larger particles, the size of the

impacted area was vaster. This is common with the previous findings ((Bandis et al., 1981 & 1982), that indicate increasing particle size results in reducing degree of freedom, and therefore a decreased shear strength.

8-6- Conclusion

A series of DEM simulations was performed to show a better understanding of the dynamics of filling a cable shovel dipper, and the importance of particle size and shape, as well as the dipper's teeth on the application. A PFC code was developed to determine the capability of the DEM in modeling the flow of granular material into a cable shovel dipper. To verify the accuracy of the designed numerical model, the results were compared against the experimental analysis.

Due to the limitations of the available computer technology and facilities, many assumptions had to be made to reduce the number of particles used in the simulation and to reduce the total processing time to a reasonable length. Assumptions such as designing the particles and the dipper as simple as possible, creating the rockpile in a restricted boundary, and employing calibration methods and the contact and damping models that were initially designed to solve static systems could have caused inaccuracy within the numerical model. However, the results showed the DEM simulation was able to model the granular flow.

The DEM simulation successfully modeled the flow pattern of granular material into a cable shovel dipper. It predicted many of the trends seen in the experimental set up. Different steps of the flow mechanism and the layers of flowing particles proposed in the experiments were identified in the numerical simulation. Also, the procedure of creating the empty space inside the dipper could be seen in the numerical simulations by modifying the particle sizes in the DEM model.

Two different dipper designs and different particle sizes and shapes were analysed as well. It was found that increasing the particle size results in a steeper slope rockpile, higher percentage of void ratio, larger empty space at the rear of the dipper, and lower amount of payload. More angular particles become more interlocked and increase frictional resistance. More angularity would result in a higher void ratio, steeper pile, more dipper entry blockage, and less payload. Employing a

dipper equipped with a tooth provides an easier dig condition, and so leads more material to flow into the dipper, consequently providing more amount of payload and less cutting resistance.

The main imprecision of the current simulations was that the particles hardly resisted the digging via the dipper. An insufficient internal friction coefficient and low roughness resulted in a low dig resistance. Therefore, particles easily moved one over another and loaded the dipper. Inadequate compaction, which was enhanced in 2D modeling by omitting the third dimension, was another reason to reduce the interlocking, and therefore, reduce the sliding resistance. The method of creating the rockpile, as well as inaccurate damping and contact models might be the other factors. In such an easy digging condition in which the dig resistance seemed to be significantly less than the dig force, there was less chance to create the empty space inside the dipper, which lead to a smaller void space, and so a higher amount of payload in comparison to the reality.

Chapter 9

Conclusion

9-1 - Main conclusions

Electric cable (or rope) shovels are critical equipment in the surface mining industry. Factors influencing the profitability and effectiveness of shovels include material properties (Singh et al., 1992; Taksuk et al., 2000). As mines endeavour to improve productivity and maintain competitiveness, more attention is given to rock fragmentation, which its role on the production and costs is undeniable (Hendricks et al., 1989, and Singh et al., 2006A&B).

Based on previous works, the interrelation of granular composition of blasted hard rock and shovel productivity has been studied incompletely. An improved understanding of the factors that affect the flow of broken material into the dipper during loading can help to evaluate the performance of the excavator, define the criteria for equipment selection, and develop ways to mitigate equipment damage caused by broken particles.

In order to understand the cable shovel loading procedure better, this thesis employed two approaches: scaled experimental laboratory tests, and numerical modeling (Figure 9-1).

9-1-1- modeling cable shovel filling

The mechanism of granular material flow was investigated experimentally through a series of laboratory tests by moving 1:32 and 1:20 (cube root scale) models of a 44m³ dipper through a test bin filled with angular crushed limestone. The dipper/handle assembly was hoisted at constant velocity by an electric motor. As the dipper was hoisted through the material, the resultant flow patterns were observed using a high resolution camera, and the hoist force was recorded using a load cell attached to the hoist rope and an e-Daq data acquisition system. At the end of each run, the cycle time and the dipper payload were measured. Tests were run for 3 different hoist speeds and 3 different dipper pitch angles with the main dipper model (smaller to

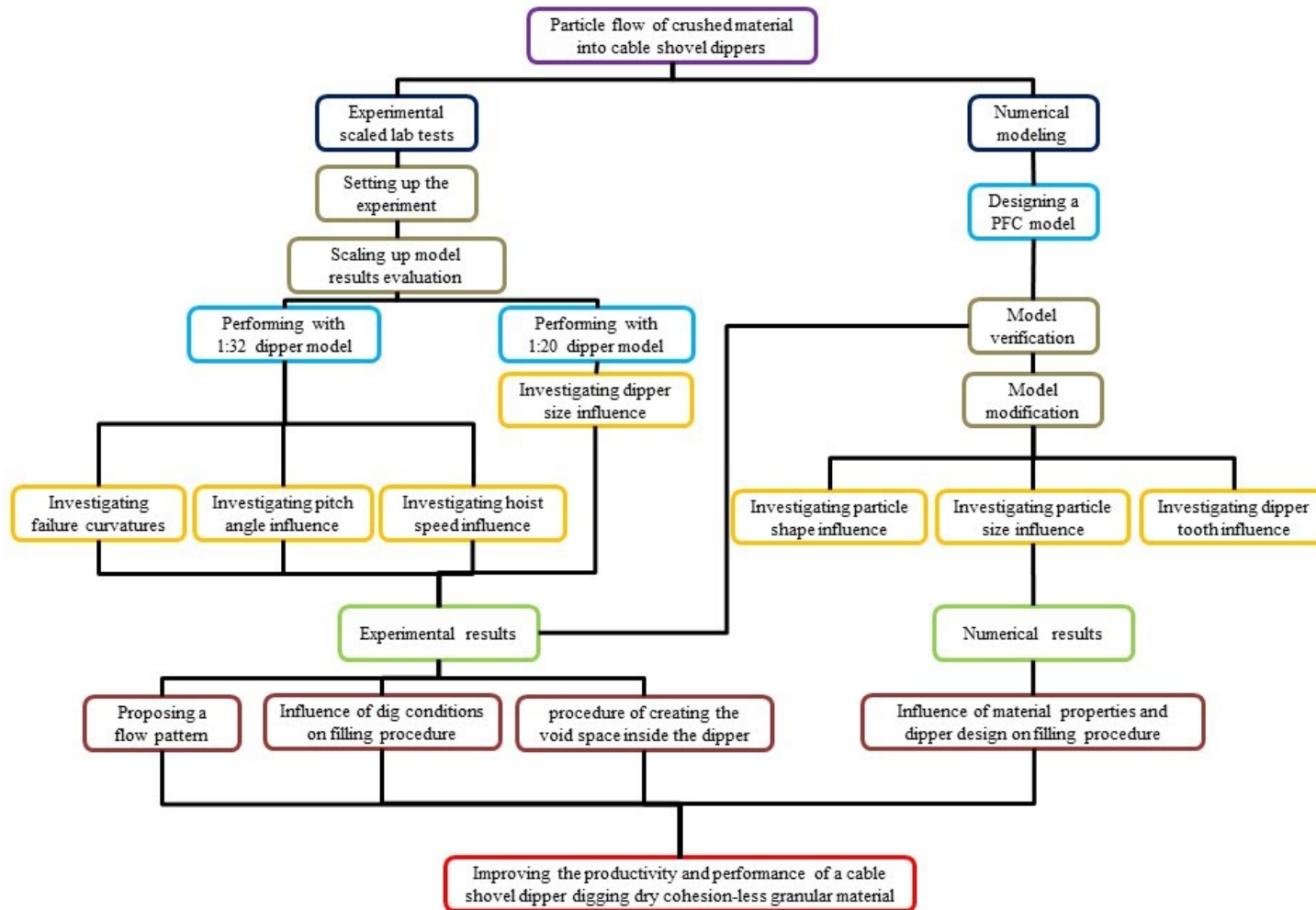


Figure 9-1 Diagram of the used approach in the research

dipper) for a total of 9 (3×3) different dig conditions. The second model (bigger dipper) was constructed investigate the influence of the dipper size on the particle flow pattern. It was tested at only one dig condition with all other parameters held constant.

Also, as a part of experimental lab tests, the development of failure envelopes in the material during a dig cycle was studied. For this purpose, the tests were run for the examined hoist speeds and dipper pitch angles with the main dipper model, while the camera recorded dig cycles from side view.

To evaluate the capability of the experimental results to be extrapolated to the full size, different scaling approaches were used. The outcome indicated that the results may be reliable when scaling up to full size cable shovel dippers with reasonable confidence.

In the numerical study, a discrete element method approach was used to model the filling procedure of a cable shovel dipper. Therefore, a PFC model was created to simulate the behaviour of crushed hard rock during a dig cycle of a cable shovel dipper. The results were then compared against experimentally measured results. Afterwards, different scenarios were examined to investigate the influence of material properties (particle size and shape) and dipper tooth on flow pattern by modifying the main designed numerical model.

From the test observations, a flow mechanism of material during a dig cycle was proposed in a number of stages from the time the dipper engages the material to the time it detaches the rockpile. Two layers of flowing material were identified with different modes of motions and named as “flow zone” and “bulk zone”. Particles in the flow zone have sliding and rotational modes of motion. With the increase of the thickness of the flowing material and particle interlocking, granules will lose their modes of motion and transfer to the bulk zone. The movement of material in this zone is more like a movement of bulk material rather than individual particles. One of the important findings of this research was that, in contrast to previous beliefs, the typically observed void space inside the dipper is generated during the dig cycle and that its initial location is between the bottom door and front wall. The location of this void space changes during the latter stages of the dig cycle as the orientation of the dipper changes resulting in the void space moving from the front wall to the dipper back wall.

The numerical results indicated that the designed DEM model could accurately predict the general trend, identified flowing layers, and different loading stages; however, the numerical model could not precisely reproduce the experimental simulation. The main imprecision was that the particles barely behaved as crushed angular granules, and therefore hardly resisted the digging via the dipper. Possible reasons for the less accurate results of the modeled particles were the assumptions made in the creation of the numerical model. Insufficient internal friction coefficient, low roughness, inadequate compaction, method of rockpile creation, and inaccurate damping and contact models are some possible causes.

Examining different dig conditions and material properties through experimental and/or numerical modeling determined that the general flow pattern is independent to dig conditions and material properties, but they may influence the efficiency and productivity of the dipper.

9-1-2- Influence of dig conditions on particle flow behaviour

Analysing the qualitative and quantitative results determined that a lower pitch angle flattens the dipper approach to the rockpile and provides more chance of the material to flow inside the dipper more continually and smoothly. Smooth particle flow results in less probability of dipper entry blockage and higher amount of payload. Employing a faster dig speed, although increasing the rate of consuming energy, at the end of specific period of time such as a work shift, provides a higher number of completed dig cycles and lower specific dig energy, which amounts to higher productivity.

Employing a larger size dipper, however, provides a higher amount of payload due to a wider dipper lip, but does not necessarily result in a good efficiency. It was found that to reach a higher payload and an appropriate efficiency, a bigger dipper needs to penetrate deeper. Otherwise it will end up with a very low fill factor. Deeper penetration results in a greater pile of material inside and in front of the dipper, but not significant change in the behaviour of the material loading into the dipper. Applying an appropriate penetration according to the dipper size plays an important role in improving the efficiency and productivity of the machine, an improvement that should be considered

by machine operators. It is predicted that there is a relationship between dipper size and optimum depth of cut that needs further investigations.

The numerical studies found that employing a dipper equipped with teeth provides an easier dig condition and so allows more material to flow into the dipper, with consequently more amount of payload and less cutting resistance.

9-1-3- Influence of material properties on particle flow behaviour

The influence of particle shape and size were analysed numerically through different scenarios by modifying the main created PFC model. To limit the number of particles in the system and shorten the processing time, uniform size distributions were used in these scenarios. Two different particle shapes and three different particle sizes were examined.

It was found that increasing particle size or angularity results in a steeper slope rockpile, higher percentage of void ratio, and therefore lower amount of payload. Oversized and angular particles have more difficulties to fit into the dipper and require extra effort, which may cause extra energy consumption and increase the risk of damages on the machine. However, particle size could be controlled through blast fragmentation, but particle shape is one of the inherent characteristics of the material that remains out of control.

9-1-4- Influence of material properties on creating the void space inside the dipper

Experimental investigations illustrated the procedure of creating the void space inside the dipper at the presence of blasted hard rock. Since the simulated particles in the main numerical model were not precise, their behaviour resembled less angular and/or smooth particles rather than crushed angular granules. Comparing the behaviour of these two materials indicated that the probability of creating the void space inside the dipper is much higher with angular rough particles. Particles with low angularity and roughness (like simulated particles) create a very low slope pile inside and in front of the dipper and flow more smoothly into the dipper. This smooth flow will reduce the chance of creating the void space at the rear of dipper and provide more payloads. It was shown that the

procedure of creating the empty space was able to be simulated by modifying the particle sizes in the DEM model.

Simulating cable shovel dig cycle with small particle size material showed the same response as low angular and roughness particles. Fine particles have more capability to fill available spaces inside the dipper, leading to less volume of empty space, and therefore more amount of loaded material. However, the impact of under sized particles should be considered. Very fine particles increase the amount of dust in the environment and have an inverse effect on the equipment efficiency.

9-1-5- Limitations

The main limitation of the current study was in applying the DEM approach to model cable shovel filling. PFC basically was designed for static situations; the linear contact and local damping models, as well as the material calibration methods all had the static approaches (Dymond, 2007). Also, due to the time and available computer technology limitations, many assumptions had to be made to design as simple a model as possible, and to reduce the number of particles and the total processing time. . For instance, more complicated particles were designed using higher number of balls to create a clump, also 3D modeling was examined using Rhino software to design particles, the dipper, and the test bin, and then importing them into PFC3D. Unfortunately, the available computer systems (computer RAM) were not able to run such models. Consequently, these shortcomings have affected the results.

9-2 - Research contributions

The main contributions of this work are listed below:

- ✓ A particle flow mechanism for broken material into a dipper of cable shovel was proposed. This flow pattern was based on visual observations via a transparent wall dipper, and was independent on the examined dig conditions and material properties. Based on this flow pattern, the first part of material loading into the dipper has rolling and sliding modes of motion (flow zone), by increasing the thickness of the flowing material, the particles interlock to each other and loose their mode of motion that results in creating another zone (bulk zone) beneath the first zone. In

this zone, the movement of material is more like movement of a bulk material rather than individual particles. The mode of motion of these two different zones is one of the reasons that more wear is occurred at the dipper tooth and lip attachments and less at the inner walls of the dipper. Also, in addition of the pile of material inside the dipper, another pile is generated in front of the dipper lip that is linked to the inner pile. These piles grow together during a dig cycle. A part of dig energy is consumed unproductively to push this wedge of material upward. Material with higher frictional coefficient creates steeper piles and increases the probability of dipper entry blockage. Employing an appropriate dipper angle could minimize the chance of such a blockage. The material examined in this study was dry cohesion-less crushed granules. In the field, environmental parameters such as humidity and temperature influence the material properties, and therefore their behaviour. Consequently, the proposed flow pattern might be changed for other types of material (wet, cohesion, very loose, or very compact).

- ✓ The procedure of generating the void space inside the dipper was identified for the first time. Employing the transparent wall dipper not only was used to study the behaviour of material flowing into the dipper, but also advanced to observe how a void space might be created inside the dipper. Based on the both experimental and numerical results, material properties have the main role in creating such a space. Material with more angular, more surface roughness, or larger sized particles have more difficulties to smoothly flow into the dipper and fill the available spaces inside the dipper. A higher internal friction coefficient of such material causes more particle interlocking and resistance against displacements, that results in more tendency to create steeper piles inside and in front of the dipper, and therefore more material would accumulate at the dipper entry, or even block it, while an unused empty space exists at the rear of the dipper. This unknown up-to-date void space may remain up to the end of the dig cycle and so results in overestimation the dipper payload.
- ✓ Investigating the influence of different dig conditions including dipper angle and dig speed on the flow pattern led to improve the dipper productivity. Based on both experimental observations and data analysis on the several shovel key performance indicators, it was found that a lower dipper angle provides an easier and smoother flowing layer of material inside the dipper, and results in a higher amount of payload. Digging faster, although increases the rate of consuming

energy, at the end of a specific period of time, completes more number of dig cycles. Employing both, a lower dipper angle and a faster dig speed, showed a lower specific dig energy that means more efficiently energy consumption. It is worth to remind that specific dig energy is the best shovel key performance indicator has been proposed up to date to evaluate the performance of cable shovels.

- ✓ Investigating the influence of dipper capacity on the flow pattern and dipper performance specified the importance of applying an appropriate depth of penetration regarding to the dipper capacity. Employing the same cut depth for one dipper may result in a high fill factor but for another dipper with different capacity may be very shallow or very deep, that means inefficient dipper performance.
- ✓ The capability of PFC in modeling the cable shovel filling was examined. The designed numerical model could predict the different dig stages and the different zones in the flowing layer of material, but due to the insufficient friction coefficient of modeled particles, the void space generation could not accurately be simulated. As mentioned, creating the void space is a function of material properties, especially the internal friction coefficient of granules. The lower internal friction coefficient of simulated particles inhibited generation of such a void space. In the next phase of the study by increasing the size of particles and using unique size distribution, the friction coefficient of particles was increased, so the same procedure of creating the void space was observed.
- ✓ The effect of particles shape and size on dipper productivity was analysed through DEM simulations. Increasing the size and angularity of particles increases the void ratio between particles and the probability of creating the void space inside the dipper. Also, it reduces the fill factor and therefore the amount of the payload. Particle size may be controlled through blast fragmentation, but particle shape is one of the inherent characteristics of the material that remains out of control.
- ✓ A better understanding of failure curvatures in the rockpile, developed during a dig cycle, was presented. During a dig cycle several failure envelopes are generated in front of the dipper. The size and shape of such envelopes are a function of the dipper position and the dipper cut depth. More penetration into the rockpile results in a larger failure of material. It is expected that if the

dipper follows a trajectory that is tangent to all these failure envelopes, such a trajectory would be the optimum trajectory for the dipper. Further investigations are recommended.

9-3 - Suggestions for Future Works

Some important suggestions to enhance the presented work and diversify its applications have been presented as follows:

- ✓ The experimental study was based on a simplified scaled dipper model without tooth. Since in reality all shovel dippers benefit from tooth, it is suggested to perform the lab tests with a prototype dipper equipped with tooth.
- ✓ Investigating the failure curvatures implies that the optimum dipper trajectory would be a tangent to the all failure curvatures developed during a dig cycle. Further studies are required to find such a trajectory.
- ✓ The results indicated that there may be a relationship between the dipper size and the optimum depth of cut that enhances the productivity. More studies are suggested.
- ✓ It is believed that the number of assumptions and simplification that had to be made affect the precision of the designed numerical model. For instance, a simple linear model was used in this research. There are other available models that may improve the results.
- ✓ To reduce the chance of creating the void space inside the dipper and minimizing its volume, modifying the dipper design seems a good solution. For instance, examining a dipper with unparallelled side walls or a dipper with curvatures at the corners is recommended.
- ✓ One of the main reasons for inaccurate numerical results was due to available computer facilities. Therefore, to reduce the total processing time, very simple clump shapes were used to simulate crushed angular particles that may not successfully represent the real material. Creating complex clump shapes by combining a greater number of balls would simulate angular granules better and result in more accurate models. Also, employing image analysis techniques as a powerful tool to model the particles shape or creating CAD files and importing them to PFC

(Figure 9-2) would be other alternatives to model particles more precisely, especially in 3D modeling.

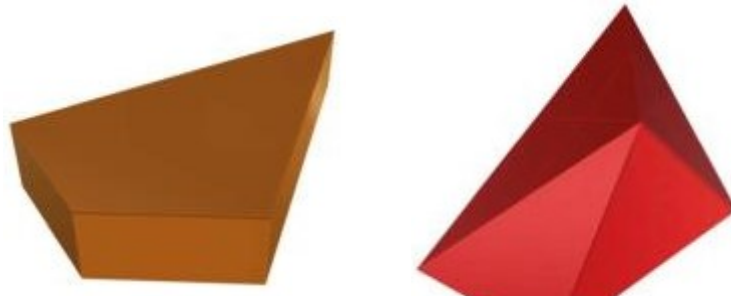


Figure 9-2 Sample of designed particles in Rhino software, imported to PFC3D

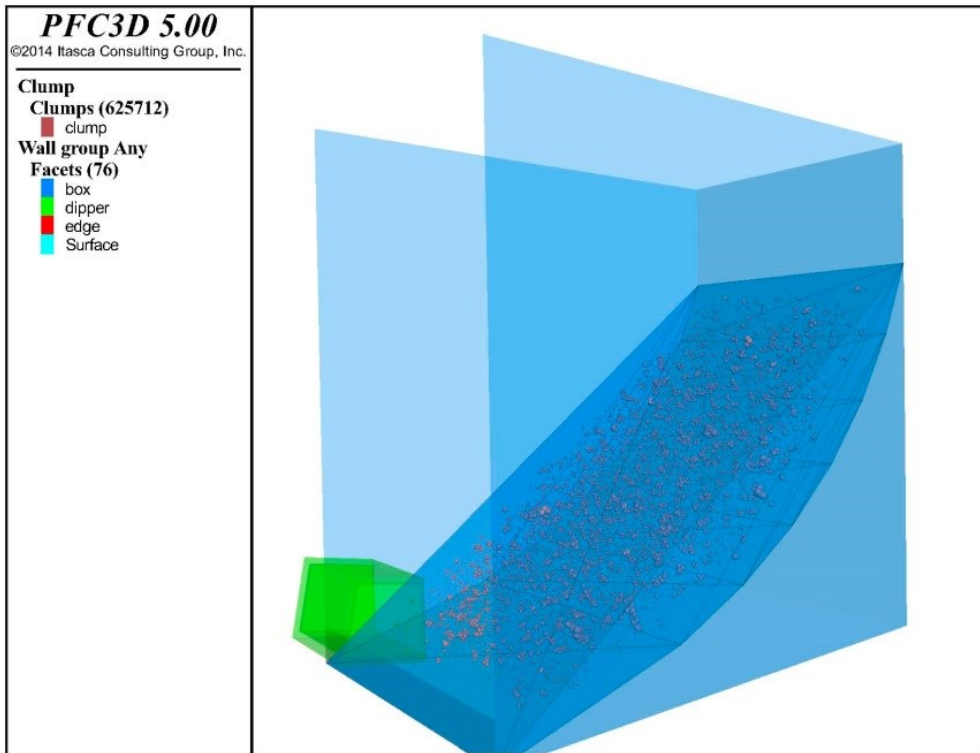


Figure 9-3 Schematic 3D mode designed in Rhino, imported to PFC

- ✓ PFC2D was used to model the cable shovel filling procedure. Omitting the third dimension influenced the material behaviour due to reducing particle interlocking that, in turn, resulted in less sliding resistance. Due to limited computer facilities, modeling with PFC3D was impossible. 3D modeling will improve the accuracy of the results and is recommended as future works (Figure 9-3).
- ✓ As mentioned, limited computer facilities (running on a single computer) was the main problem in this research. Increasing the size of simulation dramatically would increase the processing time on a single computer. PFC has this capability to be run on multiple computers or processors, including a “master processor” and a few “slave processors” (Dymond, 2007). In this case, each part of the simulation is run by employing one of the “slave processors” (Dymond, 2007). It is highly recommended to use parallel processing systems to decrease the simulation time.

References

Alderliesten, M. (2013), Mean Particle Diameters. Part VII. The Rosin-Rammler Size Distribution: Physical and Mathematical Properties and Relationships to Moment-Ratio Defined Mean Particle Diameters, *Particle & Particle Systems Characterization* Volume 30, Issue 3, pages 244–257

Anthony, J. L., Marone, Ch. (2005), Influence of particle characteristics on granular friction, *Journal of Geophysical Research*, Vol. 110, B08409, doi:10.1029/2004JB003399

Awuah-Offei, K., I Frimpong, S. (2011), Efficient Cable Shovel Excavation in Surface Mines, *Geotech Geol Eng*, 29:19–26

Awuah-Offei, K. and Frimpong, S. (2007), Cable shovel digging optimization for energy efficiency, *Mechanism and Machine Theory* 42, 995–1006

Bandis, S., Lumsden, A. C., Barton, N. R. (1981), Experimental Studies of Scale Effects on the Shear Behaviour of Rock Joints, *International Journal of Rock Mechanics and Mining Sciences & Geomechanics*, Volume 18, Issue 1, Pages 1–21

Bareither, Ch. A., Edil, T. B., Benson, C. H., Mickelson, D. M. (2008), Geological and Physical Factors Affecting the Friction Angle of Compacted Sands, *Journal of Geotechnical and Geoenvironmental Engineering* © ASCE

Barrett, P. J. (1980), The shape of rock particles, a critical review, *Journal of Sedimentology*, 291-303

Barton, N. (1976), *Rock Mechanics Review; The Shear Strength of Rock and Rock Joints*, Int. J. Rock Mech. Min. Sci. & Geomech. Abstr. Vol 13, pp. 255-279. Pergamon Press 1976. Printed in Great Britain

Barton, N., Bandis, S. (1982), Effects of block size on the Shear behaviour of jointed rock, Geomechanics Division, Terra Tek, Inc. Salt Lake City, Utah

Barton, N.R. (2008), *Shear Strength of Rockfill, Interfaces and Rock Joints, and their Points of Contact in Rock Dump Design*, Australian Centre for Geomechanics, Perth, ISBN 978-0-9804185-3-8

Blouin, S., Hemami, A., Lipsett, M. (2001), Review of Resistive Force Models for Earthmoving Processes, *Journal of Aerospace Engineering*, pp. 102-111.

Bozic, B. (1998), Control of Fragmentation by Blasting, *Journal of Rudarsko-Geološko-Naftni Zbornik*, Vol. 10

Bozzolo, D., Pamini, R. (1986), Simulation of Rock Falls Down a Valley Side, *Acta Mechanica* 63, pp. 113—130, Lugano, Switzerland

Chang, Ch. S. (1992), Discrete element method for slope stability analysis, *Journal of geotechnical engineering*, Pages: 1889-1905.

Chen, Y. H., and Cotton, G. K. (1988), Design of roadside channels with flexible linings, Publication No. FHWA-IP-87-7, Hydraulic Engineering Circular No. 15, U.S. Dept. of Transportation, Federal Highway Administration, McLean, VA.

Chiwaye, H. (2010), A comparison of the limit equilibrium and numerical modelling approaches to risk analysis for open pit mine slopes, University of the Witwatersrand, Johannesburg

Cho, G., Dodds, J., Santamarina, J.C. (2006), Particle Shape Effects on Packing Density, Stiffness, and Strength: Natural and Crushed Sands, *Journal of Geotechnical and Geo-Environmental Engineering* © Asce.

Cleary, P. W. (1998-B), the filling of dragline buckets, *math. Eng. Ind.*, vol. 7, pp. 1-24

Cleary, P. W. (2000), DEM simulation of industrial particle flows: case studies of dragline excavators, mixing in tumblers and centrifugal mills, *Powder Technology* 109, pp. 83–104

Cleary, P. W. (2009), Industrial particle flow modelling using discrete element method, *International Journal for Computer-Aided Engineering and Software*, Vol. 26 No. 6, pp. 698-743

Cleary, P.W. (1998-A), discrete element modelling of industrial granular flow applications, *TASK, Quarterly – Scientific Bulletin*, Vol. 2, pp. 385-416

Cleary, P.W. (2004), Large scale industrial DEM modelling, *Engineering Competition*, Vol. 21, pp. 169-204.

Coetzee C.J. (2004), The modelling of granular flow using the particle-in-cell method, PhD thesis, Mechanical Engineering, University of Stellenbosch, Stellenbosch, South Africa

Coetzee, C.J., Basson, A.H., Vermeer, P.A. (2007), Discrete and continuum modelling of excavator bucket filling, *Journal of Terramechanics* 44, pp. 177–186

Coetzee, C.J., Els, D.N.J. (2009-A), Calibration of discrete element parameters and the modeling of silo discharge and bucket filling, *Journal of computer and electronics in agriculture*, pp. 198-212

Coetzee, C.J., Els, D.N.J. (2009-B), The numerical modelling of excavator bucket filling using DEM, *Journal of Terramechanics* 46, pp. 217–227

Coetzee, C.J., Els, D.N.J., Dymond, G.F. (2010), Discrete element parameter calibration and the modelling of dragline bucket filling, *Journal of Terramechanics* 47, pp. 33–44

Cundall, P.A. & Strack, O.D.L. (1979), A discrete numerical model for granular assemblies, *Geotechnique* 29, No. 1, 47-65

Doktan, M. (2001), Impact of blast fragmentation on truck shovel fleet performance, 17th international mining congress and exhibition of turkey, IMCET2001, ISBN 975-395-417-4

Dorren, L.K.A. (2003), A Review of Rockfall Mechanics and Modelling Approaches, *Progress in Physical Geography* 27,1, pp. 69–87

Dymond, G. (2007), Creation, optimization and verification of a three dimensional numerical model to simulate a dragline bucket during the digging cycle using modern DEM software, Department of Mechanical and Mechatronic Engineering, University of Stellenbosch, South Africa

Fakhimi, A., Hosseinpour, H. (2008), The role of oversize particles on the shear strength and deformational behaviour of rock pile material, American Rock Mechanics Association, the 42nd US Rock Mechanics Symposium and 2nd U.S.-Canada Rock Mechanics Symposium, San Francisco

Fowler, R.T. and Chodziesner, W.B. (1959), The influence of variables upon the angle of friction of granular materials, Chemical Engineering Science, Volume 10, Issue 3, Pages 157–162

Frankline, J. A., Maerz, N. H., Santamaria, J. C. (1995), developments in blast fragmentation measurements, proceeding of 11th symposium on explosive and blasting research, Nashville, Tennessee, USA

Frimpong, S. and Hu, Y. (2004), Parametric Simulation of Shovel-Oil Sands; Interactions during Excavation, International Journal of Surface Mining, Reclamation and Environment, 18:3, 205-219

Frimpong, S. and Li, Y. (2007), Stress loading of the cable shovel boom under in-situ digging conditions, Engineering Failure Analysis 14, 702–715

Froehlich, D.C. (2011), Mass Angle of Repose of Open-Graded Rock Riprap, journal of irrigation and drainage engineering © ASCE

Guo, P., Su, X. (2007), Shear strength, inter-particle locking, and dilatancy of granular materials, Canadian Geotechnical Journal, Vol. 44 Issue 5, p579

Hadjigeorgiou, J. (1993), Studies of machine - ground interaction in surface mines, PhD thesis, McGill University, Canada

Heitiaratchi, D. R. P., Witney, B. D., Reece, A. R. (1966), The Calculation of Passive Pressure in Two-Dimensional Soil Failure, *J. agric. Engng Res.* 11 (2) 89-107

Hemami, A., Goulet, S., Aubertin, M. (1994), Resistance of Particulate Media to Excavation: Application to Bucket Loading, *International Journal of Surface Mining, Reclamation and Environment*, pp.125-119

Hemami, A., Hassani, F. (2007), Simulation of the Resistance Forces of Bulk Media to Bucket in A Loading Process, 24th International Symposium on Automation and Robotics in Construction (ISARC 2007) Construction Automation Group, I.I.T. Madras

Hendricks, C. (1990), Performance monitoring of electric mining shovels, PhD thesis, McGill University

Hendricks, C., Davison, J., Scoble, M. (1988), Electric Mining Shovel Diggability Studies, International Symposium On Mine Planning and Equipment Selection, Calgary, Canada, pp 327-333.

Hendricks, C., Peck, J., Scoble, M. (1989), Performance monitoring of electric mining shovel, Transactions; Institution of Mining and Metallurgy, Section A. Mining industry, vol. 98 pages A151-A159

Hendricks, C., Peck, J., Scoble, M. (1990), Integrated drill and shovel performance monitoring towards blast optimization, Third International Symposium on Rock Fragmentation by Blasting, pages 9-20, Brisbane, Queensland

Hu, W., Frossard, E., Hicher, P., Dano, Ch. (2010), Method to Evaluate the Shear Strength of Granular Material with Large Particles, Soil Behaviour and Geo-Micromechanics, GeoShanghai 2010 International Conference

Hustrulid, W.A., McCarter, K.M., Van Zyl, D.J.A. (2000), Slope Stability in Surface Mining, SME, Technology & Engineering, 442 pages

Itasca Consulting Group Inc. (2014-A), PFC manual

Itasca Consulting Group Inc. (2014-B), PFC course

Janoo, V. (1998), Quantification of shape, angularity, and surface texture of base course materials, US Army Corps of Engineers® Cold Regions Research & Engineering Laboratory

Jensen, R.P., Edil, T.B., Bosscher, P. J., Plesha, M. E., Ben Kahla N. (2001), Effect of Particle Shape on Interface Behaviour of DEM-Simulated Granular Materials, The International Journal of Geomechanics, Volume 1, Number 1, 1–19

Joseoh, T.G., Shi, N. (2012), A revised dipper-ground equilibrium derivation for shovels operating in oil sand and soft ground, CIM journal, vol. 3, NO. 1, 47-53

Joseph, T.G. and Shi, N. (2010), Scaling to Full Size Dipper Design Via Geometric and Performance Field Data, Proceedings of the World Congress on Engineering, Vol II, WCE 2010, London, U.K.

Joy Global (2012), P&H 4100C BOSS Electric Mining Shovel - DC Drive Product Overview

Karpuz, C., Ceylanoğlu, A., Paşamehmetoğlu, A.G. (1992), An investigation on the influence of depth of cut and blasting on shovel digging performance, International Journal of Surface Mining, Reclamation and Environment, 0.254, 161-167

Karpuz, C., Hindistan, M.A. and Bozdog, T. (2001), A new method for determining the depth of cut using power shovel monitoring. J. Min. Sci., 37, 85 – 94.

Krahn, J. (2003), The 2001 R.M. Hardy Lecture: The limits of limit equilibrium analyses, the NRC Research Press Web site at <http://cgj.nrc.ca> on

Lipsett, M.G. and Yousefi Moghaddam, R. (2011), Modeling Excavator-Soil Interaction, R. Wan et al. (Eds.): Bifurcations, Instabilities and Degradations in Geomaterials, SSGG, pp. 347–366. springerlink.com © Springer-Verlag Berlin Heidelberg

- Macias-Garcia, A., Cuerda-Correa, E. M., Diaz-Diez, M.A. (2004), Application of the Rosin–Rammner and Gates–Gaudin–Schuhmann models to the particle size distribution analysis of agglomerated cork, *Materials Characterization* 52, P. 159– 164
- Maciejewski, J., Jarzcebowski, A. (2002), Laboratory optimization of the soil digging process, *Journal of Terramechanics* 39, pp. 161–179
- Maciejewski, J., Jarzebowski, A., Trampczynski, W. (2004), Study on the efficiency of the digging process using the model of excavator bucket, *Journal of Terramechanics* 40, pp. 221-233
- Maerz, N. H. (1998), Aggregate sizing and shape determination using digital image processing. Center For Aggregates Research (ICAR) 6th Annual Symposium Proceedings, St. Louis, Missouri, pp. 195-203
- Maerz, N. H., Palangio, T. C., Franklin, J. A. (1996), WipFrag image based granulometry system. Proceedings of the FRAGBLAST 5 Workshop on Measurement of Blast Fragmentation, Montreal, Quebec, Canada, 23-24, pp. 91-99.
- Mair, K., Frye, K. M., Marone, Ch. (2002), Influence of grain characteristics on the friction of granular shear zones, *JOURNAL OF GEOPHYSICAL RESEARCH*, VOL. 107, NO. B10, 2219, doi: 10.1029/2001JB000516
- Majidi, B. (2012), Discrete element method applied to the vibration process of coke particles, MSc. thesis, Université Laval, Canada
- McLemore, V.T., et al. (2009), Questa Rock Pile Weathering Stability Project-Literature review of other rock piles: Characterization, weathering, and stability, New Mexico Bureau of Geology and Mineral Resources
- Miller, R. L., and Byrne, R. J. (1966), The angle of repose for a single grain on a fixed rough bed, *Sedimentology*, 6(4), 303–314.

Mirghasemi, A. A., Rothenburg, L., Matyas, E. L. (2002), Influence of particle shape on engineering properties of assemblies of two-dimensional polygon-shaped particles, *Geotechnique* 52, NO. 3, 209-217

Morgan J. K. (2000), *Distinct Element Simulations of Granular Shear Zones: Micromechanics of Localization and Frictional Behaviour*.

Morgan, J. k. (1999-A), Numerical simulations of granular shear zones using the distinct element method 2. Effects of particle size distribution and inter-particle friction on mechanical behaviour, *Journal of geophysical research*, vol. 104, NO. B2, Pages 2721-2732

Morgan, J. k. and Boettcher, M. S. (1999-B), Numerical simulations of granular shear zones using the distinct element method 1. Shear zone kinematics and the micromechanics of localization, *Journal of geophysical research*, vol. 104, NO. B2, Pages 2703-2719

Morrell, S., Valery, W., O'Loughlin, P. (1998), Exploring the effect of blast design on SAG mill throughput at KCGM, Mine to Mill Conference, Brisbane, Qld

Müller, B., Hausmann, J., Niedzwiedz, H. (2010), Control of rock fragmentation and muck pile geometry during production blasts (environmentally friendly blasting technique), *Rock Fragmentation by Blasting – Sanchidrián (ed)*, Taylor & Francis Group, London, ISBN 978-0-415-48296-7

Nataliya, M., Goren, L., Sparks, D., Aharonov E. (2010), What controls the effective friction of shearing granular media, Taylor and Francis Group, LLC

Onederra, I., Esen, S., Jankovic, A. (2004), Estimation of fines generated by blasting – applications for the mining and quarrying industries, *Mining Technology (Trans. Inst. Min. Metall. A)*, Vol. 113 A237

Osanloo, M., Hekmat, A. (2005), Prediction of shovel productivity in the Gol-E-Gohar iron mine. *J. Min. Sci.*, 41, 177 –184.

Owen DRJ, Feng YT, de Souza Neto EA, Cottrell M, Wang F, Andrade Pires FM, et al., 2004. The modelling of multi-fracturing solids and particulate media, International Journal for Numerical Methods in Engineering

P& H MinePro services, 2001, Peak performance practices-dippers, Harnischfeger.

Palangio, T.C. (1995), WIPFRAG- a new tool for blast evaluation, proceeding of the 11th symposium on explosive and blasting research

Parker, B.M. (2009), Simulation and Analysis of Particle Flow Through an Aggregate Stockpile, MSc thesis, faculty of the Virginia Polytechnic Institute and State University

Patnayak, S. (2006), Key performance indicators for electric mining shovels and oil sands diggability, PhD thesis, University of Alberta

Patnayak, S., Tannant, D. D., Parsons, I., Del Valle, V. and Wong, J. (2008), Operator and dipper tooth influence on electric shovel performance during oil sands mining, International Journal of Mining, Reclamation and Environment Vol. 22, No. 2

Patnayak, S., Tannant, D. D. (2005), Performance monitoring of electric cable shovels, International Journal of Surface Mining, Reclamation and Environment, Vol. 19, No. 9, 276 – 294.

Patnayak, S., Tannant, D.D., Parsons, I. and Del Valle, V. (2005), Performance Monitoring of Electric Shovels Digging Oil Sands, Proc. Int. Symp. on Mine Planning and Equipment Selection, Banff, 1021-1033

Peck, J., Hendricks, C., Scoble, M. (1990), Blast optimization through performance monitoring of drills and shovels, Second International Symposium on mine planning and equipment selection, pages 159-166, Calgary, Canada

Peck, J., Scoble, M. (1990), Integrated Drill and Shovel Performance Monitoring Towards Blast Optimization, Third International Symposium on Rock Fragmentation by Blasting, Brisbane, Queensland

Petje, U., Mikos, M., Majes, B. (2006), Motion of Rock Masses on Slopes, GEOLOGIJA 49/2, pp. 393–408, Ljubljana

Pourkhosravani, A. and Kalantari, B. (2011), A review of current methods for slope stability evaluation, Electronic Journal of Geotechnical Engineering (EJGE), Vol. 16, Bund. L

Raza M. A., Frimpong, S. (2013), Cable Shovel Stress & Fatigue Failure Modeling - Causes and Solution Strategies Review, Journal of Powder Metallurgy & Mining, S1

Reece, A.R. (1965), The fundamental equation of earthmoving mechanics, Symposium of earthmoving machinery, Institute of Mechanical Engineers, Vol. 179, pp. 16-22.

Rowlands, J.C., Just, G. D. (1992), Performance characteristics of dragline buckets Source: Third Large Open Pit Mining Conference, pp. 89-92

Rowlands, J.C. (1991), Dragline bucket filling. Ph.D Thesis, University of Queensland, Queensland, Australia

Santamarina, J.C. and Cho, G.C. (2004), Soil Behaviour: The Role of Particle Shape, Proc. Skempton Conf., March, London.

Shi, N. (2007), A new approach to improving cable shovel dipper design for cutting soft rock and soils, PhD thesis, Department of Civil and Environmental Engineering, University of Alberta, Canada.

Shi, N., Joseph, T.G. (2006), A new Canadian shovel dipper design for improved performance, Maintenance/Engineering

Siddiqui, F.I., Ali Shah, S.M., Behan, M. Y. (2009), Measurement of Size Distribution of Blasted Rock Using Digital Image Processing, JKAU: Eng. Sci., Vol. 20 No. 2, pp: 81-93 (A.D. / 1430 A.H.)

Singh, A., Scoble, M., Lizotte, Y. (1990), blast fragmentation size analysis techniques and application experience, proceeding of the 16th conference on explosives and blasting technique, Orlando, Florida

Singh, S. P., Narendrula, R. (2006-A), Factors affecting the productivity of loaders in surface mines, International Journal of Mining, Reclamation and Environment, Vol. 20, No. 1, 20 – 32

Singh, S.P., Glogger, M., Willock, D. (1992), Effect of fragmentation on loader efficiency, 27th conference on explosives and blasting techniques, At Nashville, USA

Singh, S.P., Narendrula, R. (2006-B), Productivity indicators for loading equipment. CIM Mag, 1(3), 7

Sinha, B.N. (2008), Advance Methods of Slope-Stability Analysis for Economical Design of Earth Embankment, the 12th international conference of international association for computer methods and advances in geomechanics(IACMAG), India

Spang, R.M, Rautenstrauch, R.W. (1987), Protection against Rockfall-Stepchild in the Design of Rock Slopes, 6th ISRM Congress, Montreal, Canada

Stavropoulou, M., Xiroudakis, G. and Exadaktylos, G. (2013), Analytical model for estimation of digging forces and specific energy of cable shovel, Coupled Systems Mechanics, Vol. 2, No. 1, pages 23-51 23

Strelec, S., Gazdek, M., Mesec, J. (2011), Blasting Design for Obtaining Desired Fragmentation, Technical Gazette 18, 1 79-86

Sukumaran, B., Ashmawy, A. K. (2001), Quantitative characterisation of the geometry of discrete particles, Geotechnique 51, No. 00, 1±9

Taksuk, M., Erarslan, K. (2000), Factors Affecting Loading Performance of Excavators in Grap Lignite Enterprise, Mine Planning and Equipment Selection

Thote, N.R. and Singh, D.P., (2003), Blast fragmentation size assessment analysis for production blasts in Indian mining conditions, *Explosives and Blasting Technique*, Holmberg (ed.), Swets & Zeitlinger, Lisse, ISBN 90 5809605 X

Tipthavonnukul, S. (2002-A), Numerical Simulation of Granular Particle Movement in Fluid Flow, PhD thesis, Department of Civil and Environmental Engineering, University of Alberta, Canada

Tipthavonnukul, S., Chan, D. (2002-B), Numerical Simulation of Granular Particles Moving in Fluid Flow, *Discrete Element Methods*, pp. 183-188

Van Burkalow, A. (1945), Angle of repose and angle of sliding friction: an experimental study, *Geol. Soc. Am. Bull.*, 56(6), 669–707.

Wadell, H. (1932), shape and roundness of rock particles, *The Journal of Geology*, Vol. 40, No. 5, pp. 443-451 Volume.

Wei, B., Gao, F. (2012), Digging trajectory optimization for a new excavating mechanism of electric mining shovel, *Proceedings of the ASME International Design Engineering Technical Conferences & Computers and Information in Engineering Conference IDETC/CIE*, USA

Williamson, S., McKenzie, C., O'Loughlin, H. (1983), Electric shovel performance as a measure of blasting efficiency, *1st International Symposium on Rock Fragmentation by Blasting*, Lulea, Sweden, vol. 2, pp. 625 –635.

Wikipedia, https://en.wikipedia.org/wiki/Slope_stability_analysis

Wu, H. (1995), *Modeling and Simulation of Electric Mining Shovels*, McGill University, Canada

Appendix A

Calculation of dig energy for cable shovels

Current and voltage from hoist and crowd motors come from the recording system in cable shovels.

Power=current × voltage

Force=(Power/speed) × machine efficiency

Energy=Force × displacement= $\int_{t_1}^{t_2} \Delta p dt$ (p: power, t: time)

In the current lab experiment, the hoist force was recorded directly using a load cell and a data acquisition system with the rate of 100 data per second. Following is an example of dig energy calculation based on the recorded data:

Time	bucket@#heavss	1 RN, 1	force (positive)	hoist length(cm)	ceowd length(cm)	d (cm)	cumulative d (cm)	E=F*d (lb*cm)	cumulative E (lb*cm)
22:00	-2.428		2.428	100.000	73.000	0.000	0.000	0.000	0.000
22:01	-2.347		2.347	99.978	73.000	0.022	0.022	0.052	0.052
22:02	-2.363		2.363	99.956	73.000	0.022	0.044	0.052	0.104
22:03	-2.396		2.396	99.934	73.000	0.022	0.066	0.053	0.156
22:04	-2.379		2.379	99.912	73.000	0.022	0.088	0.052	0.209
22:05	-2.396		2.396	99.890	73.000	0.022	0.110	0.053	0.261
22:06	-2.444		2.444	99.868	73.000	0.022	0.132	0.054	0.315
22:07	-2.444		2.444	99.846	73.000	0.022	0.154	0.054	0.369
22:08	-2.379		2.379	99.824	73.000	0.022	0.176	0.052	0.421
22:09	-2.396		2.396	99.802	73.000	0.022	0.198	0.053	0.474
22:10	-2.396		2.396	99.780	73.000	0.022	0.220	0.053	0.527
22:11	-2.444		2.444	99.758	73.000	0.022	0.242	0.054	0.580
22:12	-2.460		2.460	99.736	73.000	0.022	0.264	0.054	0.635
22:13	-2.460		2.460	99.714	73.000	0.022	0.286	0.054	0.689
22:14	-2.477		2.477	99.692	73.000	0.022	0.308	0.054	0.743
22:15	-2.412		2.412	99.670	73.000	0.022	0.330	0.053	0.796
22:16	-2.412		2.412	99.648	73.000	0.022	0.352	0.053	0.849
22:17	-2.412		2.412	99.626	73.000	0.022	0.374	0.053	0.902
22:18	-2.396		2.396	99.604	73.000	0.022	0.396	0.053	0.955
22:19	-2.412		2.412	99.582	73.000	0.022	0.418	0.053	1.008
22:20	-2.428		2.428	99.560	73.000	0.022	0.440	0.053	1.062
22:21	-2.460		2.460	99.538	73.000	0.022	0.462	0.054	1.116
22:22	-2.493		2.493	99.516	73.000	0.022	0.484	0.055	1.171
22:23	-2.509		2.509	99.494	73.000	0.022	0.506	0.055	1.225
22:24	-2.460		2.460	99.472	73.000	0.022	0.528	0.054	1.280
22:25	-2.444		2.444	99.450	73.000	0.022	0.550	0.054	1.334
22:26	-2.444		2.444	99.428	73.000	0.022	0.572	0.054	1.387
22:27	-2.428		2.428	99.406	73.000	0.022	0.594	0.053	1.441
22:28	-2.460		2.460	99.384	73.000	0.022	0.616	0.054	1.495
22:29	-2.460		2.460	99.362	73.000	0.022	0.638	0.054	1.549
22:30	-2.444		2.444	99.340	73.000	0.022	0.660	0.054	1.603
22:31	-2.428		2.428	99.318	73.000	0.022	0.682	0.053	1.656
22:32	-2.428		2.428	99.296	73.000	0.022	0.704	0.053	1.710
22:33	-2.444		2.444	99.274	73.000	0.022	0.726	0.054	1.763
22:34	-2.477		2.477	99.252	73.000	0.022	0.748	0.054	1.817
22:35	-2.477		2.477	99.230	73.000	0.022	0.770	0.054	1.872
22:36	-2.460		2.460	99.208	73.000	0.022	0.792	0.054	1.927
22:37	-2.460		2.460	99.186	73.000	0.022	0.814	0.054	1.981
22:38	-2.460		2.460	99.164	73.000	0.022	0.836	0.054	2.035
22:39	-2.460		2.460	99.142	73.000	0.022	0.858	0.054	2.089
22:40	-2.477		2.477	99.120	73.000	0.022	0.880	0.054	2.143
22:41	-2.493		2.493	99.098	73.000	0.022	0.902	0.055	2.198
22:42	-2.493		2.493	99.076	73.000	0.022	0.924	0.055	2.253
22:43	-2.477		2.477	99.054	73.000	0.022	0.946	0.054	2.308
22:44	-2.460		2.460	99.032	73.000	0.022	0.968	0.054	2.362
22:45	-2.460		2.460	99.010	73.000	0.022	0.990	0.054	2.416

Appendix B

Field data example come from recording systems in cable shovels

	A	B	C	D	E	F	G	H	I	J	K	L	M	N	O	P	Q	R	S	T	U	V	W
1																							
2																							
3																							
4																							
5																							
6																							
7																							
8																							
9																							
10																							
11																							
12																							
13																							
14																							
15																							
16																							
17																							
18																							
19																							
20																							
21																							
22																							
23																							
24																							
25																							
26																							
27																							
28																							
29																							
30																							
31																							
32																							
33																							
34																							
35																							
36																							
37																							
38																							
39																							
40																							
41																							
42																							
43																							
44																							
45																							
46																							
47																							
48																							
49																							
50																							
51																							
52																							
53																							
54																							
55																							
56																							
57																							
58																							
59																							
60																							
61																							
62																							
63																							